

ENERGY ABSORPTION CAPACITY OF GRAPHITE-EPOXY
COMPOSITE TUBES

by

Marc Robert Schultz

Thesis submitted to the Faculty of the Virginia Polytechnic Institute and State University
in partial fulfillment of the requirements for the degree of

MASTER OF SCIENCE

in

Engineering Mechanics

M. W. Hyer, Chairman

A. C. Loos

J. J. Lesko

November 20, 1998
Blacksburg, Virginia

Key Words: static, dynamic, low-cost, filament winding, towpreg, 12k, 50k

Copyright 1998, Marc Robert Schultz

ENERGY ABSORPTION CAPACITY OF GRAPHITE-EPOXY COMPOSITE TUBES

by

Marc Robert Schultz

M. W. Hyer, Chairman
Engineering Mechanics

(ABSTRACT)

The energy absorption capacity of a series of axially crushed composite tubes fabricated from high tow count graphite fiber is compared with those of similar tubes fabricated from aerospace-grade fiber to determine the viability of considering the use of such fibers in automotive applications. To that end, graphite-epoxy tubular specimens with circular and square cross-sectional geometries; stacking sequences with $\pm 45^\circ$ fibers and with both $\pm 45^\circ$ and 0° fibers; and two different fiber types were fabricated and crushed both statically and dynamically to examine the energy absorption characteristics. The fiber types, in the form of preimpregnated tow (towpreg) from Thiokol, were Akzo Fortafil 50k fiber and aerospace-grade T300 12k fiber. Using the towpreg, sixteen tubes were filament wound on aluminum mandrels. Three specimens were cut from each of these tubes for a total of forty-eight specimens. Twenty-four of these specimens were crushed statically in a load frame and twenty-four were crushed dynamically in a drop fixture. In order to characterize the tubes and specimens, a number of measurements were taken. These measurements included length, wall thickness, cross-sectional dimensions, volume, and mass. Two important energy absorption measures were examined: the specific energy absorption (SEA) and the ratio of the peak load to the average load. The geometry had a significant effect on the energy absorption but the stacking sequence did not. It was also found that the 50k material was less effective at absorbing energy than the 12k material, but the 50k still may be acceptable.

Acknowledgments

I would like to thank my advisor, Professor M. W. Hyer for his friendship and support, both technical and personal. Also, I wish to thank the other members of my committee: Professors A. C. Loos and J. J. Lesko. The financial support of the National Science Foundation Science and Technology Center for High Performance Polymeric Adhesives and Composites at Virginia Tech is gratefully acknowledged.

Many people have given of their time to help me with my work. The help of Professor Loos, Dr. P. J. Shih, Tom Ochinerro, and Jennifer McMurray with my filament winding activities is much appreciated. Dr. Anand Rau was a great help to me in my early time here. I also give my thanks to Bob Simonds and George Lough for their help and expertise during the static testing performed at Virginia Tech. The dynamic portion of the testing was done at the General Motors Corporate Research and Development Center. I wish to express my deep thanks to the Body Engineering Department, in particular Hannes Fuchs and Pat Watling, for making it possible to conduct the testing there. Bill Shaver and Archie Montgomery in the ESM department machine shop were of great assistance during this project. Beverly Williams was a help in administrative matters. Bob Sadler at North Carolina Agricultural and Technical State University helped with preliminary manufacturing ideas and methods.

I'd also like to heartily thank my family for all of the support that they have given me over the years. In particular, I'd like to my father and my brother, Eric, for their love and friendship.

Table of Contents

Chapter 1	Introduction to the problem	1
Chapter 2	Experimental design	10
	2.1 Specimen parameters	10
	2.2 Static testing	12
	2.3 Dynamic testing	13
	2.4 Specimen material analysis.....	13
	2.5 Reduction of data	16
Chapter 3	Specimen manufacture	21
	3.1 Choosing a system	21
	3.2 Manufacturing equipment.....	22
	3.3 Manufacturing technique	24
	3.4 Problems encountered.....	27
Chapter 4	Specimen description	29
	4.1 Cutting/labeling scheme	29
	4.2 Data.....	32
Chapter 5	Static energy absorption characteristics	40
	5.1 Crushing modes	40
	5.2 12k specimens.....	43
	5.3 50k specimens.....	52
	5.4 Comparison of 12k and 50k specimens	59

Chapter 6	Dynamic energy absorption characteristics	61
6.1	12k specimens	62
6.2	50k specimens	69
6.3	Comparison of 12k and 50k specimens	75
Chapter 7	Comparison of static and dynamic energy absorption characteristics	77
7.1	12k specimens	77
7.2	50k specimens	80
7.3	Comparison of 12k and 50k specimens	82
Chapter 8	Conclusions and recommendations	85
8.1	Conclusions	85
8.2	Recommendations	86
References		87
Appendix	Data traces from dynamic tests	90
Vita		115

List of Figures

Figure 1-1: Ideal crush load vs. crush length	2
Figure 1-2: Different types of crush initiators	6
Figure 2-1: Cutting schemes.	11
Figure 2-2: 30° external bevel.	11
Figure 2-3: Schematic and picture of the static test setup	12
Figure 2-4: Schematic of dynamic test setup	14
Figure 2-5: Volume measure	15
Figure 2-6: Definitions of quantities from the dynamic test.	16
Figure 3-1: CMC filament winder with square tube being wound.	23
Figure 3-2: Aluminum mandrel used for filament winding the square tubes with uncut square tube	24
Figure 3-3: End view schematic of shrink wrapping with the aluminum tees	26
Figure 3-4: Shrink wrapping over the aluminum tees	26
Figure 4-1: Cutting and labeling schemes	30
Figure 4-2: Tubes (a) before and (b) after being cut into individual specimens	31
Figure 4-3: Cross sections of specimens (a) c12.2 (b) s12.1 (c) cz50.1 (d) sz50.2	34
Figure 4-4: Diameters or side lengths of (a) the 12k uncut tubes and specimens and (b) the 50k uncut tubes and specimens	35
Figure 4-5: Wall thicknesses of (a) 12k specimens and (b) 50k specimens.	36
Figure 4-6: Linear density for (a) the 12k uncut tubes and specimens and (b) the 50k uncut tubes and specimens	37
Figure 4-7: Tube volume per unit length	38
Figure 5-1: Tearing crush mode	41

Figure 5-2: Splaying crush mode (with socking also seen)	42
Figure 5-3: Socking crush mode (with splaying also seen)	43
Figure 5-4: Crush load vs. crush length traces for the circular 12k static specimens.	44
Figure 5-5: Crush load vs. crush length traces for the square 12k static specimens	45
Figure 5-6: Average crush loads of the 12k static specimens.	46
Figure 5-7: Specific energy absorption (SEA) and crush modes for the 12k static specimens	47
Figure 5-8: Normalized (a) thickness (b) linear density (c) SEA for the 12k static specimens	49
Figure 5-9: Load ratios for the 12k static specimens	51
Figure 5-10: Crush load vs. crush length traces for the circular 50k static specimens.	53
Figure 5-11: Crush load vs. crush length traces for the square 50k static specimens	54
Figure 5-12: Average crush loads for 50k static specimens.	55
Figure 5-13: Specific energy absorption (SEA) and crush modes for the 50k static specimens	56
Figure 5-14: Crush shapes of square 50k tubes with 0° layers.	57
Figure 5-15: Load ratios for the 50k static specimens	58
Figure 6-1: Energy calculated from crush load vs. crush length traces and from potential energy.	62
Figure 6-2: Crush load vs. crush length for the circular 12k dynamic tests	63
Figure 6-3: Crush load vs. crush length for the square 12k dynamic tests.	64
Figure 6-4: Average crush loads of the 12k dynamic specimens	66
Figure 6-5: Specific energy absorption (SEA) and crush modes of the 12k dynamic specimens	67
Figure 6-6: Load ratios of the 12k dynamic specimens	68
Figure 6-7: Crush load vs. crush length traces for the circular 50k dynamic specimens	70
Figure 6-8: Crush load vs. crush length traces for the square 50k dynamic specimens	71
Figure 6-9: Average crush loads of 50k dynamic specimens.	72
Figure 6-10: Specific energy absorption (SEA) and crush modes of the 50k dynamic specimens	73
Figure 6-11: Load ratios for the 50k dynamic specimens	74

Figure 7-1: (a) Average crush load and (b) specific energy absorption for the 12k specimens.	78
Figure 7-2: Load ratios of the 12k specimens.	80
Figure 7-3: (a) Average crush loads and (b) specific energy absorption of the 50k specimens.	81
Figure 7-4: Load ratios of the 50k specimens.	83
Figure A-1: Dynamic data traces for c12.2	91
Figure A-2: Dynamic data traces for c12.3a	92
Figure A-3: Dynamic data traces for c12.3b	93
Figure A-4: Dynamic data traces for cz12.1	94
Figure A-5: Dynamic data traces for cz12.2a	95
Figure A-6: Dynamic data traces for cz12.2b	96
Figure A-7: Dynamic data traces for s12.1	97
Figure A-8: Dynamic data traces for s12.2a	98
Figure A-9: Dynamic data traces for s12.2b	99
Figure A-10: Dynamic data traces for sz12.1	100
Figure A-11: Dynamic data traces for sz12.2a	101
Figure A-12: Dynamic data traces for sz12.2b	102
Figure A-13: Dynamic data traces for c50.2	103
Figure A-14: Dynamic data traces for c50.3a	104
Figure A-15: Dynamic data traces for c50.3b	105
Figure A-16: Dynamic data traces for cz50.1	106
Figure A-17: Dynamic data traces for cz50.2a	107
Figure A-18: Dynamic data traces for cz50.2b	108
Figure A-19: Dynamic data traces for s50.1	109
Figure A-20: Dynamic data traces for s50.2a	110
Figure A-21: Dynamic data traces for s50.2b	111
Figure A-22: Dynamic data traces for sz50.1	112
Figure A-23: Dynamic data traces for sz50.2a	113
Figure A-24: Dynamic data traces for sz50.2b	114

List of Tables

Table 5-1: Position, from beveled end, of tow overlaps for the 12k static specimens	52
Table 5-2: Position, from beveled end, of tow overlaps for the 50k static specimens	58
Table 6-1: Position, from beveled end, of tow overlaps for the 12k dynamic specimens	68
Table 6-2: Position, from beveled end, of tow overlaps for the 50k dynamic specimens	75

Chapter 1 Introduction to the problem

Composite materials are often used to reduce the weight of structures. In the automotive industry weight reduction is important because fuel consumption is directly related to vehicular weight. Federal regulations requiring increased fuel efficiency are forcing the industry to examine new light weight materials for major structural components. In addition, there is an increased concern for occupant safety during roadway accidents. Though active devices such as front, side, and knee airbags, and pop-out devices may be one solution, using the passive capacity of the structure is also as attractive. Metals are currently used in car frames and integrated frame-body structures, and these and other metallic components are designed to passively absorb energy during accidents. However, automotive manufacturers are moving toward nontraditional materials [1], [2] and any new structural material under consideration should be capable of participating in the energy absorption process associated with accidents. Recent work has shown that it is possible to use composite materials as both structural and energy absorbing members, and still pass federal safety standards [3].

One of the current design theories for passenger vehicles is to have a progressively compliant front end [4] and a rigid passenger compartment. A progressively compliant front end consists of a series of “crumple zones,” each resisting deflection until a certain load level is reached, and then deforming at that constant load level until the next zone is reached. The first zone deforms at a very low load level to protect pedestrians and cyclists. The series of zones that follow are designed for increasing levels of load; the final zone is the rigid passenger compartment which should resist all deflection.

When studying energy absorption there are many important variables. These include material;

manufacturing method; microstructure; geometry of specimen, including any crush initiator used; and rate of crush. An important parameter when studying energy absorption, and one often used in the automotive industry, is the energy absorbed per unit mass of crushed material. This is often called the *specific energy absorption* (SEA). The SEA provides a measure of energy absorption efficiency of a structural component but, of course, says nothing about the efficiency of the structure in regards to other areas, such as resisting buckling, damping vibrations, or its ease of manufacture. It is one of several parameters that must be considered in automotive design.

Another important factor in the study of energy absorption for energy management capabilities is the shape of the crush load vs. crush length trace. Figure 1-1 shows an ideal crush load vs. crush length trace. As the crushing begins, the load quickly rises to a peak value, then drops off slightly

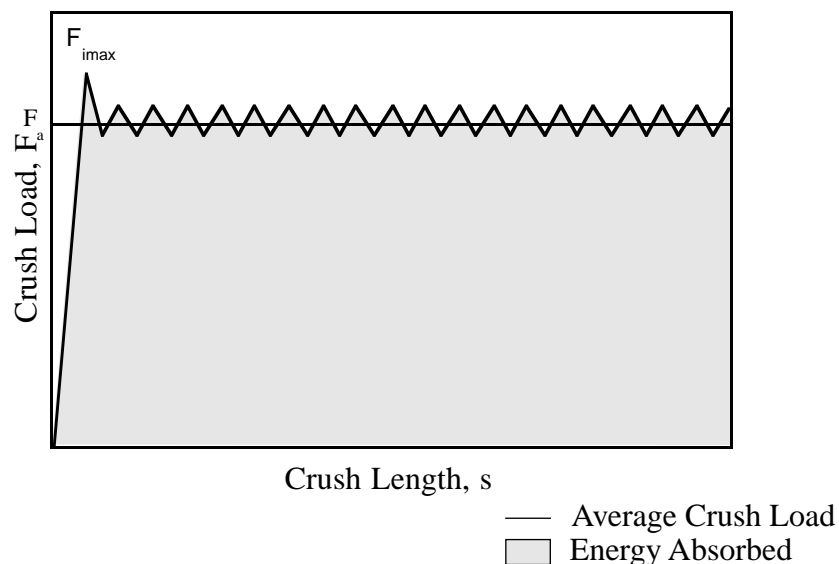


Figure 1-1: Ideal crush load vs. crush length

and stays relatively constant. In this way the energy absorption is maximized for the length of crushed material. One does not want the initial peak load (F_{imax}) to be much greater than the average crush load (F_a), because large loads would be needed to initiate crushing, and the goal in energy management is to absorb all the energy without imparting large forces to the people

involved. One measure that is used to characterize the shape of the trace is called the *load ratio*. The load ratio, which is defined as

$$\text{load ratio} = \frac{F_{i\max}}{F_a}, \quad (1-1)$$

is one metric that may be used as another important parameter for measuring crushing efficiency. Karbhari, et al. cite other sources that suggest that the load ratio should be less than 1.25 [5]. The load ratio clearly cannot be the only measure used to determine the crush efficiency. A member could have an attractive load ratio but also have very low energy absorption.

Research into the use of structural components for energy management is not new. As a result, the energy absorbing characteristics of metals are fairly well understood. Most of the research on the energy absorption of metals has concentrated on thin walled cylinders of simple cross sections. However, as early as the late 1970's, attempts at understanding the energy absorbing capabilities and crushing mechanisms of fiber-reinforced polymer composites have been made [6]. Most fiber-reinforced composites absorb energy through a combination of fracture and friction [7], whereas metals absorb energy through plastic deformation [7], [8], [9]. In order for either a metal or a composite to absorb energy efficiently, stable progressive crushing must occur. A stable progressive crush is characterized by localized failure that begins at one end of the specimen and progresses through the specimen without significant damage past this crush front. To ensure stable crushing, in both metals and fiber-reinforced composites, a crush initiator, which creates a local stress concentration, is used. If stable crushing is not established, the specimen will then usually fail catastrophically. During catastrophic failure the peak load is very high and drops off quickly, so the average load is low. Catastrophic failures are clearly not acceptable for energy management.

Farley and Jones [10] and Hull [8], [11] classified the different crush modes and micromechanisms involved in the crush modes observed in their work. Farley and Jones described four crush

modes of continuous fiber-reinforced composites: transverse shearing, brittle fracturing, lamina bending, and local buckling (although they point out that brittle fracture was really a combination of transverse shearing and lamina bending). Interlaminar crack growth and lamina bundle fracture were the mechanisms that controlled the transverse shearing mode; while interlaminar, intralaminar, and parallel-to-fiber crack growth and friction controlled the lamina bending crush mode. Brittle fracture was seen in the majority of brittle-fiber composites (i.e., graphite and glass fibers). The local buckling mode was seen in ductile-fiber composites (Kevlar[®]) and some brittle-fiber composites. The local buckling mode was similar to the crush mode of metals. In order for the local buckling mode to occur, either the fiber, the matrix, or both had to plastically yield.

Hull [8] classified the types of progressive crush failure into fiber splaying and bending, fiber splaying and axial tearing, and micro-fragmentation. The fiber splaying and bending mode was similar to the lamina bending mode of Farley and Jones. The fiber splaying and axial tearing mode was characterized by some layers bending inward and some layers bending outward, and the layers tearing into petal-like sections called fronds. With both forms of fiber splaying, a wedge of debris was present at the crush front, between the inward and outward splaying fibers. When the composite was reduced to powder and very small fragments, Hull called this micro-fragmentation.

In [11] Hull classified three modes of failure for square-ended brittle-material tubes. These three modes were Euler buckling, which was easily avoided; shell buckling and progressive folding; and brittle fracture. The brittle fracture mode was then further categorized into catastrophic failure and progressive crushing, and progressive crushing was further categorized into splaying and fragmentation. “Splaying” covered both of the types of failure described above [8]. Fragmentation was characterized by crushing and then breaking off of small pieces both inside and outside of the tube.

Carbon, glass, Kevlar, and hybrid (a composite with two or more types of fiber) fiber composites all have been studied for their energy absorption capability. Most of this work has been done with thermosetting matrix materials, usually an epoxy. Carbon fiber composites generally have a

higher SEA than composites of similar fiber placement (microstructure) made with either glass or Kevlar fiber [12], [13]. Besides epoxy, vinyl ester, polyester, and polyetheretherketone (PEEK) resins have been used as matrix material [6], [8], [14], [15]. The difficulty of producing high-quality continuous fiber tubes from thermoplastics has limited the amount of research that use thermoplastics [15].

Farley [16] and Farley, Bird, and Modlin [17] have examined the effect that fiber and matrix ultimate strain has on the energy absorption capabilities of composites. Indeed, the ultimate strain of the matrix and the fiber had a significant impact on the energy absorption properties of a material system [16]. Farley [16] suggested that to obtain the maximum energy absorption, one should combine a fiber and matrix such that the matrix has a greater ultimate strain than the fiber. Farley, Bird, and Modlin [17] found that higher ultimate strain systems with toughened matrices (Hercules AS-6/Hexcel F185 and AS-6/American Cyanamide HST-7) had lower SEA than the lower strain system [16] (Hercules AS-4/Narmco 5245).

Comparison of various fiber architectures has also been a subject of many studies [4], [5], [8], [7], [10], [11], [13], [14], [15], [16], [17], [18], [19], [20]. For composites that were made from unidirectional tape, the stacking sequence played a significant role in the energy absorbing effectiveness. Epoxy tubes with only 0° fibers tended to fail catastrophically, but when the 0° fibers were combined with 90° fibers a high SEA could be obtained. The hoop fibers constrained the tube from axial splitting and tearing, while the axial fibers provided stiffness [11]. Thornton and Edwards [20] reported that changes in stacking sequence that increased the tensile modulus also increased the SEA as long as stable crushing was obtained. It should be noted that this also increased the chance of catastrophic failure. Interestingly, Hamada, et al. [18] found a SEA of 225 J/g, perhaps the highest ever reported for any material, for carbon fiber/PEEK tubes. In an earlier paper, Hamada, et al. [15] reported that the high SEA for 0° carbon/PEEK tubes was probably due to the high fracture toughness of PEEK. It was shown for epoxy matrix tubes, even using only axial and hoop fibers, that the fiber architecture could be varied to obtain high values of SEA [11], [12], [10]. Filament wound tows, woven cloth, chopped fibers [8], pultrusion [8], [21], and braids [5] have also been studied.

The influence of specimen geometry [6], [7], [22], [23], [24], [25] (including crush initiators [6], [12], [19], [26], [27]) has also been extensively studied and has been shown to have a significant effect on the SEA. Fairfull and Hull [22], Farley [23], and Thornton [6] tested large batteries of circular tubes to determine the effects of thickness/diameter ratio. Farley [25] and Thornton [7] also tested square cross-section tubes to determine the effects of different cross sections. Farley found that for both circular and square cross-section tubes the variation with geometry changes was scalable for Kevlar/epoxy tubes but not for graphite/epoxy tubes. With near-elliptical cross section tubes, Farley and Jones [25] showed that the corners of their specimens absorbed more energy than the flatter sections, so that as the percentage of corner in the tube was increased, so was the energy absorption. It has also been shown that the use and style of crush initiator can affect the sustained crushing of a material [6], [19], [26]. The most common type of crush initiator used has been an external bevel or chamfer ground into one end of the specimen [27]. A depiction of several types of crush initiators that have been used is seen in Figure 1-2.

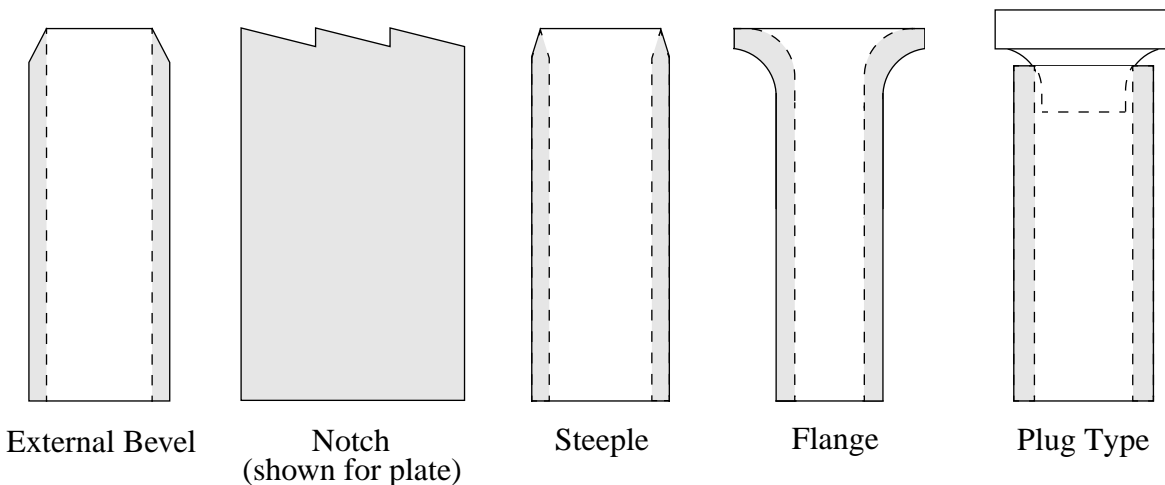


Figure 1-2: Different types of crush initiators

Because the impetus behind studying energy absorption in many investigations is energy management during crash/collision situations, the importance of rate effects has been an issue. Farley [12], [28], Schmueser and Wickliffe [13], Thornton [6], [21], and Hull [8] have all examined the effects of crushing speed on energy absorption. Farley [12] reported that the sustained crushing load for graphite/epoxy, Kevlar/epoxy, and aluminum tubes that were dropped at speeds up to 7.6

m/sec, all agreed, within 20 percent, with the static sustained crushing load. Farley [28] also tested tubes up to 13 m/s and showed that for graphite/epoxy and glass/epoxy tubes there was a slight rate dependence. Specifically, the energy absorption increased with increased rate. Schmueser and Wickliffe [13] tested graphite/epoxy, glass/epoxy, and Kevlar/epoxy tubes statically and dynamically, using a drop tower with 5.5 m/s impact speed, and found that the static testing for all tube types showed a larger SEA; specifically, up to 30% larger. Thornton [6] crushed graphite/epoxy and glass/epoxy tubes and showed a slight increase in energy absorption with increased rate over the range of 4×10^{-4} m/s to 8.5 m/s. Since these studies show opposite trends regarding the influence of impact speed, it is clear that more work in this area is needed.

Several other variables have been studied. Thornton [6] has shown that the ambient temperature during crush can significantly change the energy absorption of graphite/epoxy, glass/epoxy, and glass/polyester tubes. The surface roughness of the crush platen has been examined by several researchers. Thornton reports in a survey article [7] that several investigators have found “little difference” in the crush loads for platens made of different materials and different energy absorbing materials. Farley, et al. [29] reported that the surface roughness did play a part in the energy absorption, but only when the lamina bending mode occurs. When lamina bending occurs the SEA can increase or decrease as the roughness increases, depending on the material tested [29].

A body of research has been concerned with the modeling of the crushing process. Farley and Jones [30] have presented a simple analytical tool to determine, qualitatively, how certain variables affect the energy absorption of composite tubes. A phenomenologically-based finite-element model to calculate the energy absorbing capabilities of tubular composites was also presented by Farley and Jones [31]. Sigalas, et al. [27], Hull [11], and Faruque and Wang [32] have also published finite-element work that models the crushing of composite tubes. Good agreement has been seen between finite-element models and experimental work.

While there already exists a significant body of literature regarding the energy absorption capabilities of fiber-reinforced composite materials, new material developments and manufacturing schemes require a continuing investigation of the problem. To that end, the work reported here

focuses on the energy absorption capacity of recently available low cost, high tow count graphite fiber composites. While above studies have concluded that graphite-reinforced materials often absorb energy better than glass- or Kevlar-reinforced materials, the cost of graphite is considerably higher. However, graphite fiber that is lower in cost than traditional aerospace-grade graphite fiber is being marketed and offers some potential for cost-conscious industries such as the automotive industry. Additionally, other developments have made the manufacture of composite components somewhat simpler. In particular, for filament winding, pre-impregnated tow (towpreg) is available that can be used to wind structural components. Towpreg is a material that consists of fiber bundles, or tows, that have been pre-impregnated with a matrix material. Pre-impregnated tow offers an attractive alternative to wet winding because there is no need for the open resin bath and cleanup associated with wet winding. Of course, with the higher tow count material, the issues of stacking sequence, specimen geometry, and crushing speed are still important. The higher tow count materials are, by their nature, coarser than their aerospace-grade counterparts, therefore, they could result in different product characteristics and this must be considered. With these issues in mind, there were several specific objectives to this research effort. These objectives were to compare the energy absorption characteristics of:

- lower cost, high tow count, graphite fiber relative to more expensive aerospace-grade graphite fiber
- different stacking sequences
- different specimen geometries
- static crushing relative to dynamic crushing

Of course, the specific objectives contribute to the greater objective of determining whether or not graphite composites can be seriously considered for automotive structures.

To meet these specific objectives, epoxy-matrix towpreg material was obtained from the Thiokol Corporation [33]. Two types of towpreg were obtained; towpreg made from 12k (12,000 fibers per tow bundle) aerospace-grade Thornel T300 graphite fiber was used as the control. T300 has been an aerospace standard for many years and, as such, is quite expensive, costing \$54 per kilogram for the towpreg from Thiokol. In more recent years, as part of the industry effort to reduce the cost of carbon fiber, Akzo Nobel and other companies have begun offering less expensive, high tow-

count fiber. Akzo Nobel Fortafil 50k graphite fiber towpreg, costing \$33 per kilogram of towpreg, was selected as the other material. Each of these materials was used to fabricate tubes with two different families of stacking sequences and two different cross-sectional geometries. The two families of stacking sequences were tubes with $\pm 45^\circ$ tows and those with both $\pm 45^\circ$ and axial (0°) tows. Circular and square cross-sectional geometries were examined. With two fiber types, two stacking sequences, and two cross-sectional geometries, there were a total of eight tube types. Additionally, static and dynamic crushing tests were conducted for each tube type.

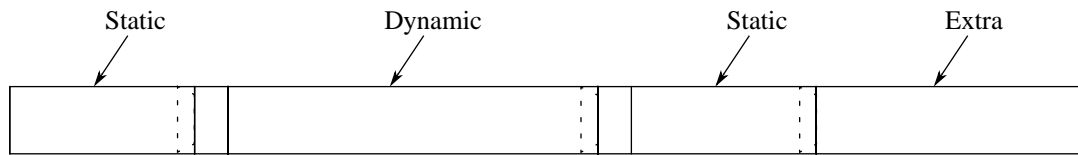
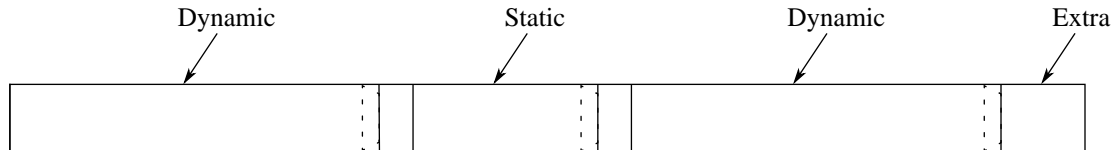
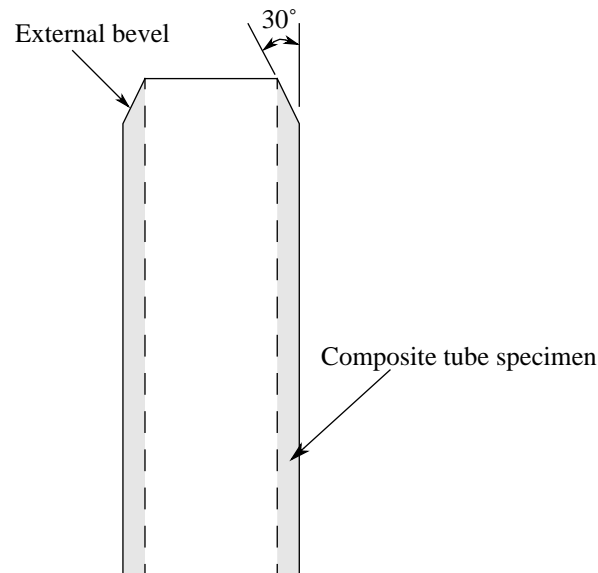
Chapter 2 will outline the experimental design and approach to meeting the objectives. The manufacturing of the tubes will be discussed in Chapter 3. Chapter 4 will provide detailed specimen data, while Chapters 5, 6, and 7 will discuss the results from the crush tests. Conclusions and recommendations for future work will be given in the final chapter.

Chapter 2 Experimental design

2.1 Specimen parameters

As stated earlier, the three specimen parameters that were varied in this study were material type, geometry, and stacking sequence. The material used for this work was epoxy pre-impregnated tow using T300 12k and Fortafil 50k carbon fiber. In order to manufacture tubes, this material was filament wound over aluminum mandrels. Two different stacking sequences were used to make tubes for each material/geometry combination.

Two mandrels with different cross-sectional geometries were used in the manufacture of the tubes. Each mandrel was 1.4 m in length, which provided enough length to wind about 840 mm of usable tube. These mandrels were slightly tapered to facilitate the removal of the finished tube. The first mandrel was circular in cross section with a diameter of about 50 mm. The second mandrel had a square cross section that was about 62 mm per side. The corners each had a radius of 12.7 mm. Because the tubes were wound on these mandrels, they had inner surfaces quite similar in dimension to the particular mandrel used. Three specimens were cut from each tube: either two static specimens and a single dynamic specimen, or a single static and two dynamic specimens, as seen in Figure 2-1. The single specimen was always cut from the middle of the uncut 840 mm long tube. A 30° external bevel, used as a crush initiator, was ground into the smaller end of each specimen. This 30° bevel is seen in Figure 2-2. The static specimens were cut to a length of 150 mm, while the dynamic specimens were 300 mm long. The dynamic specimens had to be long so that they could be impacted at a reasonable speed. Ideally, the specimens would be longer, but this compromise was reached so that three specimens could be cut from each 840 mm usable length.

Static/dynamic/static scheme**Dynamic/static/dynamic scheme****Figure 2-1: Cutting schemes****Figure 2-2: 30° external bevel**

Of the two different families of stacking sequences investigated, the first had all $\pm 45^\circ$ layers, while the second family consisted of both $\pm 45^\circ$ layers and 0° layers. To obtain approximately the same wall thickness for each fiber type, the tubes wound with the 12k material had twice as many layers as the 50k tubes. For the first family, the 12k tubes were wound with eight $\pm 45^\circ$ layers and the 50k tubes had four $\pm 45^\circ$ layers. For the second family, one fourth of the $\pm 45^\circ$ layers were replaced with two 0° layers (because each $\pm 45^\circ$ layer is essentially two layers: a $+45^\circ$ layer and a -45° layer). To keep the stacking sequence somewhat symmetric, the 0° layers were separated. The

stacking sequence for the 12k tubes was $[\pm 45^\circ/0^\circ/\pm 45^\circ/0^\circ/\pm 45^\circ/\pm 45^\circ/0^\circ/\pm 45^\circ/0^\circ/\pm 45^\circ]_T$, while the stacking sequence for the 50k tubes was $[\pm 45^\circ/0^\circ/\pm 45^\circ/0^\circ/\pm 45^\circ]_T$.

2.2 Static testing

The static testing was performed at Virginia Polytechnic Institute and State University, commonly known as Virginia Tech. The static test setup is shown by Figure 2-3. These tests were done on an

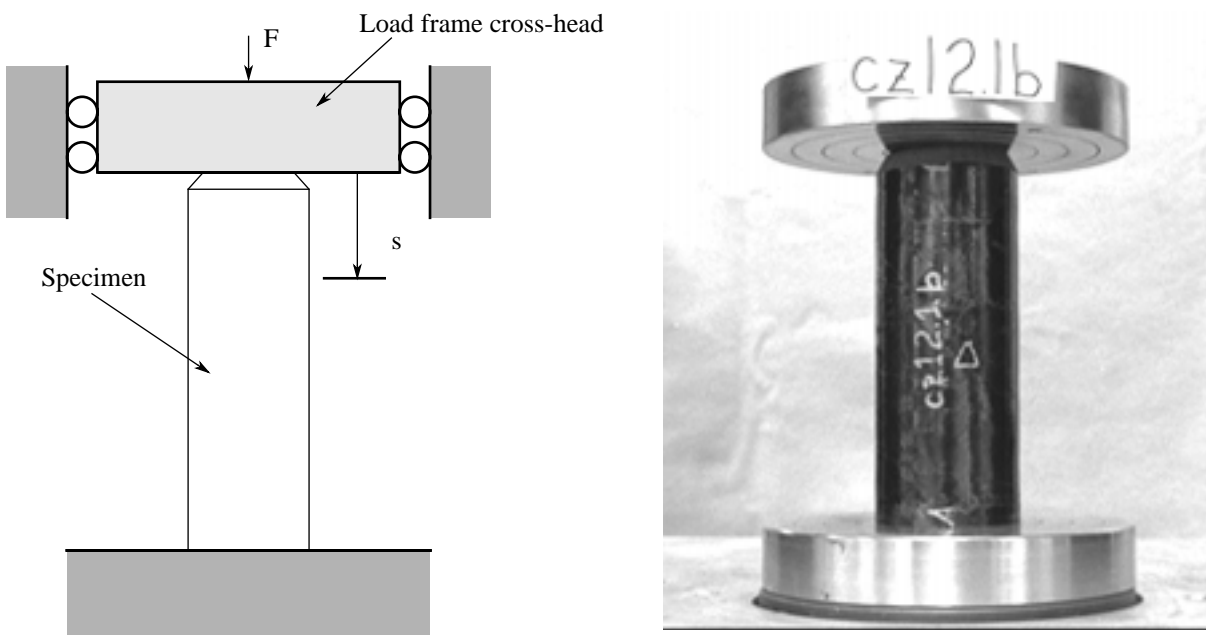


Figure 2-3: Schematic and picture of the static test setup

Instron model 4206-006 displacement-control machine with a 44.5 kN load cell. The cross-head speed was set at 6.35 mm/minute. The static specimen was placed on the stationary lower platen with the beveled end up. The cross-head was then lowered until the upper platen was just touching the specimen. The cross-head was then set into motion and the load and cross-head displacement were recorded for each test. For the initial static tests, a ball and socket device was used to ensure that the load was evenly distributed around the specimen. This device was found to cause problems, so use was discontinued after the first four static tests: tests on tubes with the 50k material. In one static test the ball and socket became misaligned to the point that only one side of the tube was being crushed. Some of the static tests were recorded with a video camera.

2.3 Dynamic testing

Dynamic testing was performed at the General Motors Corporate Research and Development Center in Warren, Michigan using a drop tower facility. Figure 2-4 shows a schematic of the drop tower used. The drop tower had a 140.2 kg rectangular drop head that was guided by four cables; one at each corner. The drop head could be raised to a maximum of 7.6 m (12.2 m/s impact speed) above the impact plate. The specimen was potted in an aluminum mounting plate using a hot melt glue, then the mounting plate was bolted to the drop head so that the specimen was oriented with its beveled end down. The drop head was then raised to a predetermined height to give the desired impact velocity. To commence the test, the drop head was released and the specimen impacted the impact plate. To protect the load cells beneath the impact plate there were four Hexcel aluminum honeycomb stoppers which prevented the drop head from directly contacting the plate.

Data were collected during each drop test. Acceleration of the specimen was measured using an accelerometer mounted to the drop head. The impact force of the specimen was measured using load cells mounted beneath the impact plate. Four load cells were used: three arranged in a triangle with the fourth in the middle. Time was also recorded. Acceleration vs. time and force vs. time files for each test were then created for further reduction at a later date. High speed video was taken for each test.

2.4 Specimen material analysis

Several measures were taken to determine the quality and consistency of the specimens. Inner and outer diameters (inner and outer square side lengths were measured for the square tubes), length, and mass were measured for each uncut 840 mm long tube and each specimen. Wall thickness measurements were also made for each specimen. The inner and outer diameters and square side lengths were measured at two locations on each end of the tubes. Length was measured in four places for each tube and mass was measured twice. The wall thickness of the circular specimens was measured in four places on each end, while the square specimens were measured in eight places on each end. The wall thickness was measured on each flat and each corner of each end of

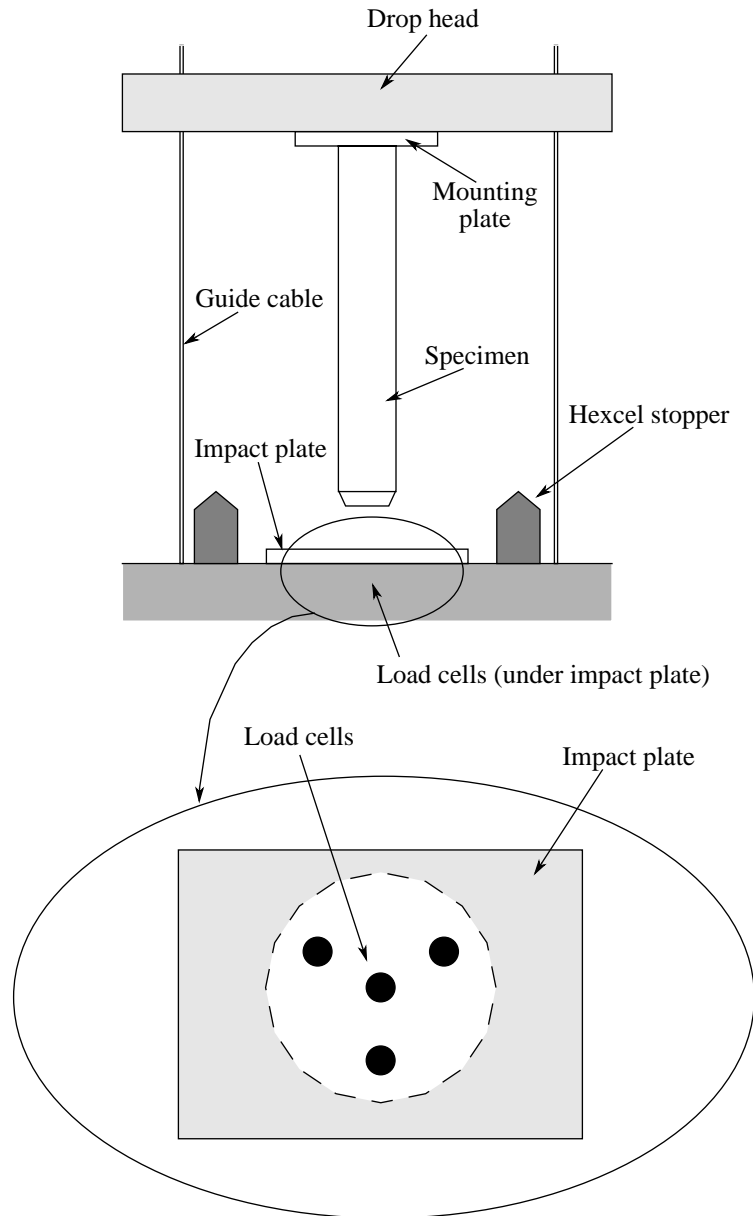


Figure 2-4: Schematic of dynamic test setup

the square specimens because the square tubes were much thinner in the corners than on the flats. The diameters and square side lengths were measured using Fowler Ultra-Cal II. electronic calipers. The lengths of the tubes were measured with a tape measure. A micrometer was used to measure the wall thicknesses. The mass was determined using a Mettler PE 16 electronic scale. Except for four tubes, these measurements were made before any static or dynamic specimens were cut from them. For the first four 50k tubes fabricated, a single static specimen was cut from end before any geometry or mass measurements were made. These four specimens were used as

calibration specimens.

A distinct fiber pattern was created during the filament winding process. The tows winding one way ($+45^\circ$) all crossed the tows that were wound the other way (-45°) at the same axial position, and at regular intervals (for a constant cross-section mandrel). It was postulated that the crushing characteristics of a tube might be different where the tows crossed, so the distance of each of these areas of overlap from the beveled end was measured for each of the specimens (except the first four 50k static specimens mentioned above).

The water displacement technique was used to measure the volume of each tube. A large graduated cylinder, as depicted in Figure 2-5, was fabricated for this purpose. A 102 mm diameter clear acrylic circular cylinder had a plate bonded to one end to form a base and watertight seal. A 51 mm acrylic rod was placed into the acrylic cylinder and the cylinder was filled with water. The initial water level was measured with a scale mounted to the cylinder. The composite tube was then placed in the water and the change in water level was recorded. The acrylic rod was used to reduce

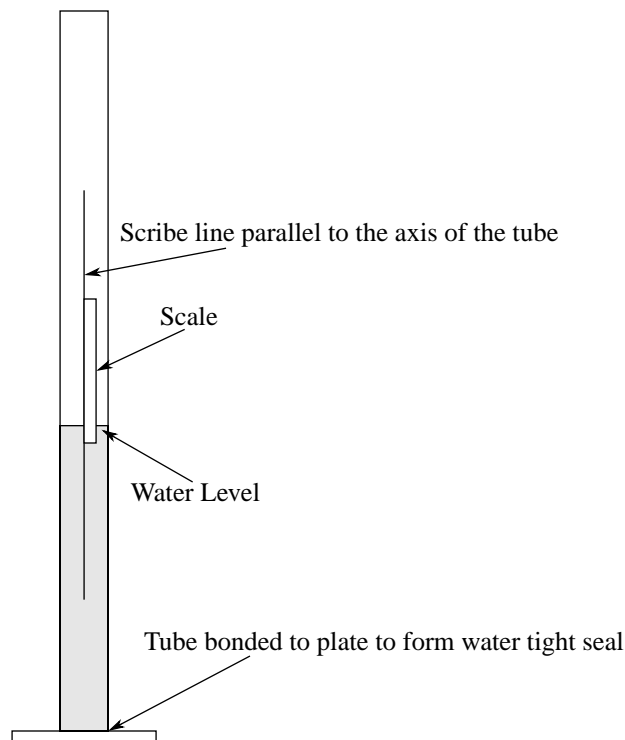


Figure 2-5: Volume measure

the volume of water inside the cylinder so that the composite tube would cause a larger change in the water level, which in turn would be easier to measure. This volume measurement was also made after the first static specimen had been removed from the first four 50k tubes. The volume of each tube was measured in this manner three times: each measurement on a separate day after the tube had had time to dry completely.

For four tubes, one cut end was polished. The end was first trued on a grinding wheel. Next the end was sanded with 320, 400, and then 600 grit sandpaper to a good finish. A one micron alumina slurry and a polishing wheel were used as a final polishing step. Once a good finish was obtained, photographs of the ends were taken to observe the voids and other imperfections.

2.5 Reduction of data

The most important parameter that was determined from each crush test was the specific energy absorption (SEA). The process for obtaining the SEA was slightly different for the static and the dynamic tests due to the different data collected in each. Energy is the product of the force and distance moved at that force level. The crush load, F , and crush length, s , obtained from the static and dynamic tests are shown in Figure 2-3 and Figure 2-6, respectively. The energy absorbed dur-

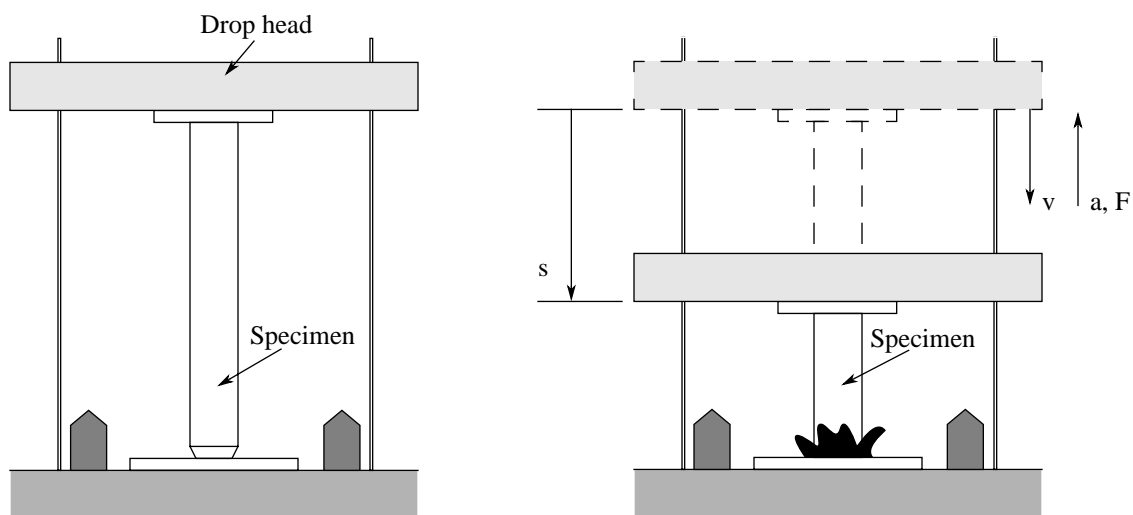


Figure 2-6: Definitions of quantities from the dynamic test

ing crush, E , was then calculated by integrating under the crush load vs. crush distance curve,

$$E = \int_0^{s_f} F \cdot ds, \quad (2-1)$$

where s_f is the final crush length.

The average crush force was calculated continuously as the tube was crushed, as follows:

$$F_a = \frac{\int_0^s F \cdot ds}{s} \quad (2-2)$$

To calculate the load ratio, using Equation 1-1, the value of the crush load at the initial peak, F_{imax} , was divided by the average crush load,

$$load\ ratio = \frac{F_{imax}}{F_a} = \frac{F_{imax}}{\frac{\int_0^{s_f} F \cdot ds}{s_f}} \quad (2-3)$$

To get the SEA, the energy absorbed during crush was divided by the mass of the crushed material, m_c . The crushed mass was found by the following:

$$m_c = m_l \cdot s_f, \quad (2-4)$$

where m_l is the linear density or mass per unit length of the tube. The linear density was determined from the length and mass measurements from each specimen.

During the static tests, the force and cross-head displacement (crush distance) were measured directly. In the dynamic tests this was not possible. During the dynamic tests the acceleration, a , of the drop head and the force on the impact plate were sampled at a rate of 20000 s^{-1} . From these data the requisite information could be determined.

The crush distance was obtained by employing Newton's Second Law:

$$\Sigma F = m \cdot a, \quad (2-5)$$

where m is mass and a is acceleration, which can be rewritten as

$$\Sigma F = m \frac{dv}{dt}, \quad (2-6)$$

where v is the drop head speed and t is the time, and in the case of the dynamic tests becomes

$$\int_{t_0}^t (F - m_{dh}g) dt = m_{dh}(v - v_0), \quad (2-7)$$

where t_0 is the time of impact; m_{dh} is the mass of the drop head, mounting fixture, and specimen; g is the acceleration due to gravity; and v_0 is speed at impact. Rearranging, Equation 2-7 becomes:

$$v = v_0 + \frac{1}{m_{dh}} \int_{t_0}^t (F - m_{dh}g) dt \quad (2-8)$$

To obtain crush distance, v is integrated over time:

$$s = \int_{t_0}^t v dt \quad (2-9)$$

As a check, the acceleration was integrated over time to obtain the drop head speed and then the crush distance:

$$v = \int_{t_0}^t a dt. \quad (2-10)$$

Equation 2-9 was again used to determine the crush distance.

All the integrations described above were done numerically, using the trapezoidal rule. For the static tests, the crush load and crush distance were measured, while for the dynamic tests, the crush load and crush distance were obtained from integration. Equation 2-1, and Equation 2-4 are then applied to calculate the SEA as follows:

$$SEA = \frac{E}{m_c} = \frac{\int_0^{s_f} F \cdot ds}{m_l s_f}. \quad (2-11)$$

It should be noted in Figure 2-6 that the direction of velocity and distance shown are the directions considered positive for purposes of plotting. Obviously, from Newton's Law, in reality, the directions of $+s$, $+a$, and $+F$ should be the same, unlike the figure.

Chapter 3 Specimen manufacture

3.1 Choosing a system

As has been established, filament winding with Thiokol towpreg was the approach used to make tubes, but several methods of manufacture and material systems were initially considered for this project. Resin transfer molding (RTM) was the first manufacturing method considered. With RTM, a fiber preform is placed in a sealed mold and then the resin is pumped into the mold to fill all the remaining space in the mold. Few universities have the capability to RTM tubes (most concentrate on flat plates alone). However, North Carolina Agricultural and Technical State University (A & T) has a laboratory, under the direction of Bob Sadler, that concentrates on the manufacture, including RTM, of tubular composite specimens. Working at the A & T laboratory, several tubes were manufactured for this project. Dow Tactix 123 epoxy resin was used along with biaxial braided fiber preforms from Atkins and Pearce Technology, Inc. [34]. Three fiber types were used for the braids: AS4 6k, AS4 12k, and Zoltek Panex 48k. Logistical problems prevented the continuation of the RTM effort with A & T. With the fiber coming from one supplier; the resin from another; and with the manufacture taking place off-campus at A & T, which had its own projects requiring the RTM facility, it was felt too much of this research effort was controlled by the schedule of others.

Because the RTM approach was not considered viable without building equipment, the next manufacturing method considered was filament winding on the Virginia Tech campus, in particular, wet filament winding with vinyl ester resins. With wet winding, dry fiber is passed through a bath of liquid resin. As the fiber passes through this bath, it picks up resin. The automotive industry uses vinyl ester resins extensively, so it was natural to consider vinyl esters for the present

research. Unfortunately, vinyl ester emits styrene, which is quite odoriferous and may soon have environmental restrictions. The Dow Chemical Company, in Freeport, TX [35], has developed a filament winding facility to address these issues. The key to their facility is a tent-like enclosure for the filament winder. It was decided that, although building such a facility at Virginia Tech was relatively straight forward, it was not compatible with the other uses of the laboratory where the filament winder was located. It was, therefore, decided not to use vinyl ester. With vinyl ester eliminated as a resin system, epoxy was chosen as the matrix material, and specifically, the tow-preg material from Thiokol was chosen.

There are several benefits to filament winding with towpreg. The Thiokol towpreg is made with a variety of fiber types, and with a number of variations of a proprietary epoxy resin. This enabled the resin system to be kept constant while two fiber types were used. Wet winding would involve the preparation of the resin bath before each winding session. The resin would have to be mixed with the curing agent, catalysts, inhibitors, etc. Also, it would have been somewhat difficult to keep constant the amount of resin picked up by the fiber as it passed through the bath. The tow-pregging system allowed the resin content to be controlled more closely. Cleanup was also much simpler with towpreg than it would have been with a resin bath.

3.2 Manufacturing equipment

The filament winder used was a Composite Machines Company (CMC) [36] ULD winder. Figure 3-1 shows a photograph of the filament winder with one of the tubes from this study being wound. The filament winder has two degrees of freedom: the mandrel rotates and the feed eye moves parallel to the rotational axis of the mandrel. The winder is controlled by a PC-based computer, and the winding pattern is generated using software called CADWIND 5.0, which CMC provided with the winder. Once the pattern is calculated by CADWIND, it can be converted to the machine language for the CMC software that actually controls the winder. There are many input parameters for CADWIND, but it is still often difficult to get the exact winding pattern that is desired. The key input parameters are the winding angle and the tow width. In the case of this research, the winding angle, the angle that the fiber makes with the rotational axis as it is laid down, was 45° .

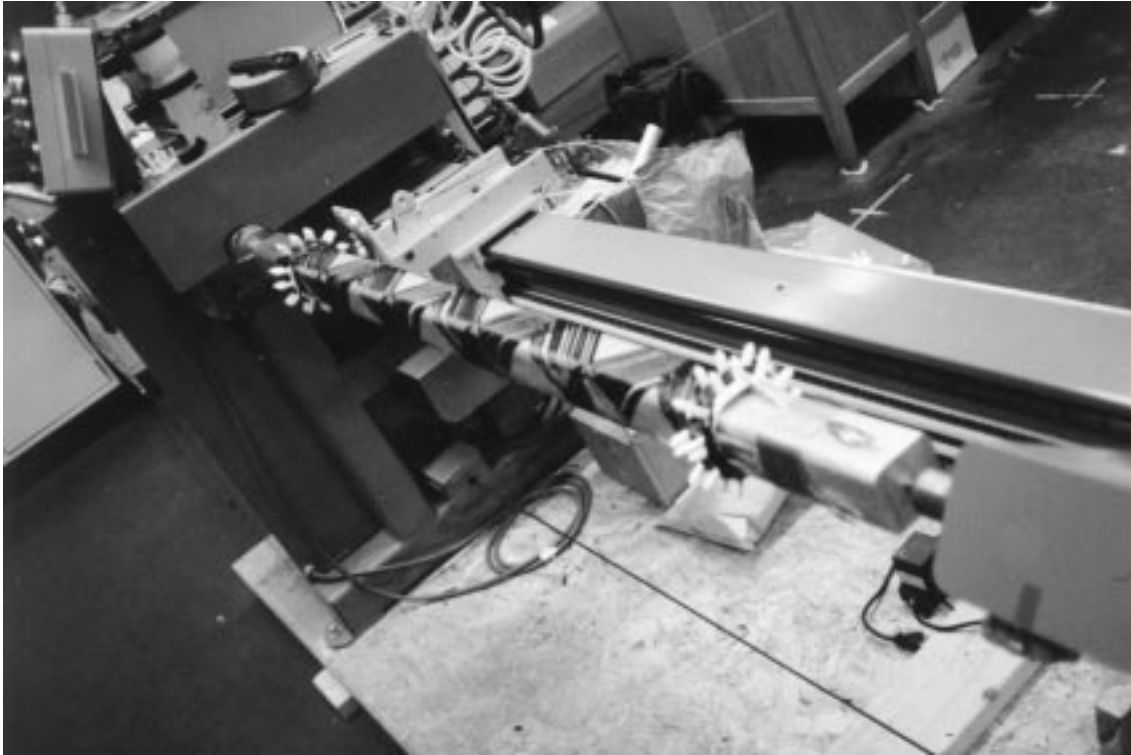


Figure 3-1: CMC filament winder with square tube being wound

The tow width determines how close to one another adjacent tows are placed. Ideally, the tows are placed right next to each other, with little or no overlap or gaps between the tows.

A circular cross-section mandrel and a square cross-section mandrel were made for the filament winder. The square cross-section mandrel and an uncut 840 mm square tube are shown in Figure 3-2. Each mandrel was machined from solid aluminum bar stock. As stated earlier, the mandrels were slightly tapered to facilitate the removal of the finished tube. The circular mandrel had a large diameter of 50.8 mm and was tapered to 47.5 mm. The square mandrel was 62.3 mm per side on the large end and 61.1 mm per side on the smaller end. The corners had a constant 12.7 mm radius. Each mandrel was 1.4 m long. The mandrels were made from aluminum so they would be reasonably light and easily machined. The circular mandrel was made solid because of the availability of round solid aluminum stock. The square mandrel was made solid because aluminum tubing with the proper dimensions was difficult to find, and so that the heat transfer characteristics would be similar to those of the round mandrel, thereby leading to similar heating and cooling characteristics during cure. The tubes were cured in a large autoclave, but only the tem-



Figure 3-2: Aluminum mandrel used for filament winding the square tubes with uncut square tube

perature control of the autoclave was utilized; it was not pressurized. The autoclave was used because no other oven large enough to accommodate such long mandrels was available.

3.3 Manufacturing technique

The first step in the manufacturing process was to cover the mandrel with nonporous Teflon[®] cloth. The cloth was cut to size and then taped, with care to eliminate wrinkles, onto the mandrel. Next, a set of radially oriented plastic spikes, called pin rings, was taped to each end of the mandrel in the turnaround zone, the zone where the tow reverses direction, of the mandrel. These pin rings, which can be seen in Figure 3-1, catch the tow as the feed-eye passes so that the turnaround zone can be shorter in length. Without the pin rings, friction and the tow tackiness would be the only resistance to fiber slippage in the turnaround zone.

Next, the fiber spool was put on a tensioner and the tension was set. For most of the 12k tubes the tension was set to about 4.4 N, and for most of the 50k tubes the tension was set to about 11N. The tow was then secured to the mandrel and the winding program was executed.

For the tubes with 0° layers, the machine was stopped at the end of the $\pm 45^\circ$ layer which would be inside the 0° layer. The 0° tows were then hand laid, being careful to minimize overlap and gaps between the tows. After the 0° layer was down, the winder was started again and a $\pm 45^\circ$ layer was wound over the 0° layer.

After all layers were down, the pin rings and the fiber in the turnaround zone were cut off the mandrel. Shrink tape was then applied over the tube to help in consolidation. Shrink tape contracts as it is heated so it would apply pressure to help compact the tube that it was wrapped around. The shrink tape used was B-500 30.5 μm thick tape from Flexicon Pacific Inc. [37]. Two layers of 51 mm wide tape were wound over the towpreg on each tube. The tape was overlapped about 6 mm as it was wound. The square tubes had one more step before going to the oven. The shrink tape that was wound directly around the square tubes would only compact the corners; because of the square geometry, the tape applied very little pressure on the flats. To counter this, a way to provide pressure to the flats was devised. Four extruded aluminum tee sections, each with a 51 mm base and a 51 mm flange, and each long enough to cover the length of the wound tube, were purchased. These aluminum tees were positioned, one on each flat side of the tube, and two layers of 25 mm wide shrink tape were wound over the tees (see Figure 3-3). This shrink tape pulled on the webs of the tees to compress the flanges against the flats of the tube. A silicon rubber mat was placed between the tees and the tube as the tubes were positioned so that the pressure would be distributed evenly and there would be no sharp lines where the tee and the tube met. Figure 3-4 shows the application of shrink tape over the tees.

Once the shrink tape was applied, the tubes were taken to the autoclave for curing. The cure cycle used was a typical ramp-hold cycle, consisting of a 2.8° C/min ramp from room temperature to 132° C. The temperature was held at 132° C for 4 hours and then cooled at 2.8° C/min.

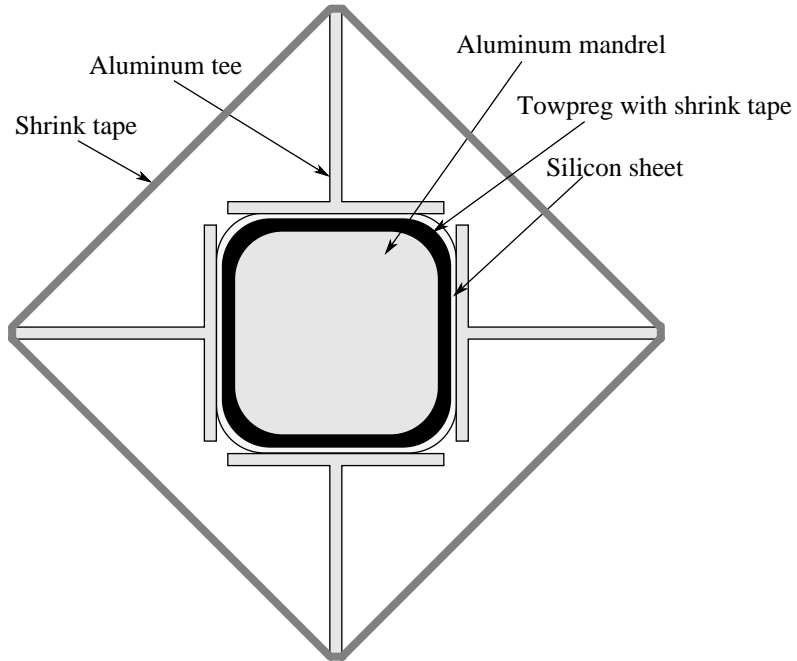


Figure 3-3: End view schematic of shrink wrapping with the aluminum tees



Figure 3-4: Shrink wrapping over the aluminum tees

When the tube was cool, the shrink tape was removed and the tube was removed from the mandrel. The ends of the tube were irregular so they were cut off with a diamond bladed band saw and then trued with a disc sander. The full tubes were then weighed and measured for all of the relevant dimensions, and cut into the shorter static and dynamic specimens with the band saw. The sander was again used to true the ends of the specimens and then to apply a 30° bevel to the smaller diameter or square side length end of each specimen (recall Figure 2-2). The specimens were also individually weighed and measured, both before and after the bevel was applied. The angle of the bevel was kept constant using a bevel protractor with the disc sander. The edge of the specimen was held against the bevel protractor as the specimen was slowly turned to produce an even bevel around the entire circumference of the specimen.

3.4 Problems encountered

Several problems were encountered during the manufacturing process, but none were insurmountable. Lack of familiarity with working with the Thiokol towpreg was the source of several of the problems. The 12k material was easier to wind than the 50k material. The fact that the towpreg is tacky (which helped with consolidation and placement) caused two problems. As the material was unwound from the spool, sometimes several fibers within the tow would separate from the tow and stick to the spool. Since the fibers are continuous, these fibers would often remain stuck to the spool and even more fibers would separate from the main tow. If these separated fibers were not noticed early, they could potentially grow in number and, although it never happened, even break the winding tow. Once the problem was noticed, the filament winder was stopped and the separated fibers were removed from the spool.

The tackiness of the towpreg also caused a problem of another sort. As the tow passed over the feed-eye, which placed the fiber onto the mandrel, sometimes the friction and tackiness would cause some of the fibers to be pulled away and to ball up on the eye. This problem was exacerbated by high winding tensions because the friction between the tow and the eye was directly related to the tension in the tow. Because Thiokol recommends fairly high winding tensions for the 50k material, the problem was seen more often with the large tows. Thiokol's winding tension

recommendations were not able to be met because too much fiber would ball up on the eye. Several other measures could have been taken to help alleviate this balling problem. Winding could have been done in a colder environment because the resin is less tacky at lower temperatures, or the feed-eye could have been modified so that the tow would never pass over a static surface (which Thiokol recommends). Some experimentation was done with the feed-eye, but no reasonable design was found until almost all tubes had been wound.

Another problem was programming the CADWIND software to obtain the correct spacing of adjacent tows. Again, the 50k material caused more problems than the 12k tows. The 50k tows varied in width much more than did the 12k tows. In addition, in the length of tow between the spool and the mandrel, the 50k tow material often curled across the width. This curling caused added variations in tow width. These variations caused unwanted gaps between tows on the first four of the 50k tow tubes. The unwanted gaps between tows caused voids in the finished tubes. To minimize this problem, the spacing of the tows was reduced for the winding of the remaining four 50k tow tubes.

There were also problems with the shrink tape. The first shrink tape that was tried, Dunstone Company's [38] Hi-Shrink polyester tape, could not be removed from the composite tube after curing; the Hi-Shrink Tape bonded to the epoxy. The Flexicon Pacific B-500 tape, a polypropylene tape, was much better. The Flexicon Pacific tape would also stick to the tube occasionally, but could usually be removed with extra attention. The Flexicon Pacific tape stuck to the 12k tubes more often than the 50k tubes.

The final problem was really more of an inconvenience than a problem. The winding software CADWIND was difficult to work with. For a given set of input parameters (e.g., tow width, winding angle, etc.) the software would create the machine code as best it could. Unfortunately, often this resulted in unreasonably long winding times for some winding patterns. There was no way to set a fiber pay-out speed or mandrel speed that was the same for all of the winding patterns. The result was that it took from 30 minutes to 3 hours to wind a layer. The 50k round tubes had the shortest winding time per layer, and the 12k square tubes had the longest time.

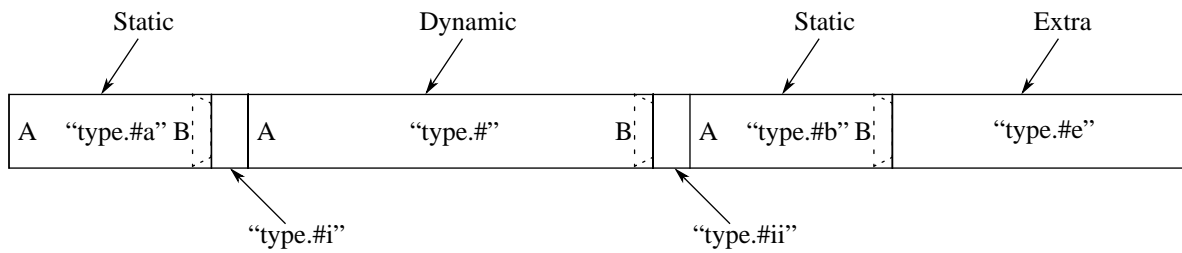
Chapter 4 Specimen description

With two fiber types, two families of stacking sequences, and two geometries, a total of eight tube types were fabricated. At least two 840 mm tubes were made for each of these eight types, for a total of sixteen 840 mm tubes tested. Three other 840 mm tubes were initially fabricated and were used to optimize the manufacturing process and for preliminary testing. As was shown in Figure 2-1, each 840 mm tube had three specimens cut from it. Figure 4-1 shows the specimen names and from where on the 840 mm uncut tube each specimen was cut. For each tube type, the last 840 mm tube manufactured had two dynamic specimens cut from it, while the earlier 840 mm tube had two static specimens cut from it. Figure 4-2 shows photographs of all the tubes before and after they were cut into individual specimens. The tubes are arranged with the 12k tubes and specimens on the left and the 50k tubes and specimens on the right.

4.1 Cutting/labeling scheme

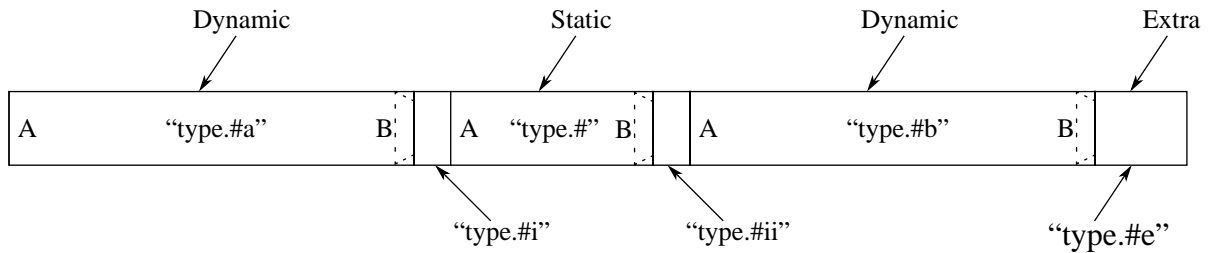
The tube name is a code that gives the tube geometry, stacking sequence, and fiber type. The first character tells the cross-sectional shape: “c” for circular cross section, “s” for square cross section. If there is a “z” in the second position, then that tube has the stacking sequence with the 0° fibers in it. Next, the number, a “12” or “50,” indicates whether the tube has the 12k AS4 or 50k Fortafil fiber tows. At least two tubes were made for each set of parameters. The “.#” indicates the number of the tube wound with that set of parameters. Three tubes were manufactured for two of the sets of parameters.

Static/dynamic/static scheme



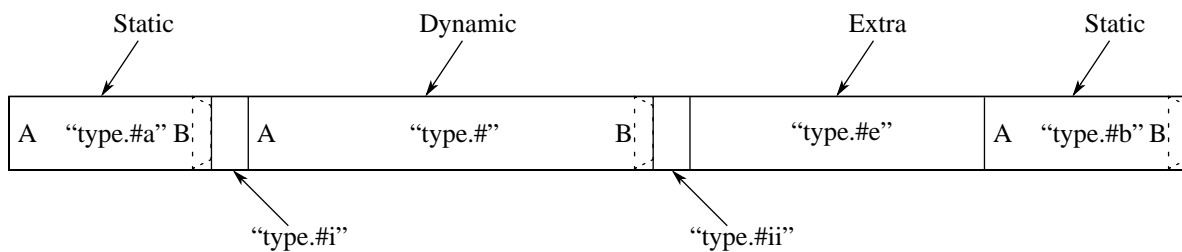
Used for "type.#": c12.2, cz12.1, s12.1, sz12.1

Dynamic/static/dynamic scheme



Used for "type.#": c12.3, cz12.2, s12.2, sz12.2, c50.3, cz50.2, s50.2, sz50.2

Previous static/dynamic/static scheme



Used for "type.#": c50.2, cz50.1, s50.1, sz50.1

Note: The "B" end was always the smaller end and the end that was beveled
The short sections were saved as a record for material characterization tests

Figure 4-1: Cutting and labeling schemes



(a)



(b)

Figure 4-2: Tubes (a) before and (b) after being cut into individual specimens

The specimen name appends the tube name and tells from where along that tube the specimen was cut. Three specimens were cut from each 840 mm tube: either two static specimens and a single dynamic specimen, or two dynamic specimens and a single static specimen. One-inch sections were cut between specimens for possible later material characterization tests. Each 840 mm tube also had some extra length. The two dynamic or two static specimens cut from the 840 mm tube were cut from the ends and given the suffix “a” or “b,” with the “a” specimen coming from the larger end and the “b” specimen coming from the smaller end of the slightly tapered tube. The tube designation was not amended for the singular specimen that came from near the center of the uncut tube. An example of the labeling scheme follows. Given the uncut tube with label “cz12.1”: this was the first tube (“.1”) made that is circular (“c”), has zeros (“z”), and was made from the “12”k fiber. Two static specimens and one dynamic specimen were cut from this uncut tube. The static specimens were labeled “cz12.1a” and “cz12.1b” while the dynamic specimen was labeled “cz12.1”. The labelling scheme is clearly shown in Figure 4-1.

As seen in Figure 4-1, two different cutting schemes were used for the “static/dynamic/static” uncut tubes. The scheme at the bottom of Figure 4-1, labelled “Previous static/dynamic/static scheme,” was used for the first four 50k uncut tubes (c50.2, cz50.1, s50.1, and sz50.1). A static specimen was cut from each of these early tubes and tested soon after manufacture as a check before the other tubes were manufactured. The static specimen was cut from the end because the ultimate length of the specimens and cutting scheme had not yet been decided. These static specimens were cut to 125 mm instead of 150 mm for the same reason. These short static specimens were the “static.b” specimens for these first 50k tubes, specimens labeled: c50.2b, cz50.1b, s50.1b, and sz50.1b.

4.2 Data

After manufacture, it was noticed that the first four 50k tubes had too much space between tows. This adversely affected the consolidation. The tow spacing parameter on the filament winder was, then decreased. Thus tubes c50.2, cz50.1, s50.1, and sz50.1 had a wider tow spacing than tubes c50.3, cz50.2, s50.2, and sz50.2. This spacing difference can be seen in Figure 4-2.

Photographs taken of four polished tube ends are seen in Figure 4-3 (note that the circular tubes are shown at lower magnification than the square tubes). Figure 4-3a and b show well consolidated 12k tubes. Only small voids can be seen in these cross sections. Cross sections of 50k tubes are seen in Figure 4-3b and c. Much larger and more numerous voids are seen in these 50k cross sections because of the rope-like character of the 50k towpreg. In both the 12k and 50k square cross-section tubes, the voids are seen on the flats but not on the corners. This indicates that, even with the precautions taken, there was not as much pressure on the flats as on the corners during consolidation. The corners are also thinner than the flats which is further indication of higher consolidation pressure in the corners. The individual layers for each tube can also be seen in Figure 4-3. It is also seen that the layers of the 50k tubes are much thicker than those of the 12k tubes because the 50k towpreg is thicker than the 12k towpreg.

As described in Section 2.4, several measurements were made to determine material quality and consistency of the specimens. Inside and outside diameters were measured with electronic calipers, while wall thicknesses were measured with a micrometer. The wall thickness of each square specimen was measured both on the flats and in the corners. Lengths and positions of the tow crossings were measured with a tape measure. Mass was measured using an electronic scale and the volumes of the uncut tubes were measured.

To compare the uncut 840 mm tubes and specimens, column charts were made for the relevant measurements. The inside and outside diameters (inside and outside square side lengths for the square cross sections) are seen in Figure 4-4. Figure 4-5 shows the wall thicknesses. The linear density is seen in Figure 4-6. The volume per unit length is shown in Figure 4-7. There are four column labels for each tube in the diameter, wall thickness, and linear density plots. The first label is for the 840 mm uncut tube, while the labels to the right are for the three specimens cut from that tube. Wall thicknesses of the 840 mm uncut tubes were not measured, so there are no columns above spaces with this label. For the volume measurements there is only one label, as volume measurements were only made on the uncut tubes. All measurements and plots were made for the tubes after the first static specimen (static.b) had been removed from the first four 50k tubes (c50.2, cz50.1, s50.1, and sz50.1) and tested. This is the reason for any additional blank spots in

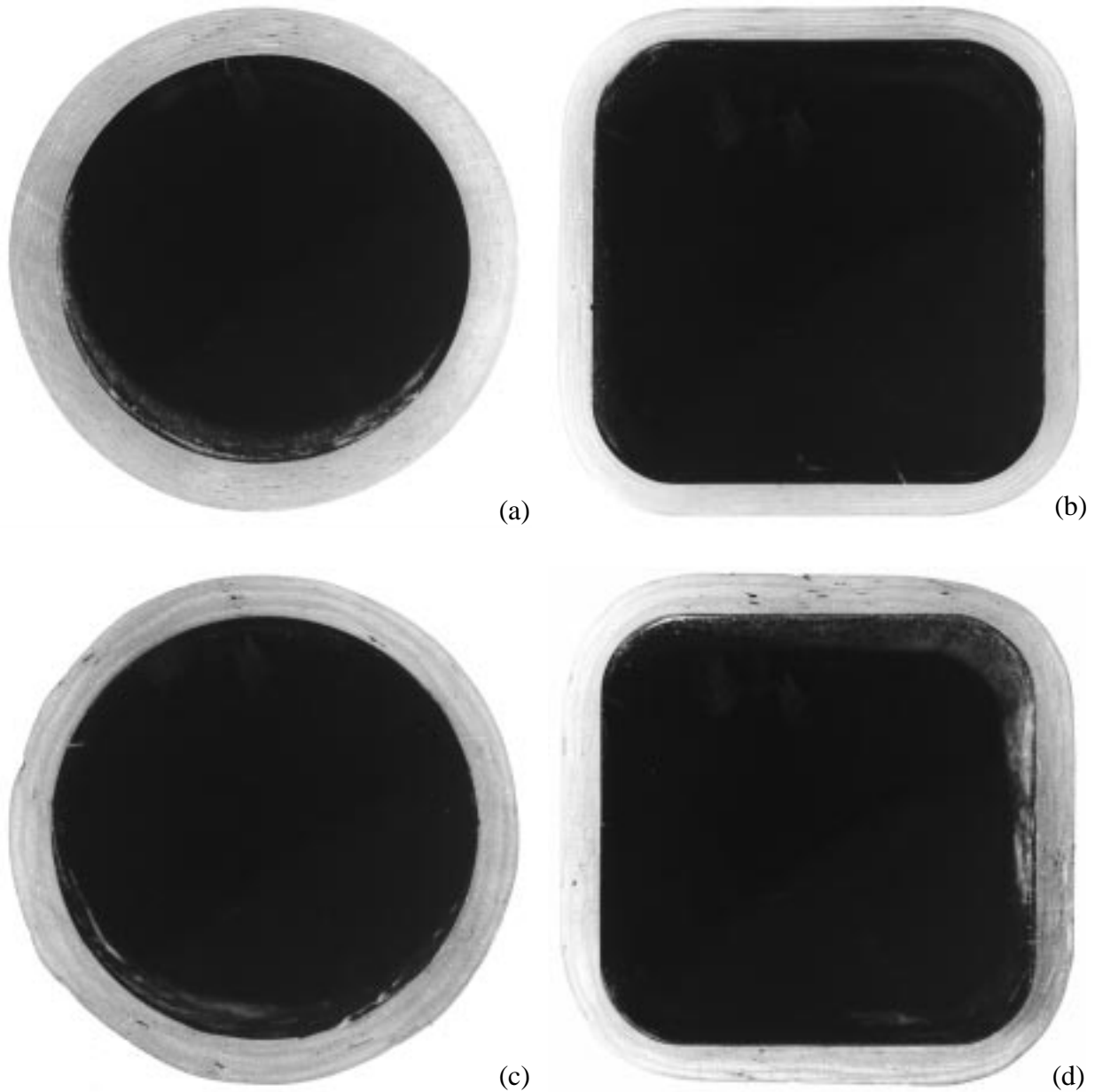
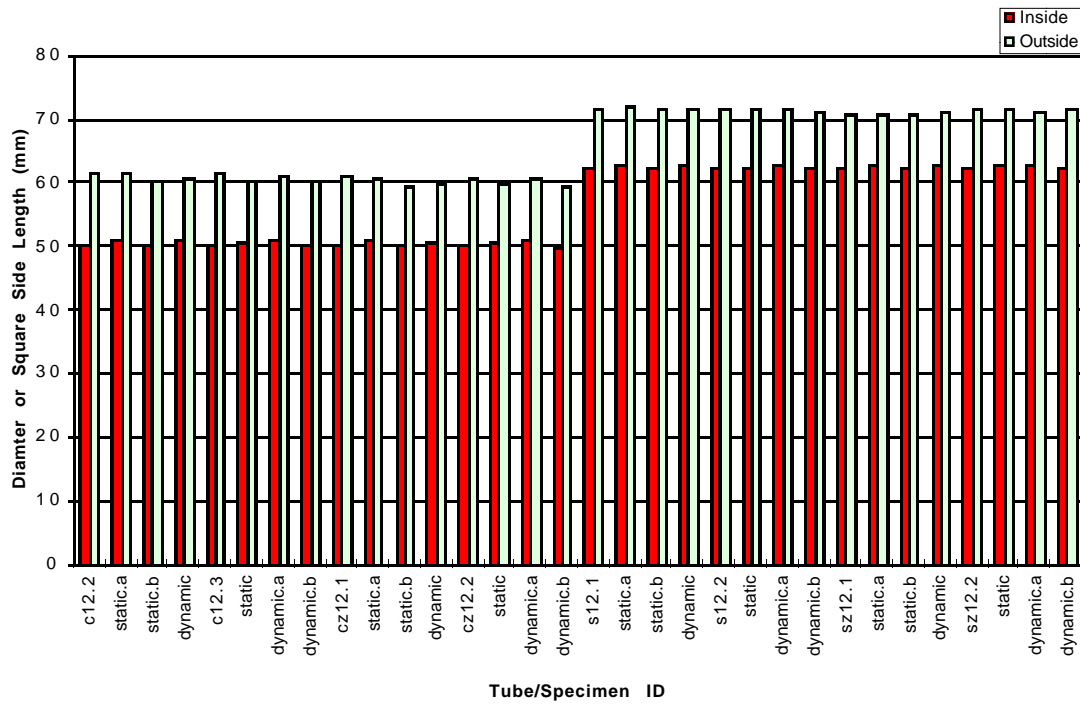


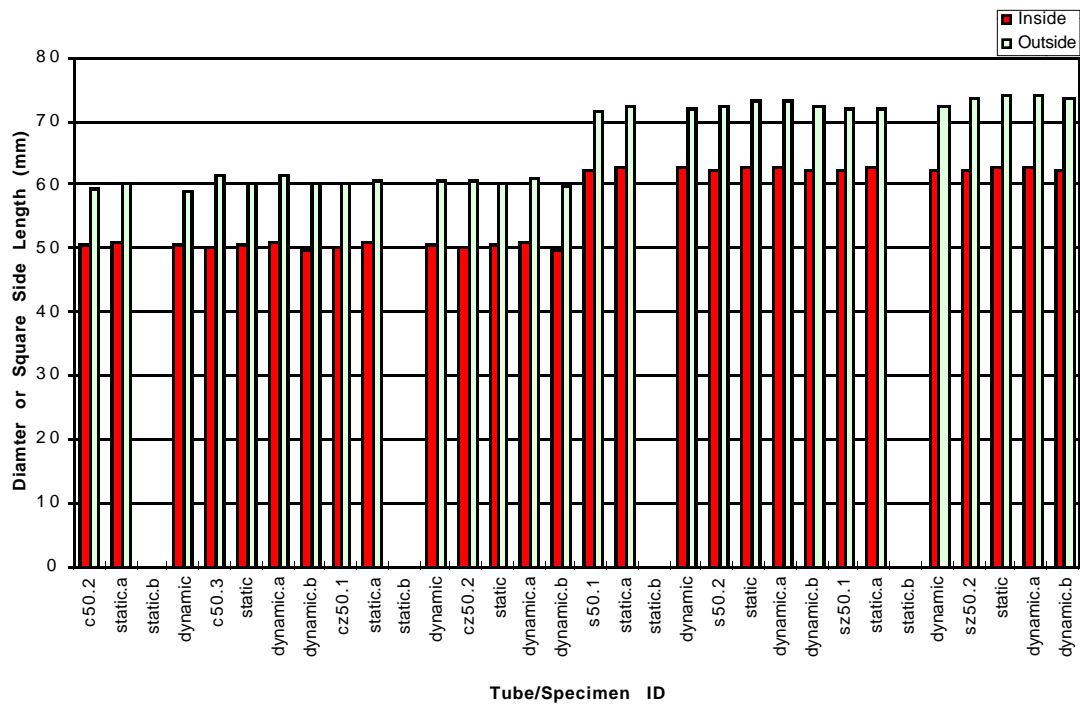
Figure 4-3: Cross sections of specimens (a) c12.2 (b) s12.1 (c) cz50.1 (d) sz50.2

the figures that show the data for 50k tubes. All of these figures (Figure 4-4 through Figure 4-7) were compiled using the averages of all the measurements taken: measurements taken at both ends and all sides, and with repeat measures.

The inside and outside diameters and side lengths are seen in Figure 4-4. The inside measurement is shown by the dark columns while the light columns represent the outside measurement. It is

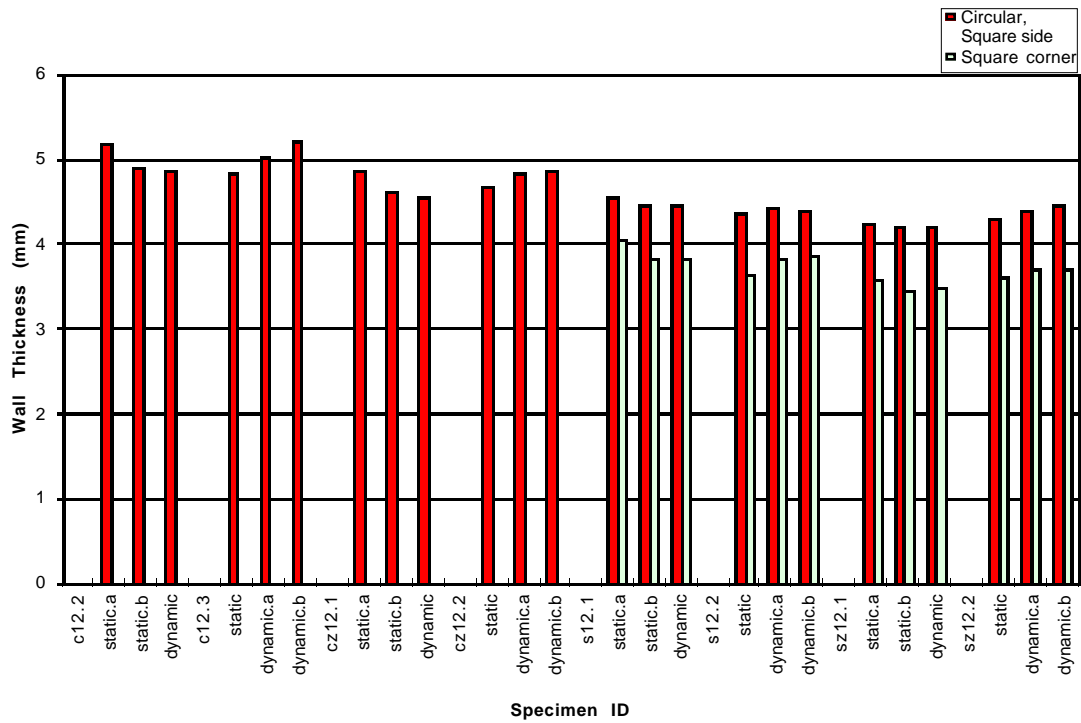


(a)

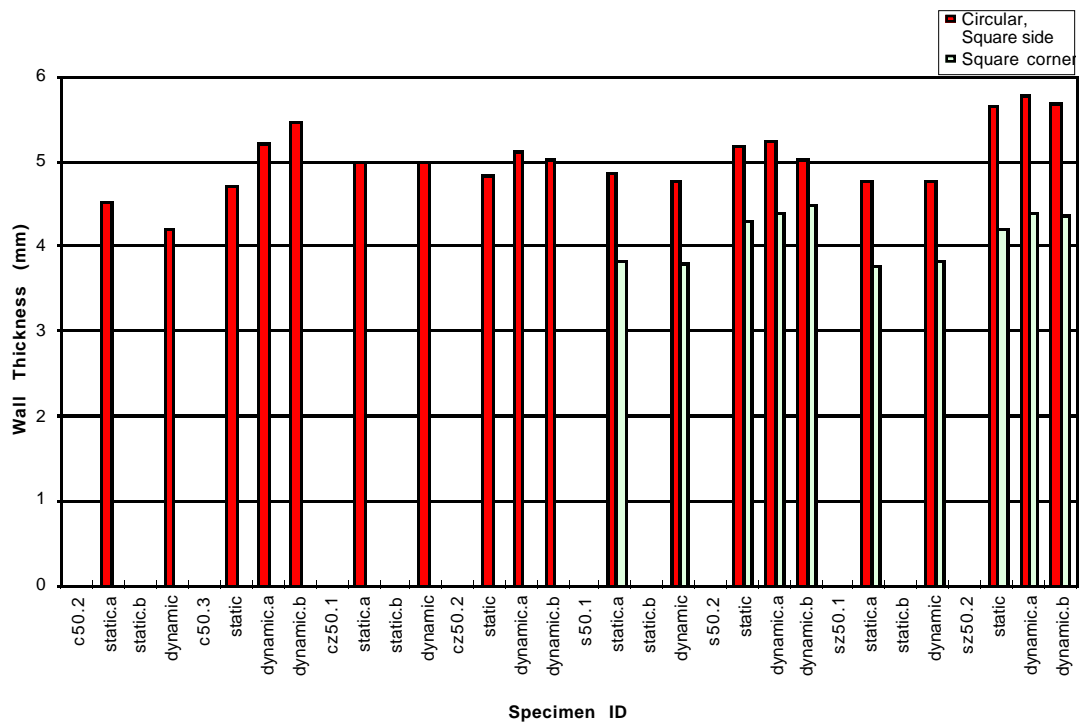


(b)

Figure 4-4: Diameters or side lengths of (a) the 12k uncut tubes and specimens and (b) the 50k uncut tubes and specimens

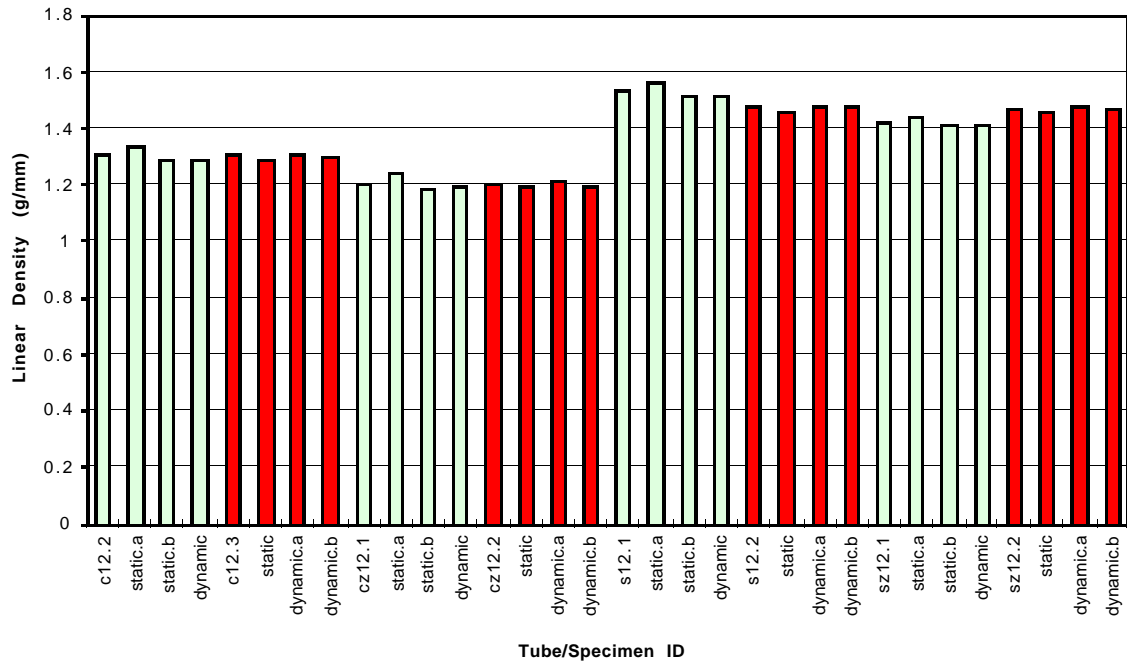


(a)

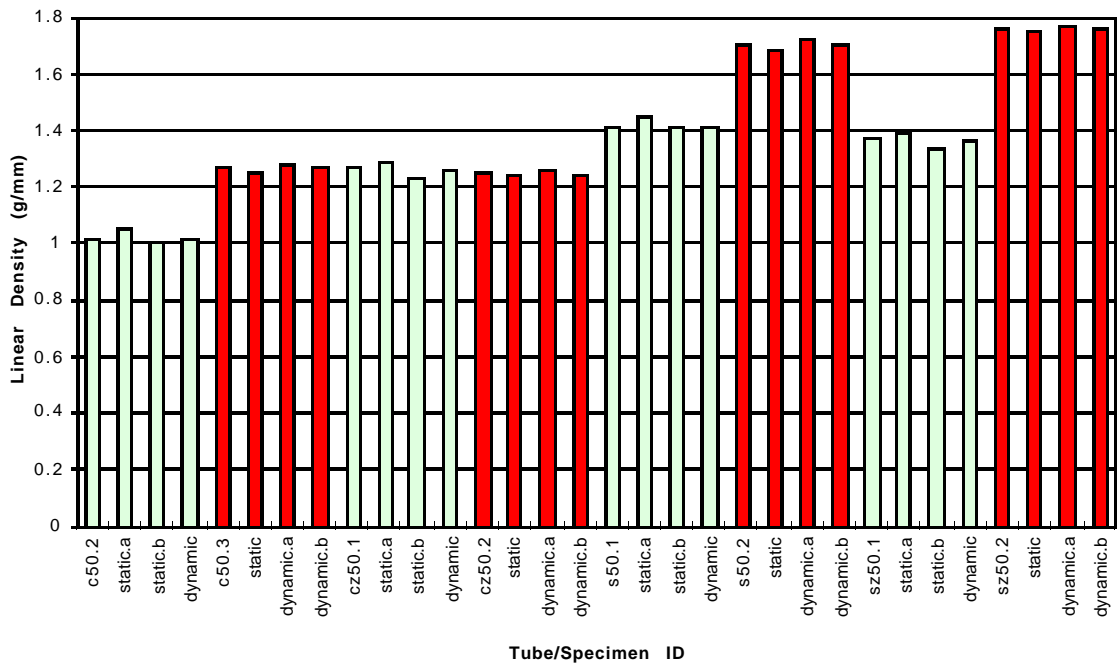


(b)

Figure 4-5: Wall thicknesses of (a) 12k specimens and (b) 50k specimens



(a)



(b)

Figure 4-6: Linear density for (a) the 12k uncut tubes and specimens and (b) the 50k uncut tubes and specimens

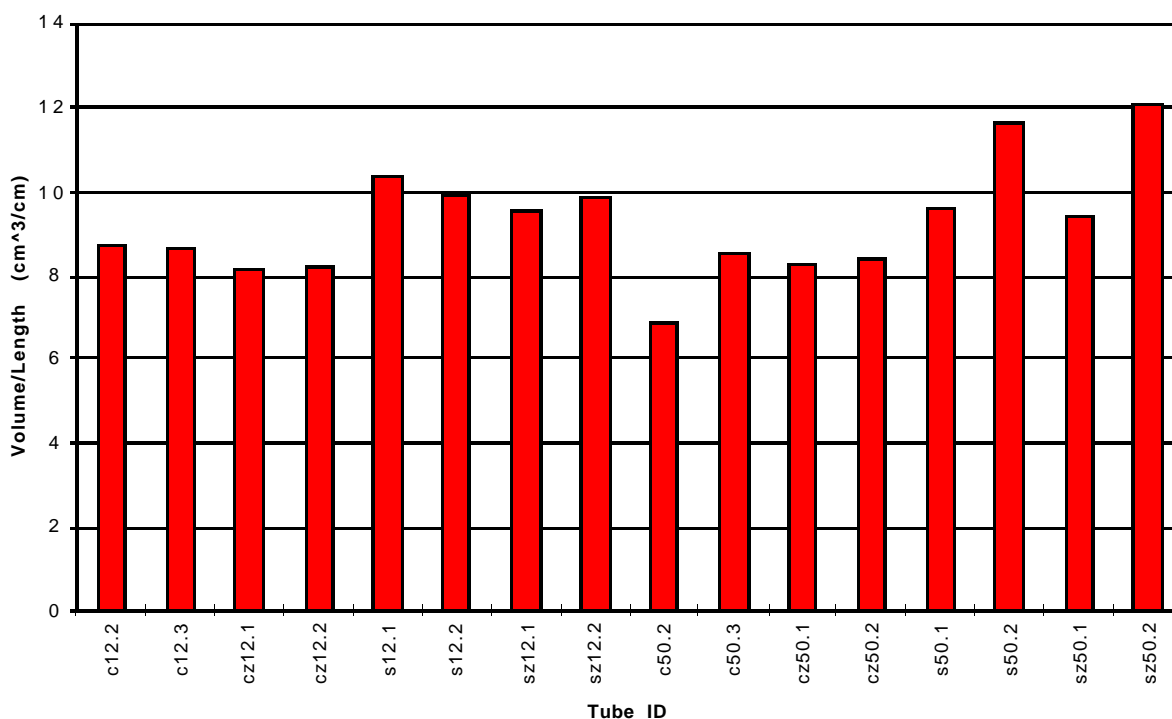


Figure 4-7: Tube volume per unit length

seen that the 12k and 50k circular tubes had similar inner and outer diameters. The 50k square tubes generally had similar inside and slightly larger outside dimensions than the 12k square tubes. The two later 50k square tubes (s50.2, and sz50.2) had the largest outside dimensions of the square tubes.

The measured wall thicknesses are shown in Figure 4-5. The circular specimens have only one column representing the average wall thickness, while the square specimens have two bars. The dark column on the left represents the average thickness of the flats, while the light column on the right represents the wall thickness of the corners. The walls of the 12k circular tubes were all thicker than the walls of the 12k square tubes. Perhaps the filament winder put down more fiber over the surface of the circular mandrel than the square mandrel, even though the tow spacing was set the same. The wall thicknesses for the 50k tubes were more random than the 12k tubes, and there did not seem to be a trend with the circular versus square tubes. All of the 50k tubes, except

c50.2, were thicker (average thickness of the specimens cut from that tube) than their corresponding 12k tube. Also, for all square tubes the thickness in the corners was less than the thickness of the flats. This is indicative of more compaction in the corners.

In Figure 4-6 there is a column for each uncut 840 mm tube and each of the three specimens cut from it. This detail shows how the mass varied throughout the length of the tube. Some variation within an 840 mm uncut tube was expected because of the slightly tapered mandrel. The linear density for the “a” specimen was expected to be greater than that for the “b” specimen because the tapered mandrel had larger dimensions on the “a” end. The specimen cut from the middle of the 840 mm tube was expected to have a linear density between the linear density of the “a” and “b” specimens. It is seen that the mass per length is more consistent for the 12k tubes than for the 50k tubes. The large increase in linear density between c50.3 and c50.2, s50.2 and s50.1, and sz50.2 and sz50.1 is due to the reduced spacing between tows that was used on the later 50k tubes. It is unknown why the same difference between the cz50.2 and cz50.1 tubes was not observed.

Basically the same trends seen in Figure 4-6 are also seen in Figure 4-7 for the volume per unit length. For the 12k uncut tubes there is fairly good consistency in volume per unit length between like pairs. The change in the tow spacing is again seen in three pairs of the 50k tubes: c50.2 and c50.3, s50.1 and s50.2, and sz50.1 and sz50.2. Again, this change is not seen between the two circular 50k tubes with the 0° layers, namely cz50.1 and cz50.2.

Chapter 5 Static energy absorption characteristics

Twenty-four static specimens and twenty-four dynamic specimens were included in this study. The static specimens were all tested prior to the dynamic specimens. The energy absorption characteristics measured and observed during the static tests were used to establish the dynamic test parameters. The static tests also provided information regarding the influence of specimen geometry, fiber angles, and tow size on energy absorption characteristics. The static tests are discussed in full in this chapter, while discussion of the dynamic tests is reserved for Chapter 6. A comparison of the static and dynamic tests is given in Chapter 7.

5.1 Crushing modes

There were several different modes of crush observed during the static crush tests. In all the modes, the wall of the tube was split part way through its thickness and the inside portion of the wall was pushed to the inside of the tube while the outside portion was bent outward. Essentially, if the wall was of thickness H , then the inner portion of the thickness, $H/3$, for example, would be pushed inward and the outer $2H/3$ portion of the thickness would be pushed outward. Between the portion that was pushed inward and the portion that was bent outward, there was a debris wedge. This wedge consisted of pulverized material and probably helped to split the wall. Three distinct crush modes were seen. However, these failure modes were often combined so that several modes would be seen in a single specimen.

There was a *tearing* mode, seen in Figure 5-1, in which the inside portion of the wall folded inward and the outside portion of the wall folded outward. As the outside portion of the wall

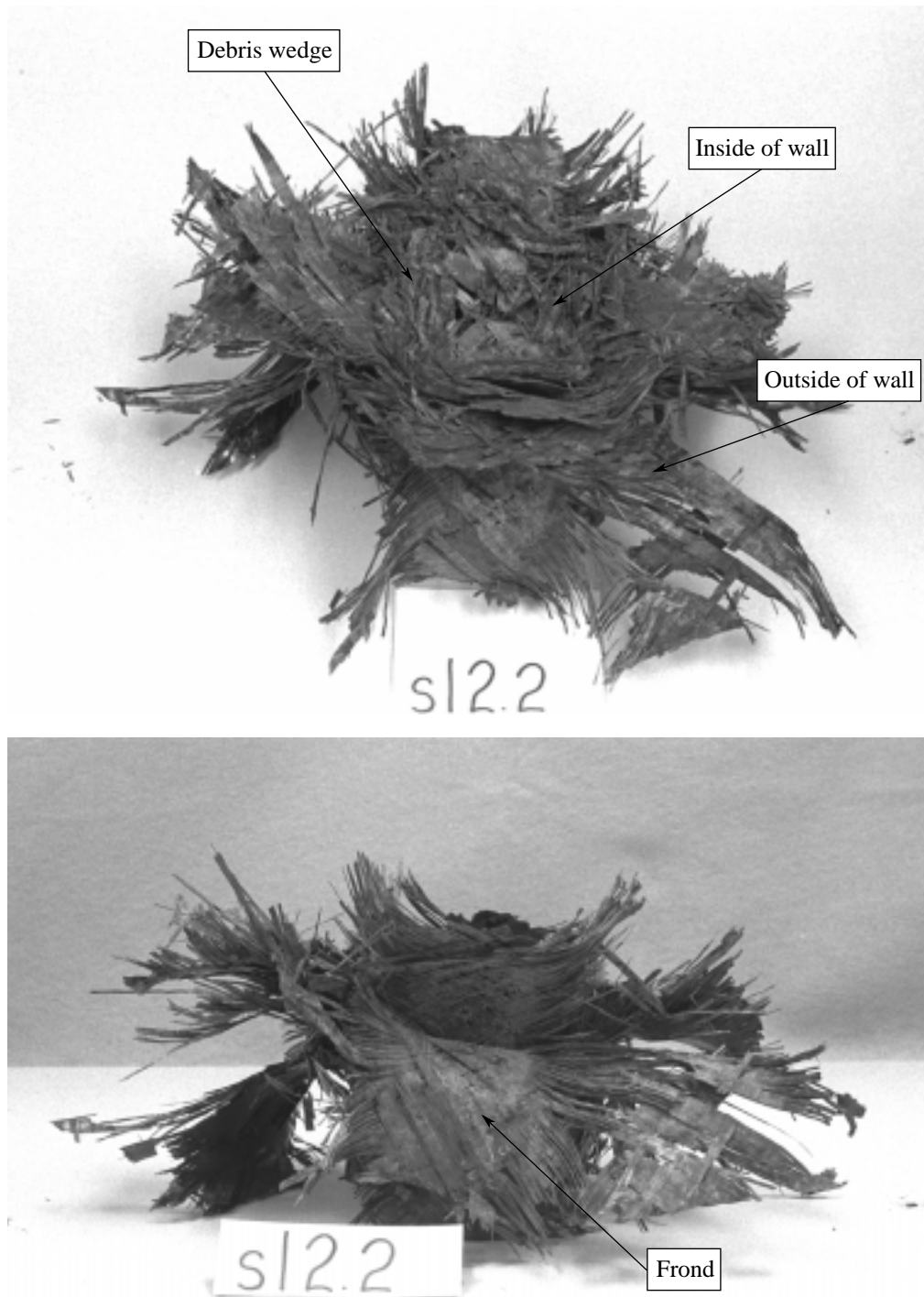


Figure 5-1: Tearing crush mode

folded outward, hoop stresses caused it to tear in several places. Between these tears there was little fiber damage and the wall remained intact, but had matrix damage. These sections between the tears, where the wall was still intact, are often referred to as fronds and are positioned like flower

petals. Occasionally, large pieces of a frond would break off. This tearing mode was similar to the fiber splaying and tearing mode seen by Hull [8].

Another mode, the *splaying* mode, seen in Figure 5-2, was similar to the lamina bending mode seen by Farley and Jones [10] and the fiber splaying and bending mode seen by Hull [8]. In the fiber splaying mode, most of the individual tows were separated, something like delamination but on a tow-by-tow basis. Often the tows were further split by matrix cracks running parallel to the fibers.



Figure 5-2: Splaying crush mode (with socking also seen)

The third failure mode seen during stable crushing was the *socking* mode, seen in Figure 5-3. In this mode, the outside portion of the wall that separated and bent outward stayed together but was



Figure 5-3: Socking crush mode (with splaying also seen)

pushed back over itself, similar to the way a sock comes off the foot when the sock is pulled downward from the top, out and over the foot part of the sock.

5.2 12k specimens

The crush load vs. crush length traces for the static tests of the circular 12k specimens are seen in Figure 5-4, while the traces for the square 12k tests are seen in Figure 5-5. The solid line seen in each figure is the measured crush load at each crush distance, while the broken line represents the crush load averaged over the crush length, as described by Equation 2-2. All of the 12k static specimens were crushed to 100 mm. It is seen that for the 12k specimens, most of the crush load

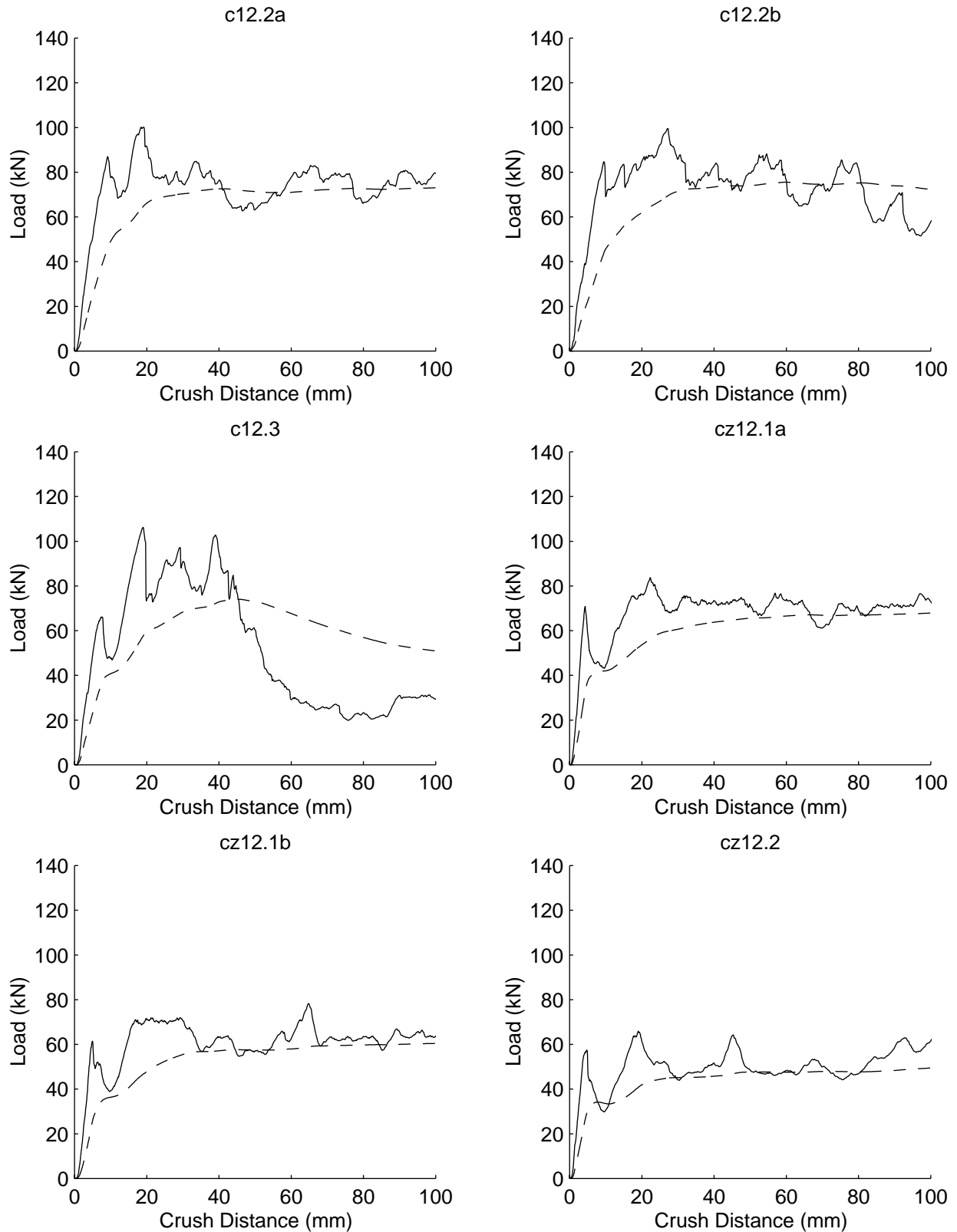


Figure 5-4: Crush load vs. crush length traces for the circular 12k static specimens

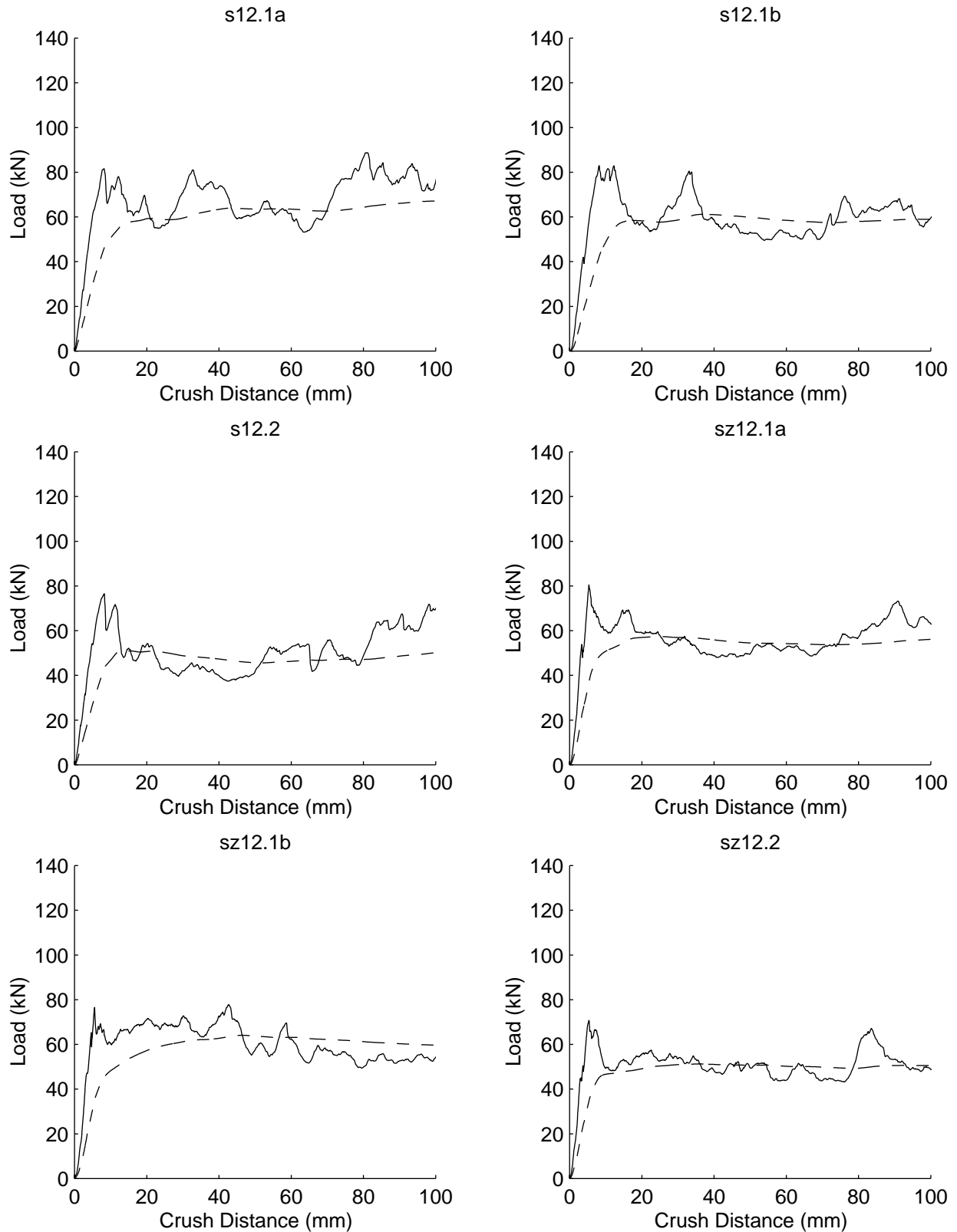


Figure 5-5: Crush load vs. crush length traces for the square 12k static specimens

vs. crush length traces approximate the ideal trace seen in Figure 1-1 in that the trace representing the measured load is relatively flat once it has made the transition from the zero load condition. Most of the measured load traces do, however, have two or three non-distinct initial peaks and large valley-to-peak variations that are not considered ideal.

The average crush loads (averaged over the length of the crush using Equation 2-2) for the 12k specimens are seen in Figure 5-6. In this figure, the two columns together represent the average load of the specimens cut from the ends of the 840 mm tubes (the “a” and “b” specimens, see Figure 4-1), with the dark column representing the “a” specimen and the light column representing the “b” specimen. The columns that stand alone represent the average load of the single specimens cut from the middle of the 840 mm long tubes. It is seen that the circular “a” and “b” specimens had higher average loads than did their corresponding square “a” and “b” specimens, while the single middle specimens from the circular and square 12k tubes had almost identical average crush loads (all within a 1.5 kN band). The 0° layers seem to lower the average load for the “a”

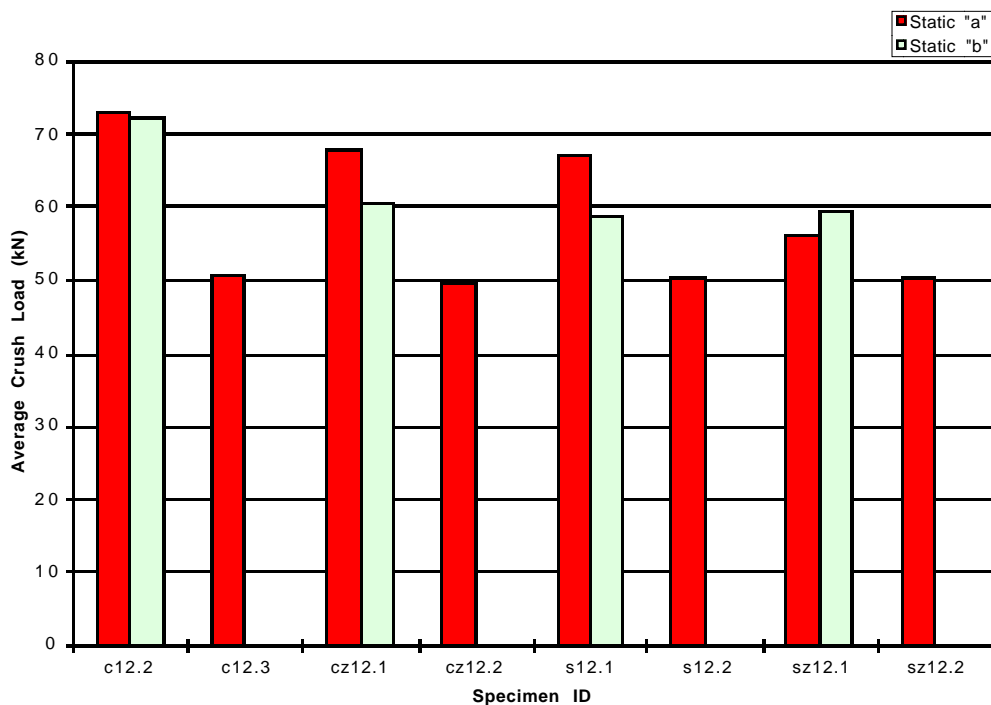


Figure 5-6: Average crush loads of the 12k static specimens

and “b” specimens, while again, no difference is seen among the single middle specimens with or without the 0° layers.

The average load data can be somewhat misleading because the specimens had different mass; most importantly, the square specimens were heavier than the circular tubes. The SEA was considered here as a measure that takes this weight difference into account. Figure 5-7 shows the SEAs for the 12k static tests; the figure is setup in the same manner as Figure 5-6. When normalized by crushed mass, the differences between the circular and square specimens become more apparent. Specifically, it is seen that all of the circular 12k specimens had higher static SEAs than their corresponding square 12k specimens. It is also seen that the “a” and “b” specimens had higher SEAs than the corresponding specimens from the middle of the replicate 840 mm tubes for the 12k static tests. It seems that the 0° layers had little effect on the SEA.

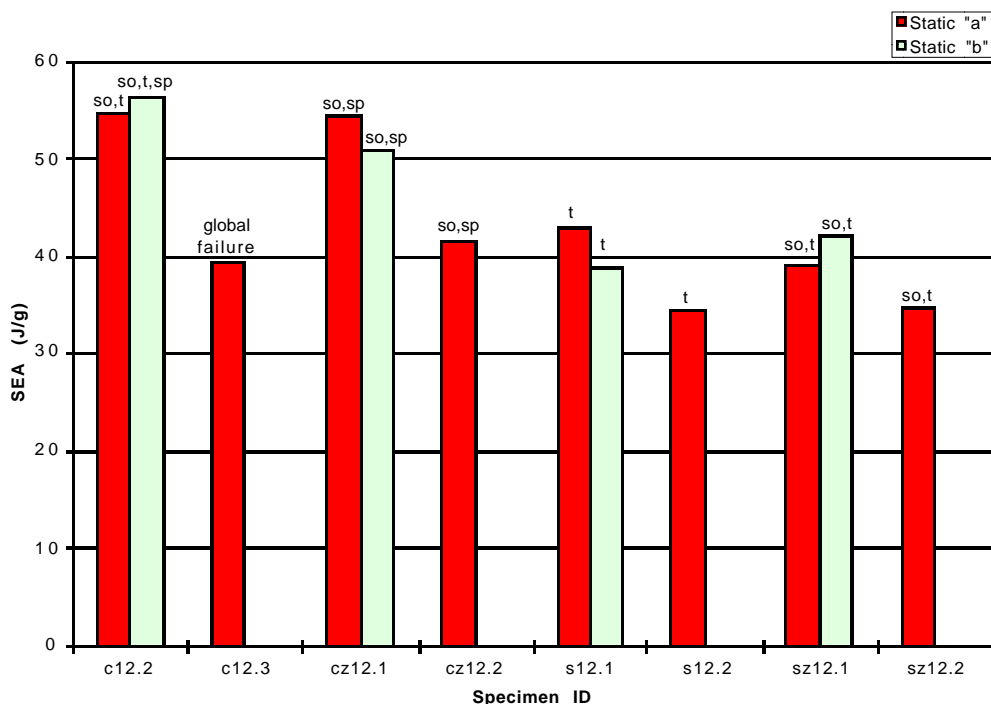
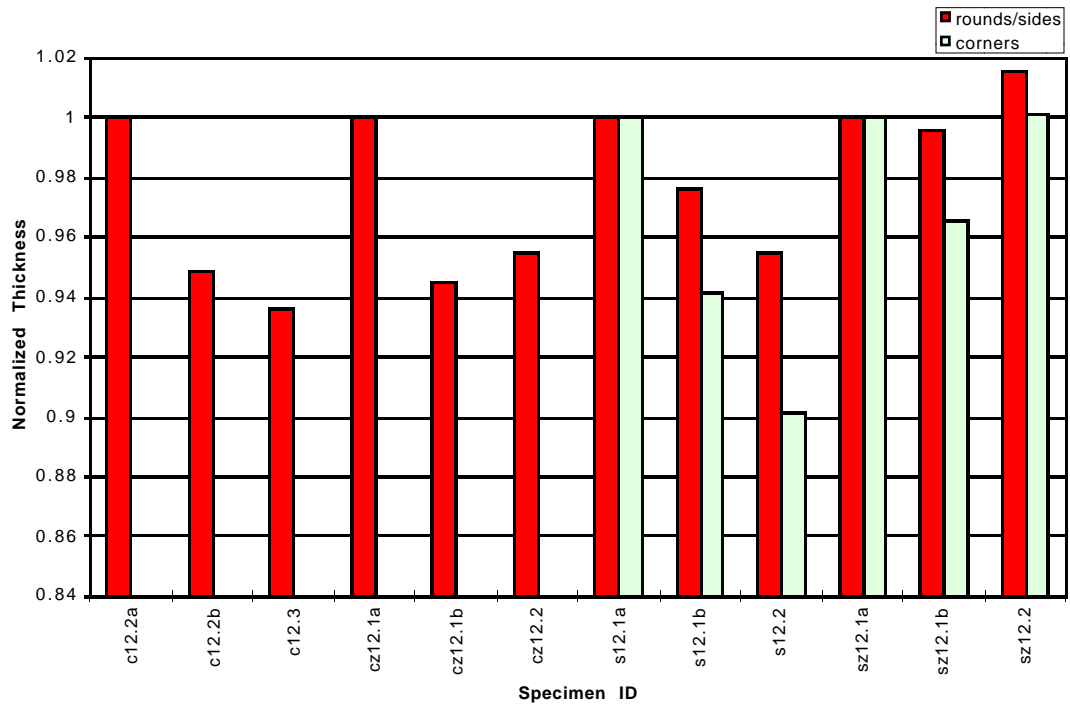


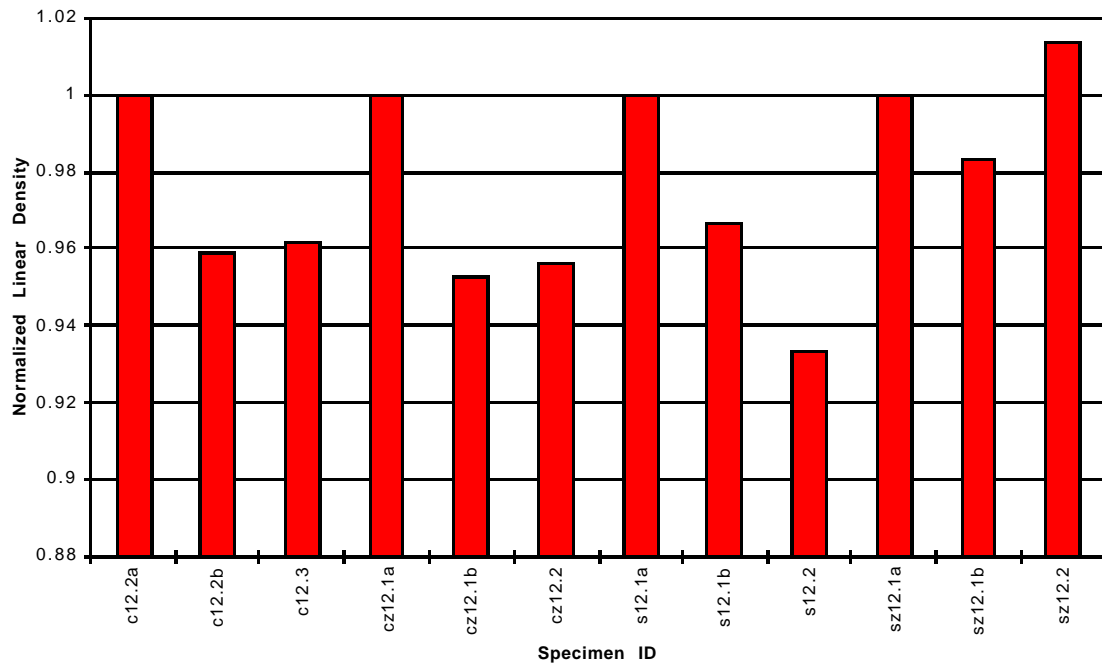
Figure 5-7: Specific energy absorption (SEA) and crush modes for the 12k static specimens

Also shown on Figure 5-7 are the crush modes present for each crushed specimen. The crush modes that occurred in each specimen are shown on top of the column representing that specimen: “t” for the tearing mode, “sp” for the splaying mode, and “so” for the socking mode. All of the crushing modes described earlier were observed with the 12k specimens. Specimen c12.2a failed by the socking and tearing modes with three fronds created. The most obvious failure mode that was seen in specimen c12.2b was the tearing mode with four fronds; however, the socking and splaying modes were also seen. Specimen c12.3 failed in a unique manner and this specimen exhibited the highest peak crush load of all the static specimens. This high peak crush load is seen in Figure 5-4, and it is also seen that the average crush load is not high. Initially, only failure on the beveled end took place, but then a 45° tear was seen that began at the bottom (on the non-beveled end of the specimen) and progressed upward. Soon this 45° tear was the major form of failure in the specimen and the high crush load could not be sustained, as is evidenced in Figure 5-4 by the significant drop in load observed towards the end of the crush length. The 12k circular specimens with the 0° layers all failed primarily by the splaying and socking modes. All of the 12k square specimens failed by tearing into four fronds with little splaying. The tear occurred at the radiused corners, and each flat stayed intact but exhibited matrix cracking. The 12k square specimens with the 0° layers also showed a moderate amount of socking.

To explore the difference in SEA between the end and middle specimens, Figure 5-8, which shows normalized values of thickness, linear density, and SEA, was created. The values were normalized by dividing the value from the particular specimen by the value from the corresponding “a” specimen. In this way each set of three replicate specimens were normalized by the first one in the set. Figure 5-8a shows the normalized thicknesses. For the square specimens the thickness of the sides is shown by the dark columns and the thickness in the corners is represented by the light columns. For all the 12k specimens, each static “b” specimen is seen to be thinner than the corresponding “a” specimen. The two middle specimens without zeros (c12.3 and s12.2) are even thinner than their corresponding “b” specimens. However, the two middle specimens with zeros (cz12.2 and sz12.2) are thicker than their corresponding “b” specimens; while middle specimen sz12.2 is also thicker than the corresponding “a” specimen. Except for c12.3 (c12.3 is heavier than c12.2b), as seen in Figure 5-8b, the linear densities follow the same trends as the thickness. In par-

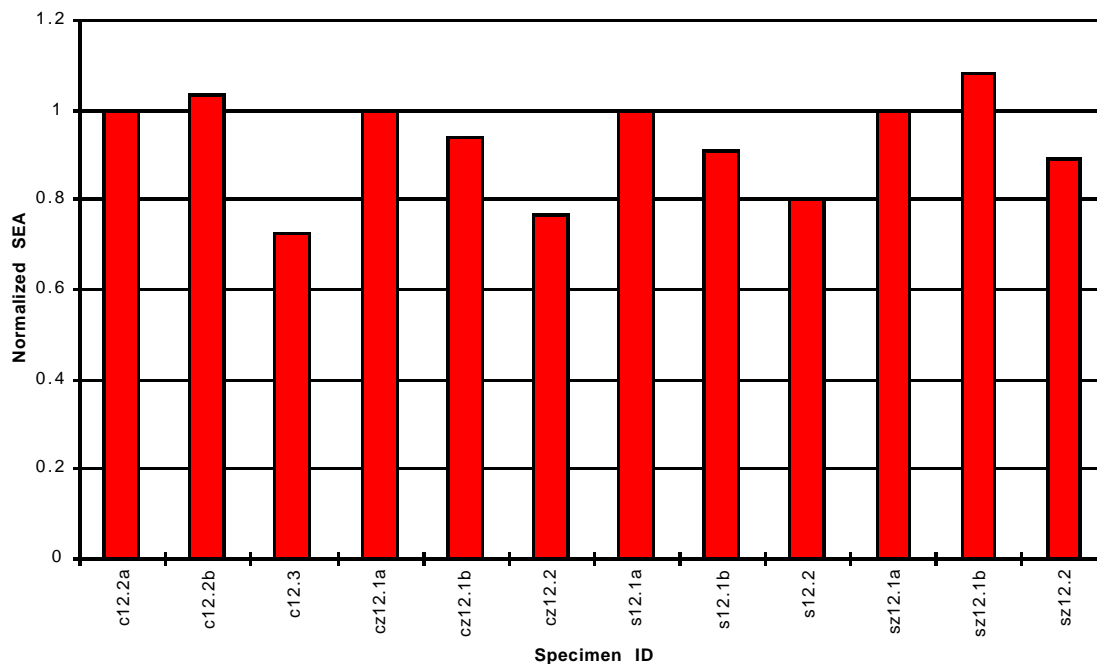


(a)



(b)

Figure 5-8: Normalized (a) thickness (b) linear density (c) SEA for the 12k static specimens



(c)

Figure 5-8: (Cont.) Normalized (a) thickness (b) linear density (c) SEA for the 12k static specimens

ticular, if a specimen in a set is thicker than another specimen in that set, then it also has a higher linear density. The normalized SEAs, seen in Figure 5-8c, show different trends. Two of the “b” specimens (c12.2b and sz12.1b) have higher SEAs than their corresponding “a” specimens, and two of the “b” specimens (cz12.1b and s12.1b) have lower SEAs than their corresponding “a” specimens. All of the middle specimens (c12.3, cz12.2, s12.2, sz12.2) have the lowest SEA in each set. The problem with the failure of specimen c12.3 has already been discussed, but there were no other drastic differences in crush modes noticed between the other specimens that would account for this trend with the middle specimens. It is believed, then, that there may have been variations, other than just the taper, along the lengths of the 840mm uncut tubes. Perhaps the ends were more well-consolidated or the fiber architecture in the ends was slightly different than the architecture in the middle due to the turnaround zone of the filament winder at each end of a tube.

The load ratios (see Equation 2-3) for the 12k static specimens, seen in Figure 5-9, are not very consistent. Except for specimen c12.3, which is an exception due to its failure mode, the square

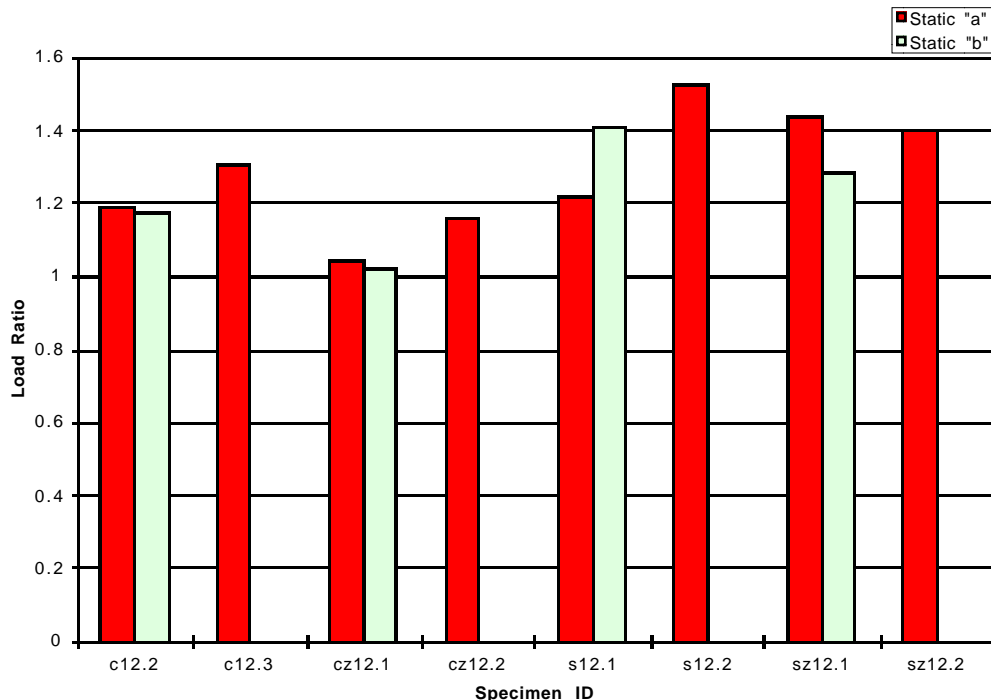


Figure 5-9: Load ratios for the 12k static specimens

specimens had higher load ratios than did any of the circular specimens. The load ratios for the circular specimens, except for specimen c12.3, were between 1 and 1.2, while the load ratios for the square specimens were between 1.2 and 1.6.

As discussed in Section 2.4, the filament winding process created a distinct fiber pattern. Tows being wound one way all crossed tows being wound the other way at regular intervals along the mandrel. Table 5-1 shows the axial position of each of these locations where the tows overlapped on each 12k static specimen. Examination of Table 5-1, in conjunction with Figure 5-4 and Figure 5-5, showed that the highest peak after the initial high peak in the crush load could be related to an area of tow overlap in ten of the twelve static specimens (cz12.1a has peaks at about 58 mm and near the overlap position at 97 mm). This cannot be said for c12.2a or c12.3 but recall that c12.3, failed globally. The trend was more pronounced for the specimens with zeros; that is, the peaks stand out more for the 12k specimens with zeros.

Table 5-1: Position, from beveled end, of tow overlaps for the 12k static specimens

Specimen	Position (mm)	
c12.2a	15	90
c12.2b	58	135
c12.3	50	128
cz12.1a	22	97
cz12.1b	64	142
cz12.2	46	124
s12.1a	80	
s12.1b	33	145
s12.2	89	
sz12.1a	92	
sz12.1b	43	
sz12.2	83	

5.3 50k specimens

Figure 5-10 shows the crush load vs. crush length traces for all the circular 50k static tests, while Figure 5-11 shows the traces for the square 50k static tests. Again, the solid lines show the actual measured crush loads at each crush length, while the broken lines show the average crush load. As was described earlier, specimens c50.2b, cz50.1b, s50.1b, and sz50.1b were shorter specimens so they were not crushed over the full 100 mm range, over which all other static specimens were tested. The plots in Figure 5-10 and Figure 5-11 approximate the ideal crush load vs. crush length trace, but they also show some characteristics that are not seen in the ideal trace shown in Figure 1-1. The main differences are that the 50k specimens often show dual initial peaks, and that these initial peaks are often not the highest of the test. Also, the load levels of some specimens exhibit fairly large valley-to-peak variations with the crush length.

It is seen from Figure 5-12, which shows the average crush loads for the 50k specimens, that all of

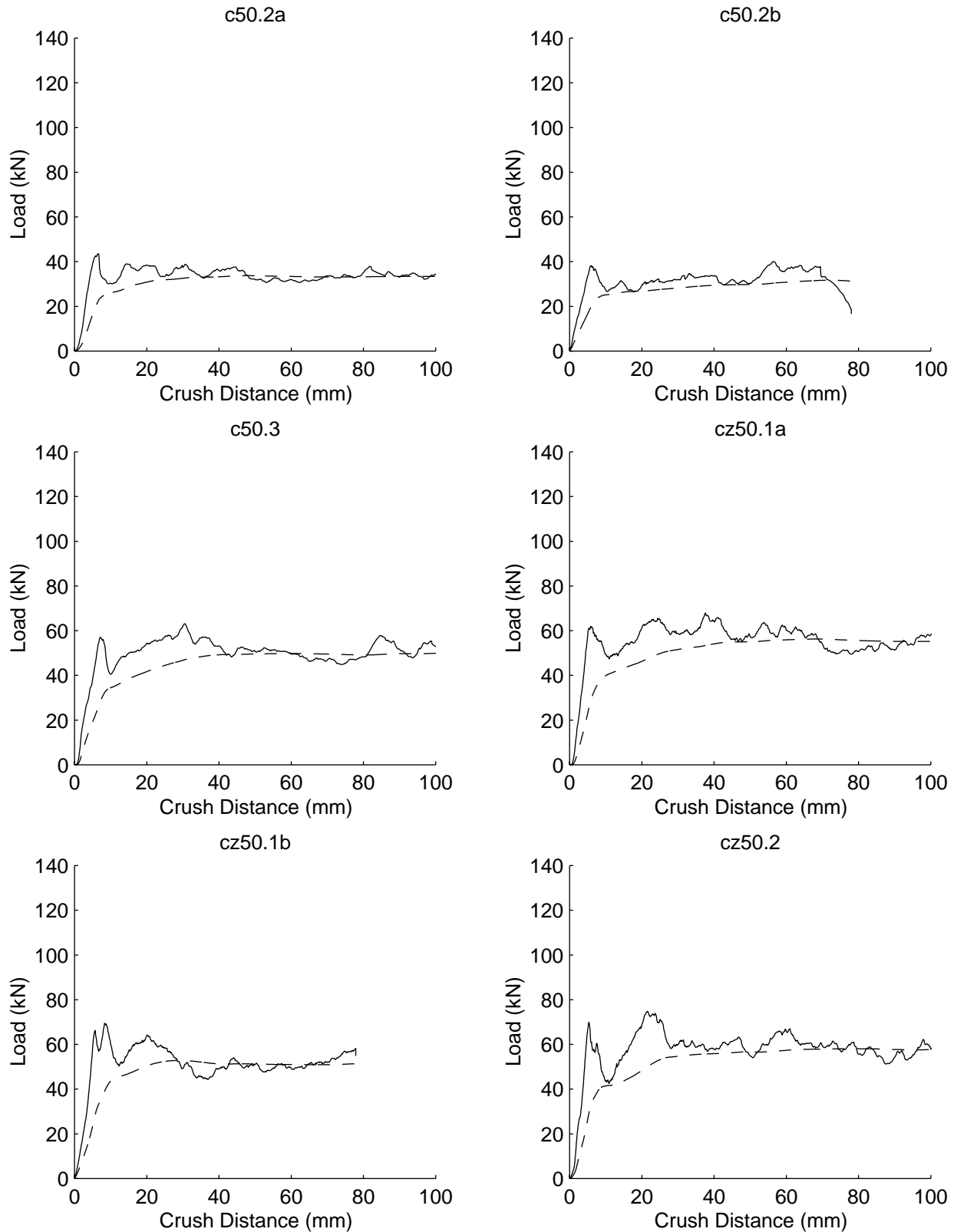


Figure 5-10: Crush load vs. crush length traces for the circular 50k static specimens

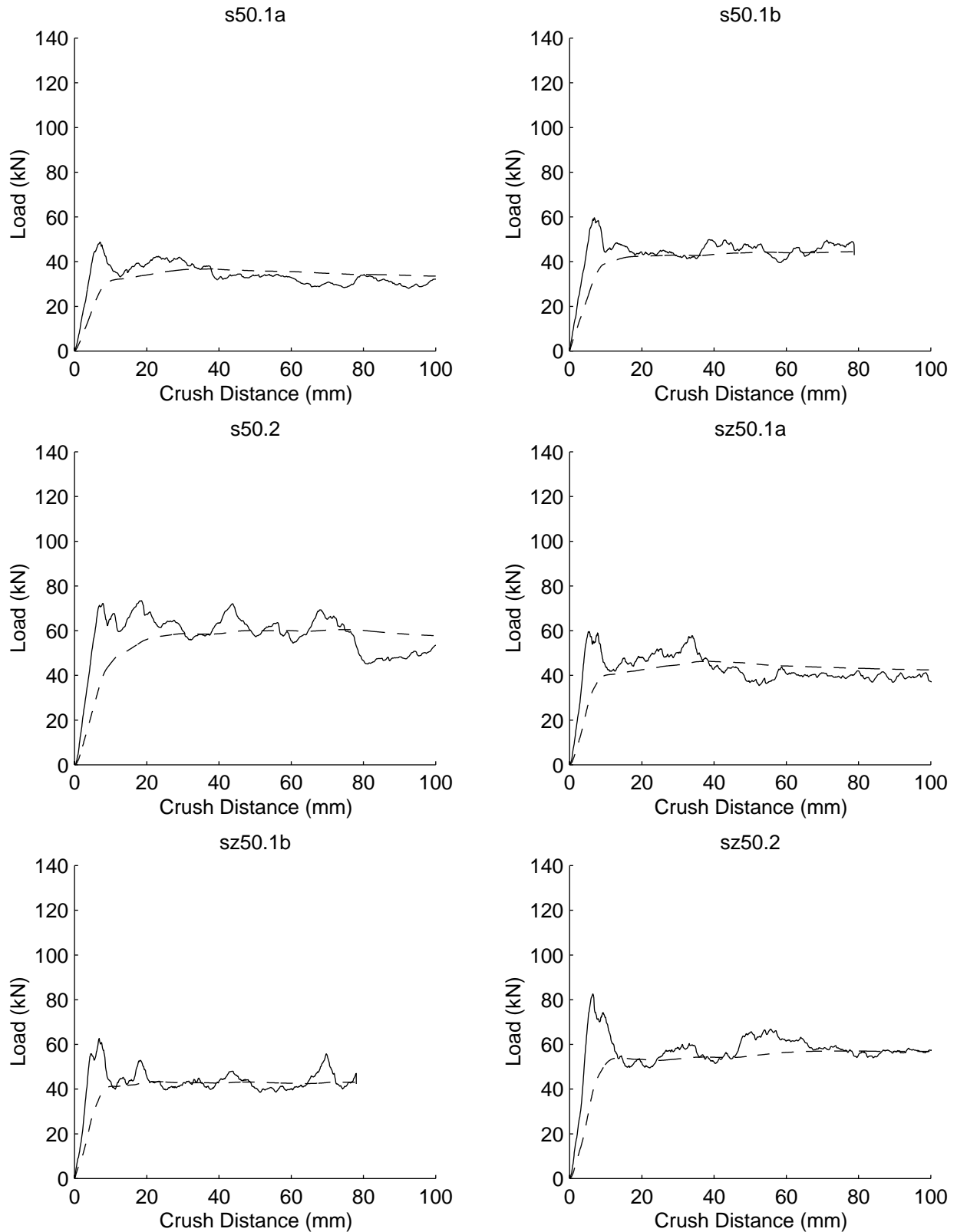


Figure 5-11: Crush load vs. crush length traces for the square 50k static specimens

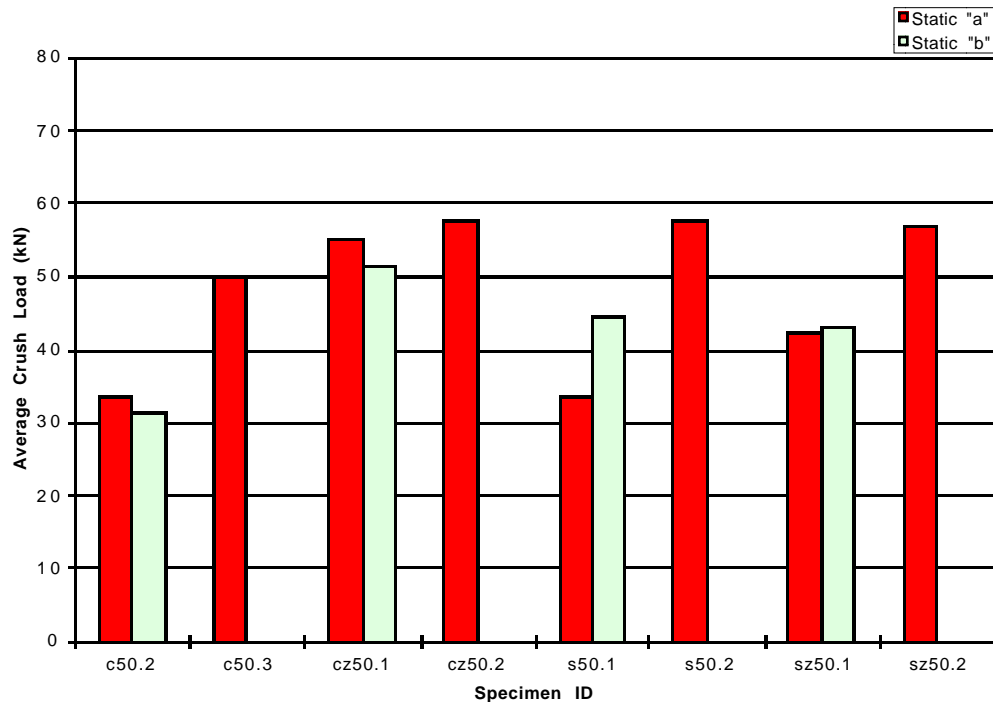


Figure 5-12: Average crush loads for 50k static specimens

the static specimens from the 840 mm tubes with the tighter tow spacing (c50.3, cz50.2, s50.2, and sz50.2) had higher average loads than their counterparts with the wider tow spacing. This is due, in part, to the fact that the specimens with the tighter-spaced tows had more material, but when the SEAs are examined in Figure 5-13, it is seen that the SEAs for all of the tighter-spaced tow specimens are also higher than the SEAs of the wider-spaced tow specimens. This higher SEA for the tighter-tow-spaced specimens indicates that these specimens may have had better consolidation. The circular specimens with the 0° layers had the highest SEAs of the 50k statically tested specimens. The presence of the 0° layers seemed to increase the average loads and the SEAs for the 50k circular specimens, but the 0° degree layers seemed to increase the average loads while having no effect on the SEAs of the 50k square specimens. The SEAs of the square specimens were, for the most part, lower than the SEAs of the circular specimens.

The crush modes are given for each specimen in Figure 5-13 above the column that represents that specimen. The 50k round specimens failed mostly by the splaying modes. All of these specimens,

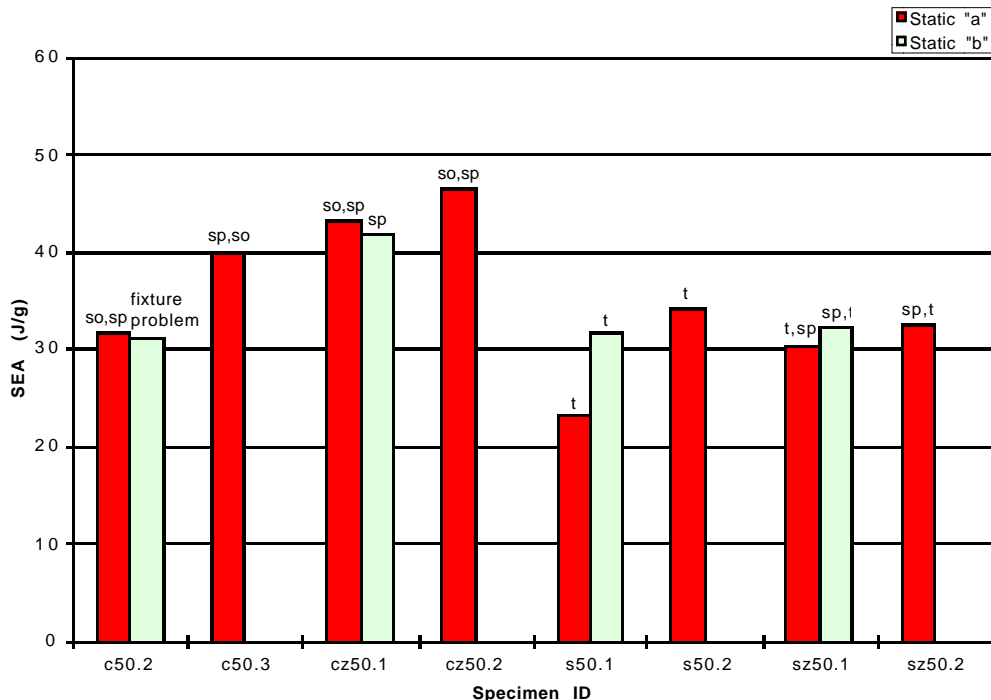


Figure 5-13: Specific energy absorption (SEA) and crush modes for the 50k static specimens

except for specimens c50.2b and cz50.1b, also showed socking. Specimen cz50.1b showed just the splaying into the individual tows, while specimen c50.2b failed in a different manner. Specimen c50.2b, along with specimens cz50.1b, s50.1b, and sz50.1b, was tested with the ball and socket joint between the cross-head and the crush initiator. In the case of specimen c50.2b, the ball and socket joint became misaligned as crushing began so the specimen was crushed on one side much more than on the other; the crush did not approach axisymmetry.

The square 50k specimens failed primarily by tearing into fronds and splaying. With the square 50k specimens there also seemed to be more tows that fractured after being separated than with the other specimens, either circular 50k specimens or any of the 12k statically tested specimens (i.e., the splayed tows were short due to fiber breakage). The square specimens with the 0° layers seemed to separate into individual tows much more than the other 50k square specimens to the extent that it was hard to distinguish the fronds (see Figure 5-14).

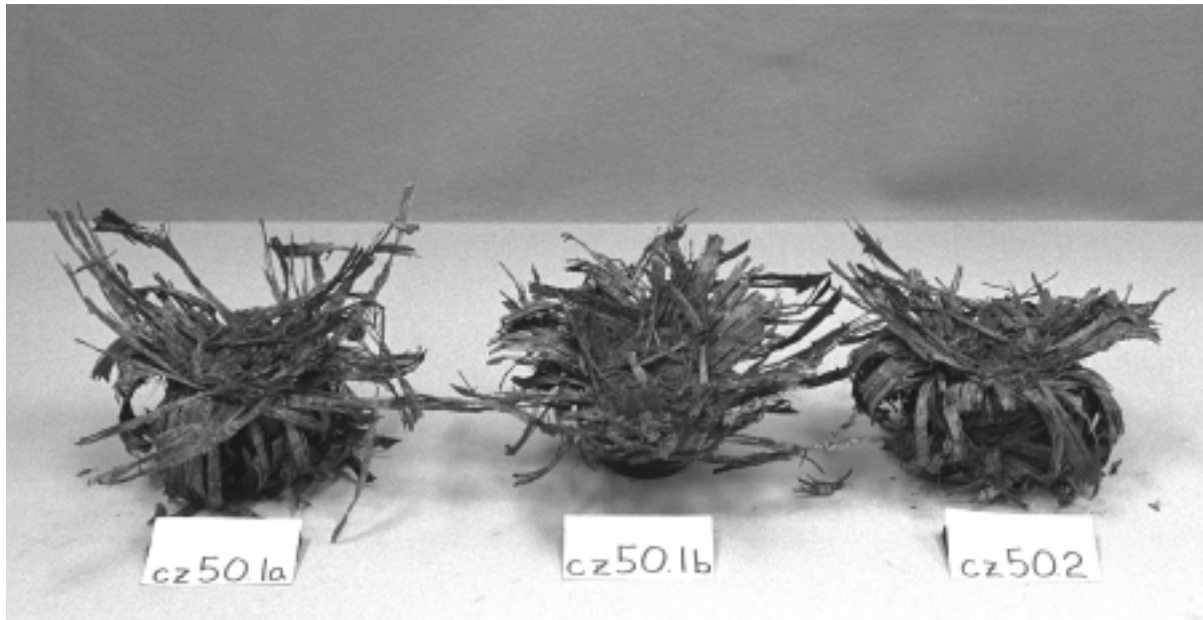


Figure 5-14: Crush shapes of square 50k tubes with 0° layers

The load ratios for the 50k static specimens are shown in Figure 5-15. The load ratios for the circular 50k specimens were generally lower than those for the square specimens. Three of the four 50k specimens with the tighter tow spacing (c50.3, cz50.2, and s50.2) had lower load ratios than at least one of the corresponding specimens with the wider tow spacing.

Table 5-2 gives the overlap locations for the 50k static specimens. The “b” specimens were tested before it was decided that these measurements might be important so they are not in the table. Using Table 5-2, Figure 5-10, and Figure 5-11, it is seen that there was little or no evidence of these tow overlaps having an effect on the crush load; however, this may be due to limited information. The specimens with zeros showed no evidence of being affected by the tow position; but, of the specimens without zeros, two peaks in crush load were near the position of the overlapped tows. The other 50k specimens without zeros had the overlapped tows near the bevel and the initial peaks, where any overlap effect was masked by the crush initiation.

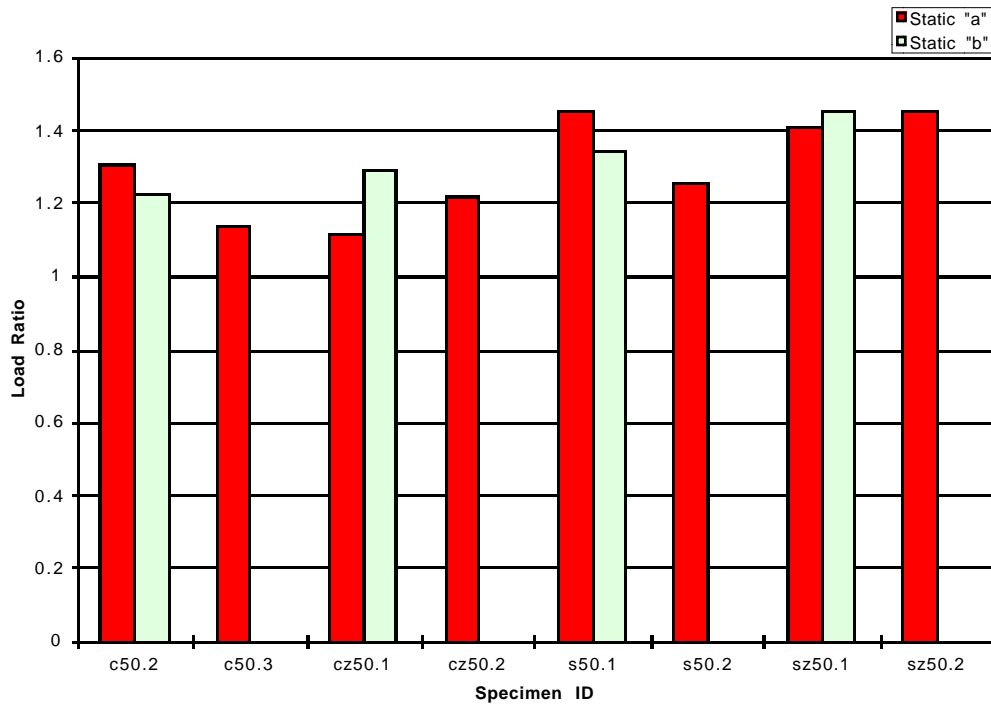


Figure 5-15: Load ratios for the 50k static specimens

Table 5-2: Position, from beveled end, of tow overlaps for the 50k static specimens

Specimen	Position (mm)	
c50.2a	33	107
c50.3	13	89
cz50.1a	44	120
cz50.2	28	105
s50.1a	27	130
s50.2	46	
sz50.1a	100	
sz50.2	92	

5.4 Comparison of 12k and 50k specimens

The valley-to-peak variations seen in the crush load vs. crush distance traces varied. Overall, the 50k specimens showed smaller valley-to-peak variations in the crushing load than did the 12k specimens. The circular 12k specimens seemed to have the largest variations. As was discussed in connection with the ideal trace of Figure 1-1, it is desirable to have little valley-to-peak variation in the steady crush region [4].

When looking at figures of the average loads and SEA (Figure 5-6, Figure 5-7, Figure 5-12, and Figure 5-13) for the static tests, the 12k and the 50k specimens show an opposite trend. For the 12k specimens, all the end (“a” and “b”) specimens for each 840 mm tube had higher values of average load and SEA than did the single middle specimen from the other 840 mm tube. The reverse was true for the 50k specimens; the single 50k specimen always had higher values of average load and SEA than did either of the corresponding end specimens. Because both of the 840 mm 12k tubes within a family were fabricated in the same manner, it is postulated that the difference in the average load and SEA is due to the position along the tube from which the specimen was cut. This same comparison cannot be made with the 50k specimens because the tubes from which the middle specimens came had the decreased tow spacing.

The 12k end specimens had much larger values of SEA than the matching 50k end specimens (between 19% and 30% larger, calculated as $[(SEA_{12k} - SEA_{50k})/SEA_{12k}] \times 100\%$, where the values of SEA are averages for the tubes with two end specimens). The 12k single middle specimens and the matching 50k single middle specimens, however, had fairly close SEAs (12k SEAs between 6% larger and 12% smaller), with the SEA for only one of the 50k single middle specimens being lower than its 12k counterpart (specimen sz50.2 compared to specimen sz12.2).

For both the 12k and 50k static specimens, the square specimens had lower SEAs. The square specimens also failed primarily by tearing in the corners. It can then be said that the SEA was lower for the square specimens because either the tearing crushing mode was not as effective at

absorbing energy as the other modes, or because the square specimens were somehow inferior in quality to the circular specimens. The tearing in the square specimens occurred mostly in the corners, so not as much percentage of material is used in energy absorption. Also, the square specimens showed large voids in the flats which may indicate poor consolidation, so the failure that did occur in the flats may not have absorbed much energy.

If, as mentioned by Karbhari, et al. [5], a load ratio of less than 1.25 is desirable, then the performance of many of these specimens might not be desirable, at least with the bevel crush initiator that was used. The square specimens of both the 12k and 50k material had load ratios higher than 1.25 so, if one were to put these specimen designs to use, perhaps a method would have to be devised to lower the load ratio for the square specimens. Most of the circular specimens had load ratios less than 1.25. Of course, the validity of these quantities must be questioned because of the large valley-to-peak variations and the non-distinct initial peaks.

The 12k specimens showed evidence of having the areas of overlapped tows increase the crush load. The 50k specimens did not show evidence of having the crush load affected by the position of the overlapped tows.

Although some of the results may have been clouded by questions about differences between the end and middle specimens, and the change in tow spacing to improve the quality of the 50k specimen, in the static tests, no obvious disadvantage to using 50k tows for energy absorption during static crush was seen.

Chapter 6 Dynamic energy absorption characteristics

The dynamic tests were performed at the General Motors Corporate Research and Development Center. The static tests were used to determine suitable drop heights, and therefore the impact speeds, for the dynamic tests. Ideally one drop height would be used for all of the dynamic tests, but because the average crush load was quite low for some of the static specimens, no single drop height could be chosen where the high crush load specimens would crush a significant distance, and the low crush load specimens would absorb all of the energy of the drop head. If the specimen did not absorb all of the energy, there was a risk of damage to the test fixture. A drop height was chosen that would meet that criteria for most of the specimens. Twenty-one of the twenty-four specimens were tested with the same drop height and the other three specimens were tested with a lower drop height. The twenty-one specimens were dropped from 5.72 m, which gave an impact speed of about 7.49 m/s. The other three specimens, c50.2, s50.1, and sz50.1, were dropped from 2.54 m, 4.45 m, and 5.08 m giving impact speeds of 4.99 m/s, 6.60 m/s, and 7.06 m/s, respectively.

During the dynamic tests, the crush load and acceleration were sampled at a constant rate. As was discussed in Chapter 2, the crush loads vs. time were integrated to obtain the crush distance. The acceleration was also integrated as a check. The crush load and acceleration plotted vs. time, the integrations of these, and the crush load plotted vs. crush distance are shown in the Appendix.

Using Equation 2-1, the energy absorbed during crush was calculated. As a check, the potential energy of the drop mass was compared to the calculated energy during crush. There was good consistency, with the potential energy always between 9% and 14% higher. This is expected because of energy losses in the guide cables and elsewhere. The results are seen in Figure 6-1. The

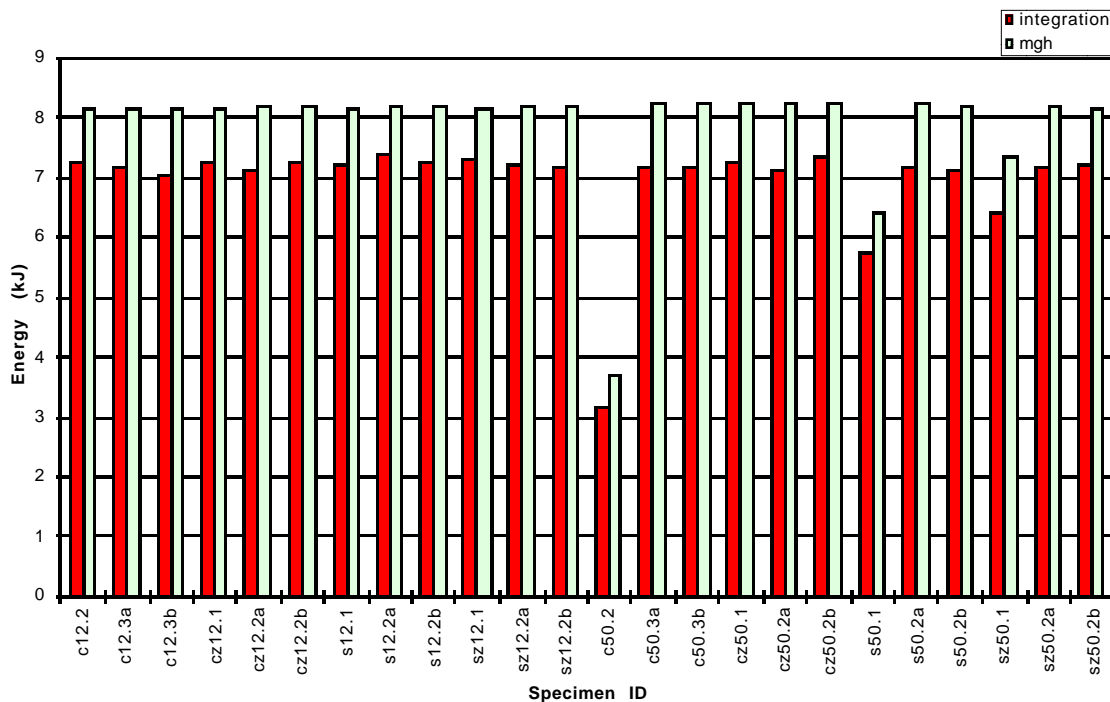


Figure 6-1: Energy calculated from crush load vs. crush length traces and from potential energy

dark columns represent the energy calculated from the crush load vs. crush length traces and the light columns represent the calculated potential energy of the crush mass.

In the dynamic tests, the three crushing modes were again seen, but with some slight differences. Occasionally the specimen wall was crushed in such a way that, in a certain section of the wall, all of the material was pushed inside the tube. Also, for some of the specimens which showed the tearing crush mode, the fronds would break off in places, leaving the fronds quite short.

6.1 12k specimens

All of the 12k specimens were dropped from 5.72m, which gave an impact speed of about 7.49 m/s. The crush load vs. crush distance traces for the circular 12k dynamic specimens and square 12k dynamic specimens are seen in Figure 6-2 and Figure 6-3, respectively. Note that the scale of the

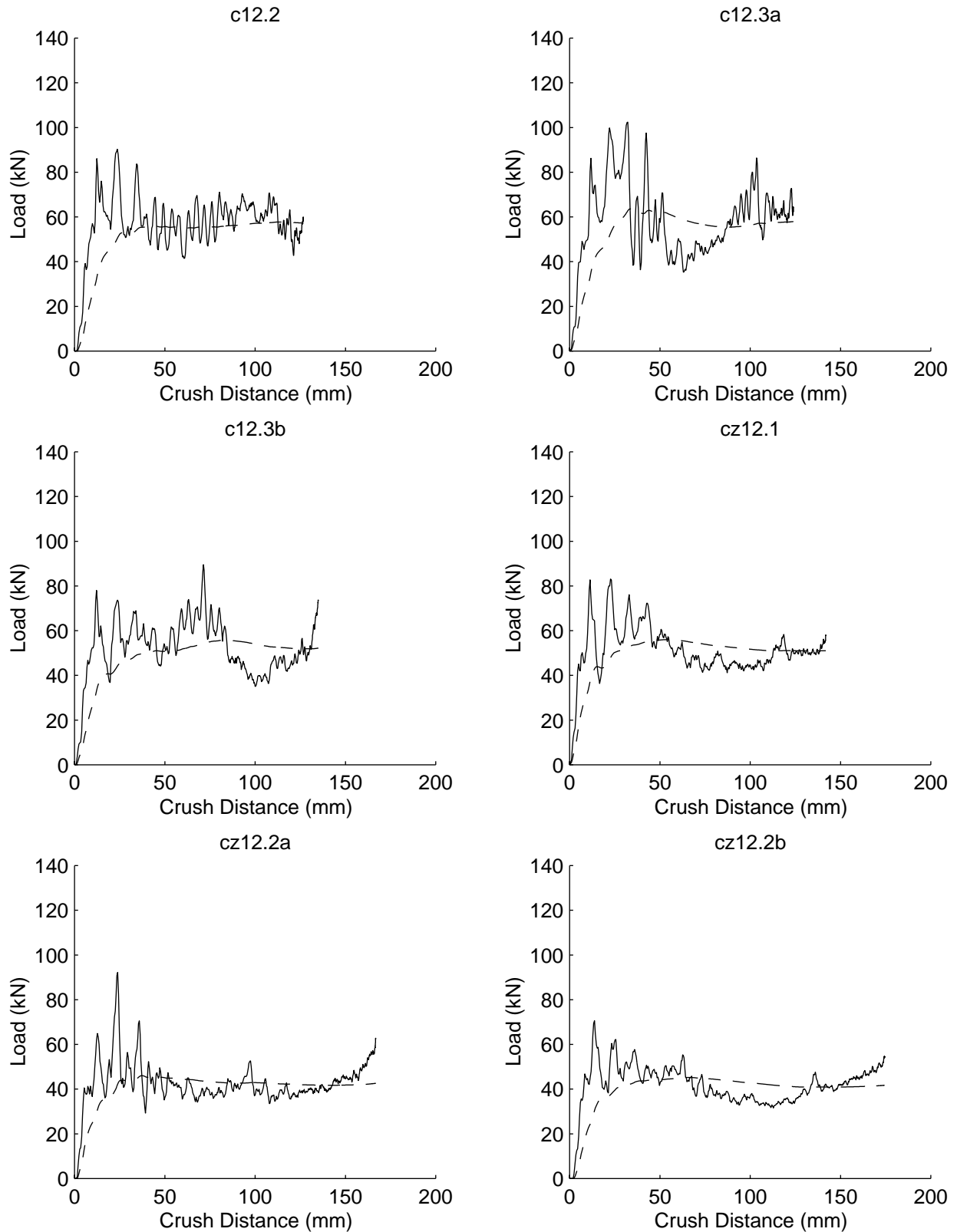


Figure 6-2: Crush load vs. crush length for the circular 12k dynamic tests

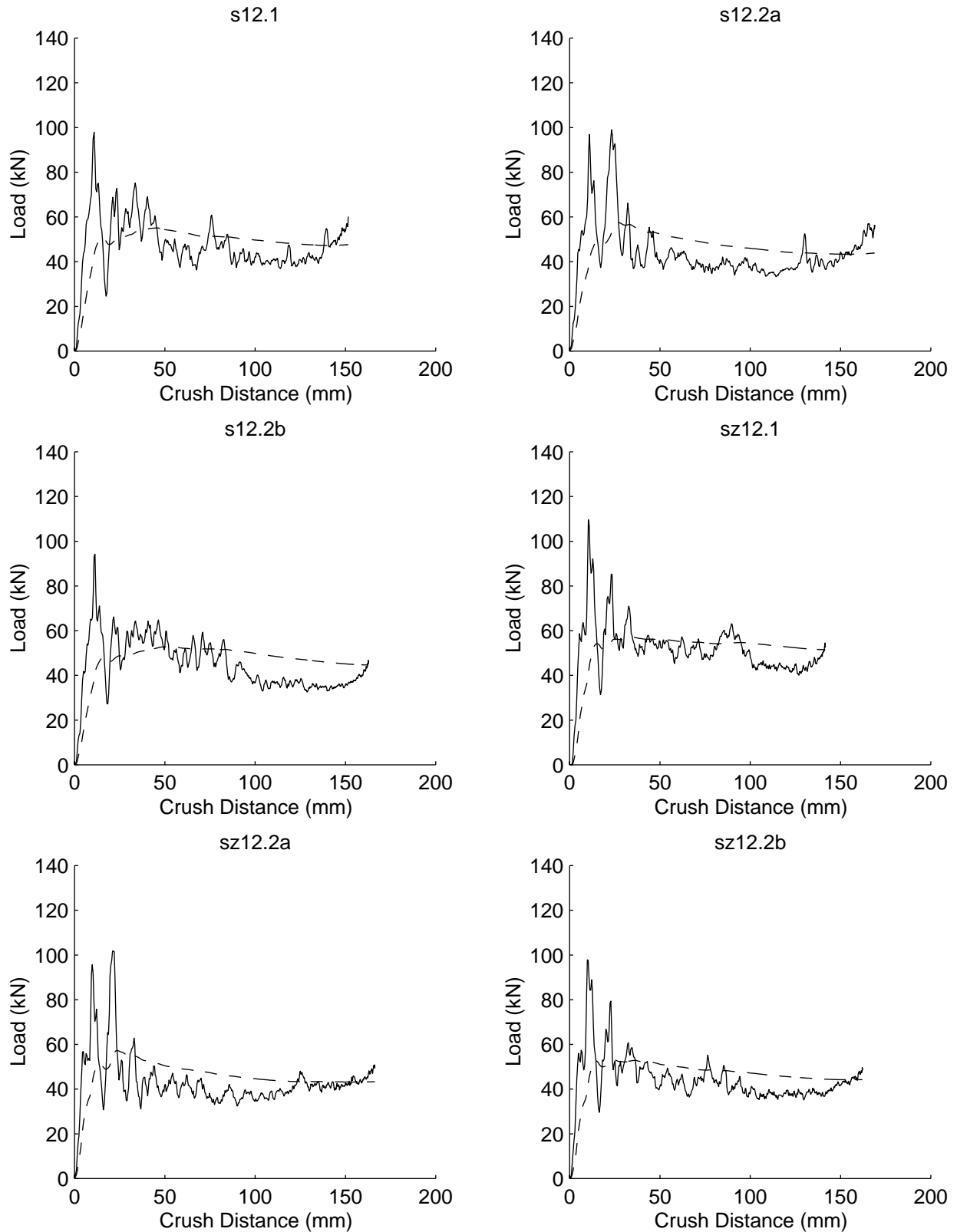


Figure 6-3: Crush load vs. crush length for the square 12k dynamic tests

crush distance in the dynamic crush load vs. crush distance traces is from 0 to 200 mm, while for the static traces the scale was from 0 to 100 mm. This scale difference gives the impression that the dynamic tests had higher frequency oscillations in crush load. As it was for the static tests, the solid lines represent the crush load at each distance, while the broken lines show the running average crush load, averaged over crush distance using Equation 2-2. Most of the 12k dynamic specimens exhibited crush load vs. crush distance traces similar to the ideal trace in Figure 1-1. From Figure 6-2, the major differences between the traces for the circular 12k specimens and the ideal trace are the large valley-to-peak variations in the steady crush regions and some high peaks outside the crush initiation region. For the square 12k specimens, the major difference from the ideal trace is the large initial peaks seen for all of the square 12k specimens. Perhaps it is difficult to begin the corner tearing (the tearing crush mode was seen in all six square 12k specimens), but does not take as much force to continue tearing.

To see how effectively each specimen absorbed energy, the average crush loads sustained over the crush distances were examined. Figure 6-4 shows the average crush loads for the dynamic 12k specimens. As can be observed, the circular 12k specimens had the highest average crush loads of the dynamic 12k specimens. The circular 12k specimens without 0° tows had higher average crush loads than any of the square 12k specimens. However, the circular 12k specimens with 0° tows had about the same average crush load as the square 12k specimens with 0° tows. Three of the middle specimens (cz12.1, s12.1, and sz12.1) had higher average crush loads than either corresponding end specimen. The other middle specimen (c12.2) had a higher average crush load than only one of the corresponding end specimens (c12.3b).

Figure 6-5 shows the SEAs from the 12k dynamic tests. From this figure it is seen that, in general, the circular 12k specimens had higher SEAs than did the square 12k specimens. The circular specimens from three of the tubes, c12.2, c12.3, and cz12.1 had higher SEAs than any of the square 12k specimens. The circular specimens from the other tube, cz12.2, had higher SEAs than all of the square 12k specimens except sz12.1. The SEAs of all the single middle specimens were higher than the SEAs of either of the two corresponding end specimens. For the 12k specimens without 0° tows, the middle specimens had only slightly higher SEAs than the SEAs of the corre-

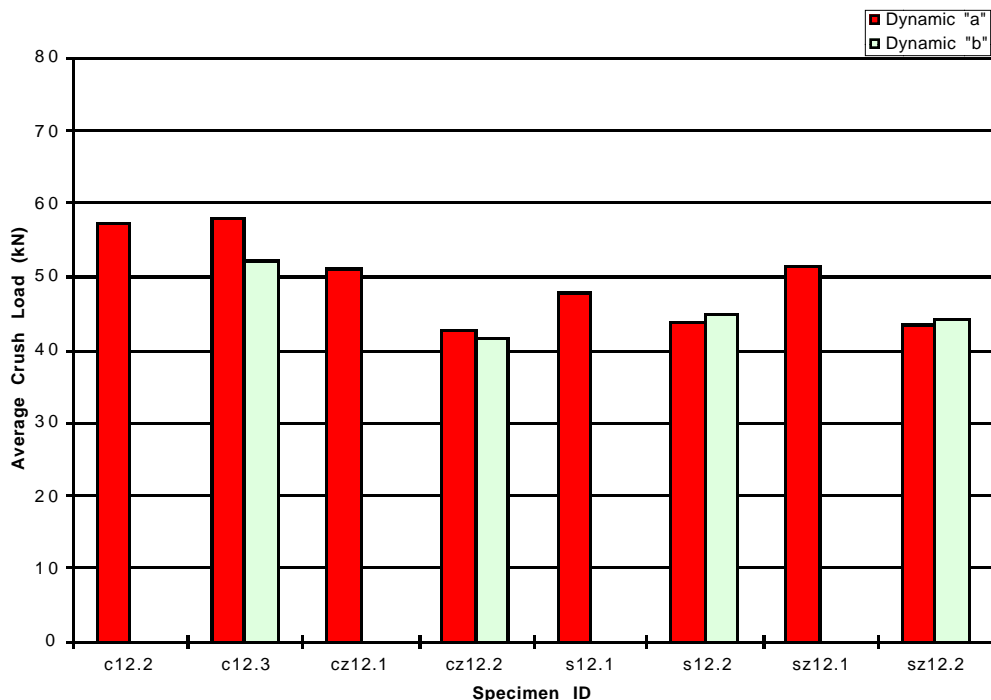


Figure 6-4: Average crush loads of the 12k dynamic specimens

spending end specimens (middle circular 4% higher, middle square 7% higher, calculated as $[(middle - end)/end] \times 100\%$, where the end specimens were averaged). The middle specimens, both circular and square, with 0° tows had significantly higher SEAs than the SEAs of the corresponding end specimens (middle square 21% higher, middle square 18% higher). Recall that the static tests showed the opposite trend; the middle 12k specimens had significantly lower SEAs than the end specimens.

The crush modes are also shown on Figure 6-5: “t” for the tearing mode, “sp” for the splaying mode, and “so” for the socking mode. The circular 12k specimens without 0° tows showed all three crush modes. The tearing crush mode seemed to occur mostly toward the end of the crush, with about 5 short fronds being formed on the inside portion of the part of the wall that was pushed outward. The addition of the 0° tows to the circular 12k specimens increased the presence of the socking mode. Heavy socking with splaying was seen for the circular 12k specimens with 0° tows. Tearing, with the formation of four fronds, was seen for all of the square 12k specimens.

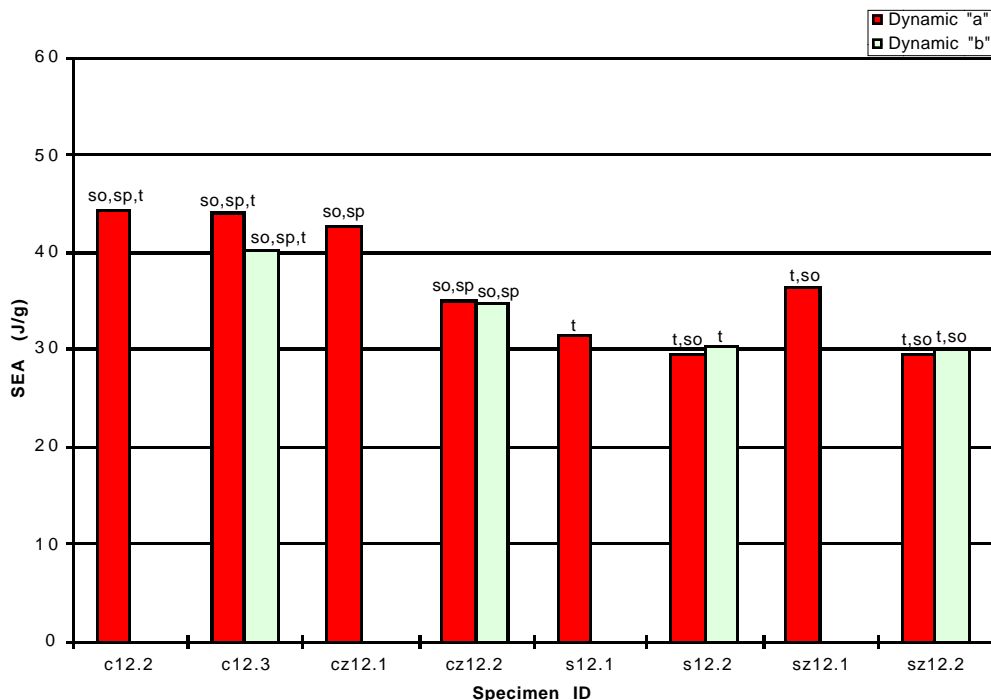


Figure 6-5: Specific energy absorption (SEA) and crush modes of the 12k dynamic specimens

The presence of the 0° tows also increased the presence of the socking mode in the square 12k specimens; the square 12k specimens with 0° tows showed prominent socking.

Figure 6-6 shows the load ratios obtained from the 12k dynamic tests. The load ratios of the circular 12k specimens without 0° tows, at 1.5, were the lowest of all the 12k dynamic specimens. The 12k circular specimens with 0° tows had slightly higher load ratios. The square 12k dynamic specimens all had load ratios over 2.

The effects of fiber pattern were examined for the dynamic specimens. Table 6-1 shows the tow-overlap positions for the 12k dynamic specimens. Using Table 6-1 in conjunction with Figure 6-2 and Figure 6-3, the effect of the overlap areas on the crush load can be determined. It is seen that there does not appear to have been a large effect of the tow overlap on the crush load. In five of the six circular dynamic specimens (c12.2 excepted) the tow overlap positions could be related to a peak past the initial peaks. In c12.3b, the peak associated with the overlap at 72 mm was the high-

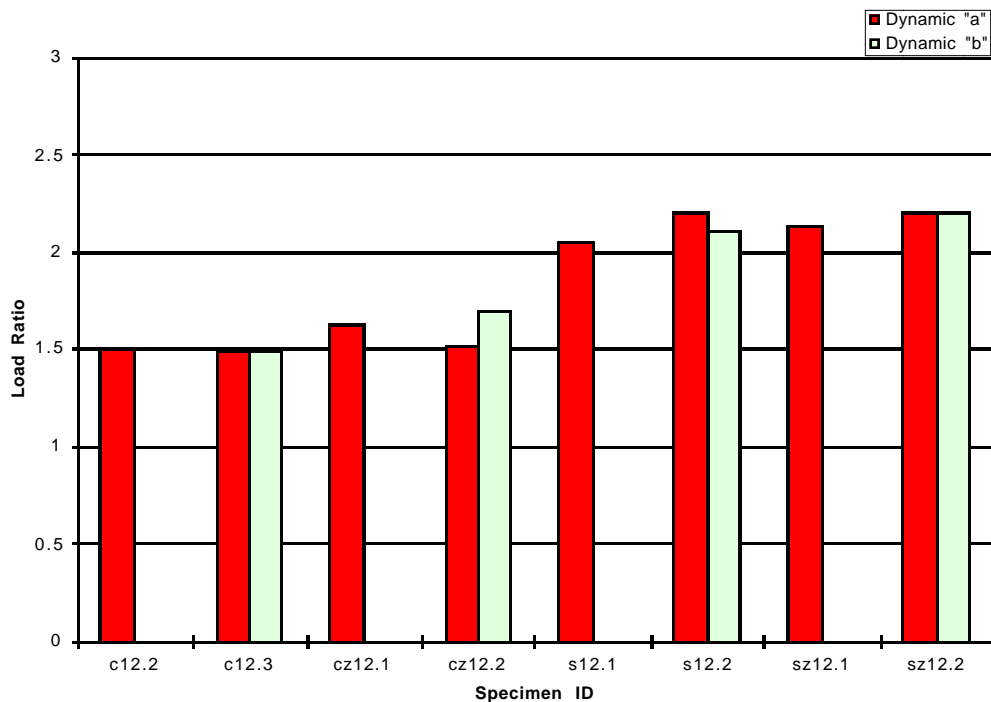


Figure 6-6: Load ratios of the 12k dynamic specimens

Table 6-1: Position, from beveled end, of tow overlaps for the 12k dynamic specimens

Specimen	Position (mm)			
c12.2	35	112	191	267
c12.3a	28	105	183	258
c12.3b	72	149	227	306
cz12.1	44	122	199	279
cz12.2a	22	101	179	254
cz12.2b	63	140	218	296
s12.1	78	190	302	
s12.2a	135	244		
s12.2b	82	193		
sz12.1	87	200		
sz12.2a	132	241		
sz12.2b	78	190		

est crush load for the test. Specimen c12.3a also had a high peak associated with the overlap position at 105 mm. The circular 12k specimens with 0° tows, cz12.1, cz12.2a, and cz12.2b, had very small peaks associated with the overlap positions at 122 mm, 101 mm, and 140 mm, respectively. However, the small peaks in cz12.1 and cz12.2a did not line up perfectly with the overlap positions. Five of the six square 12k specimens (s12.2b excepted) had peaks that could be associated with the overlap positions. However, the peaks near the overlap position on these specimens were quite small and did not line up perfectly with the tow overlap positions. Specimen s12.2b had larger valley-to-peak variations than the other square 12k specimens, and they masked any effects of the tow overlap.

6.2 50k specimens

As mentioned above, the 50k specimens, except c50.2, s50.1, and sz50.1, were dropped from 5.72 m, the same height from which all the 12k specimens were dropped. Specimens c50.2, s50.1, and sz50.1 were dropped from 2.54 m, 4.45 m, and 5.08 m, respectively. Static specimens cut from the same tubes as these specimens had low average crush loads, so the dynamic specimens from these tubes were dropped from these lower heights so that the specimen would absorb all of the energy of the drop head. The crush load vs. crush distance traces for the circular 50k specimens are shown in Figure 6-7 and the crush load vs. crush distance traces for the square 50k specimens are shown in Figure 6-8. The solid line shows the crush load at the crush distance, while the broken line is the average crush load. Most of 50k dynamic tests produced quite high initial peak loads, often double the average load. These large initial peaks were the main difference between the 50k traces and the ideal crush load vs. crush distance trace. The circular 50k specimens without 0° tows did not show the large initial peaks, but all the other dynamic 50k specimens did show the large initial peak.

Figure 6-9 shows the average crush loads for the 50k dynamic tests. Three of the four middle specimens, c50.2, s50.1, and sz50.1, had lower average loads than the corresponding end specimens. The middle specimen cz50.1 had a higher average load than either of the corresponding end specimens, cz50.2a or cz50.2b. Since the end 50k dynamic specimens had the tighter tow spacing,

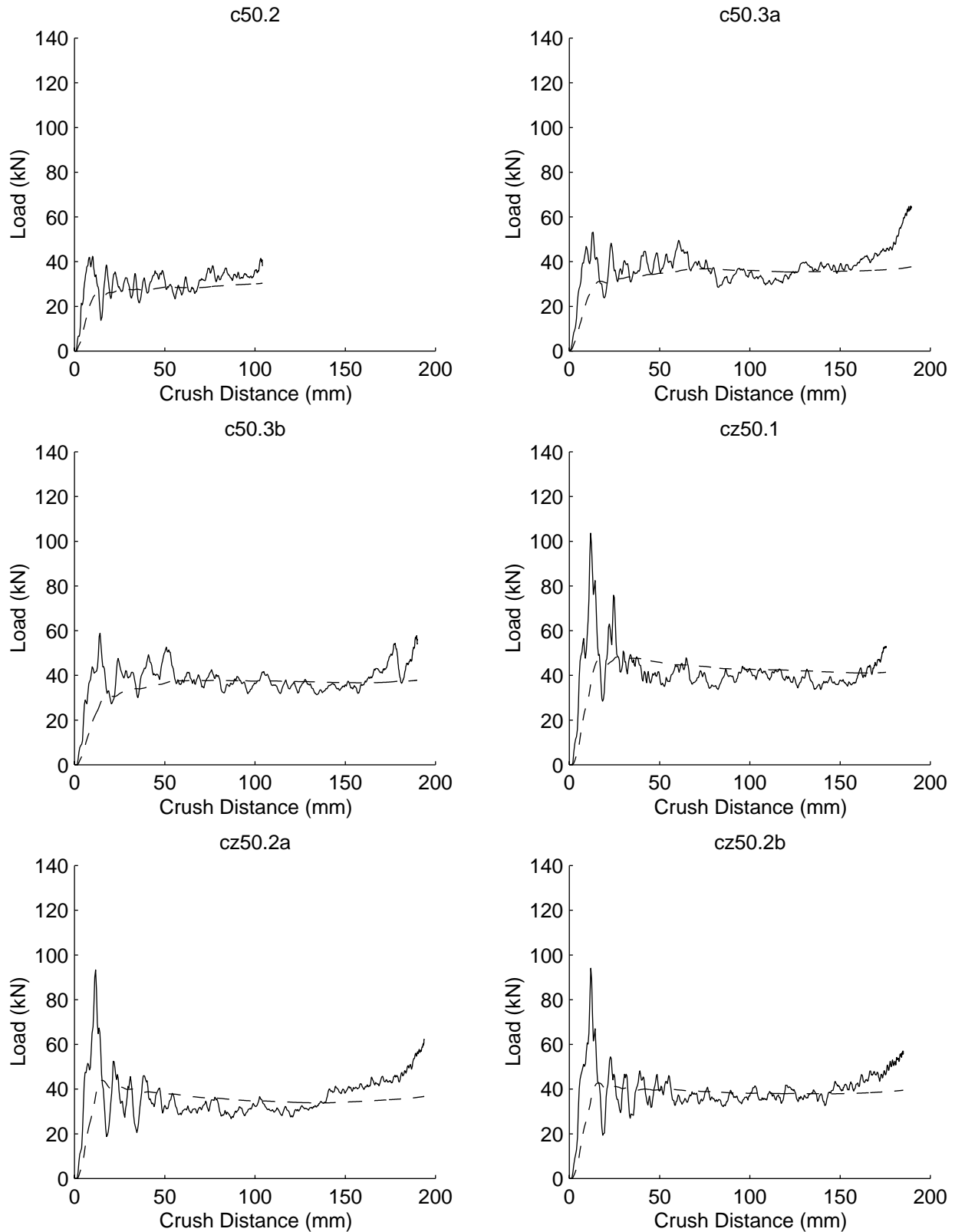


Figure 6-7: Crush load vs. crush length traces for the circular 50k dynamic specimens

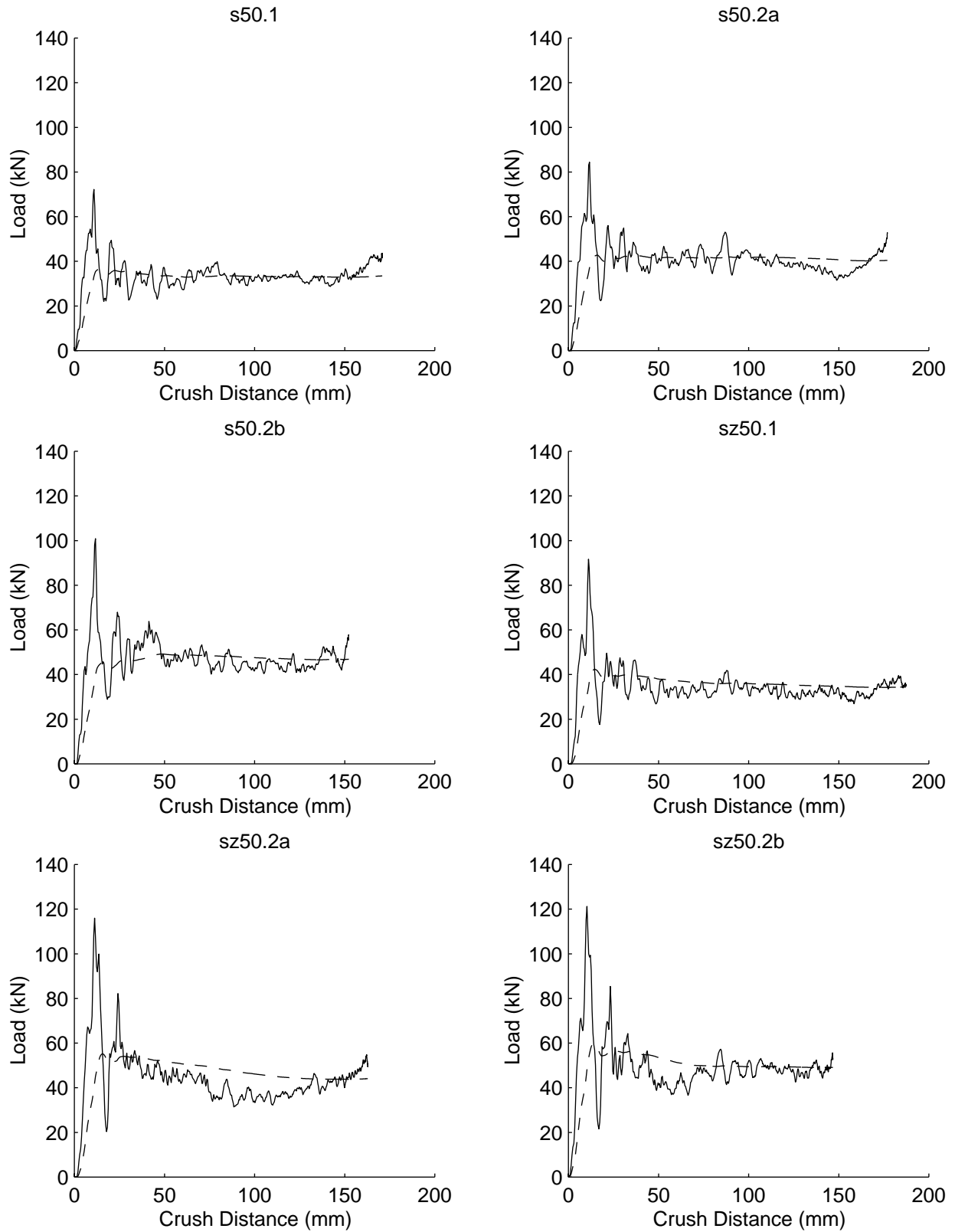


Figure 6-8: Crush load vs. crush length traces for the square 50k dynamic specimens

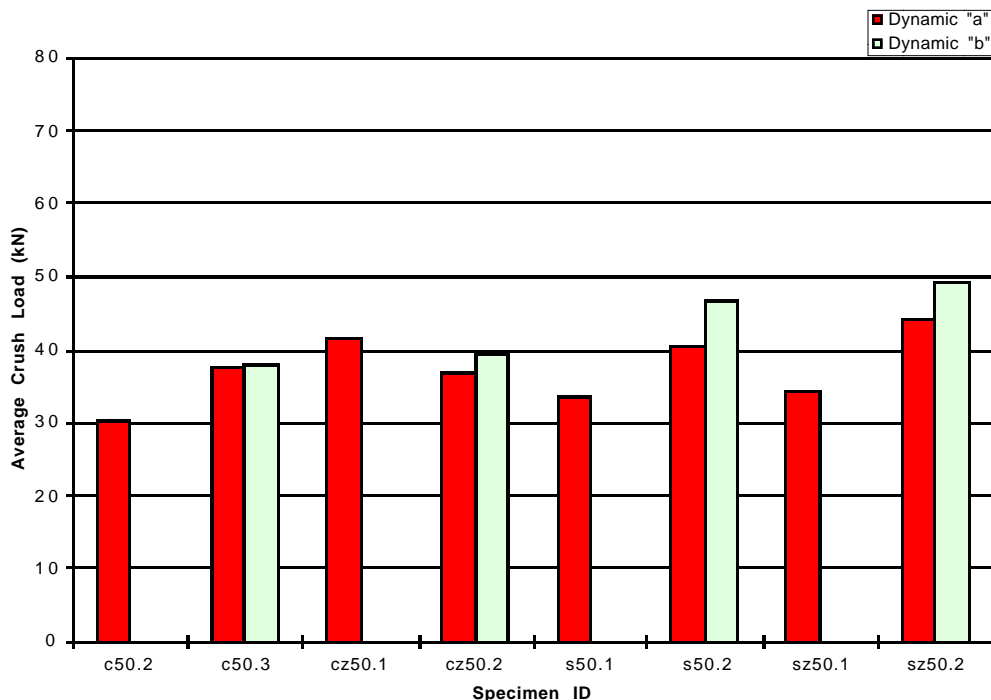


Figure 6-9: Average crush loads of 50k dynamic specimens

it was expected that they would produce higher average loads. Also recall, from Figure 4-6 and Figure 4-7, that tube cz50.1 had about the same linear density and volume per unit length as tube cz50.2 which had the tighter tow spacing. The other 50k tubes with the tighter tow spacing were heavier and more voluminous than the corresponding tubes with the looser tow spacing.

Because the tow spacing affected the linear density of many of the sets of specimens with the same set of parameters, it is important to examine the specific energy absorption. The SEAs for the 50k dynamic specimens are shown in Figure 6-10. Examining Figure 6-10, it is seen that the SEAs for specimens with like sets of parameters are closer together than the average loads for those specimens. The SEAs of the circular 50k specimens without 0° tows are almost identical, although the SEA of c50.2 is higher than either c50.3a or c50.3b. The SEA of specimen cz50.1 is higher but still quite close to the SEAs of cz50.2a and cz50.2b. The circular 50k specimens all had higher SEAs than any of the square 50k specimens. The middle square specimens had about the same SEAs as the corresponding “a” specimens but lower than the “b” specimens.

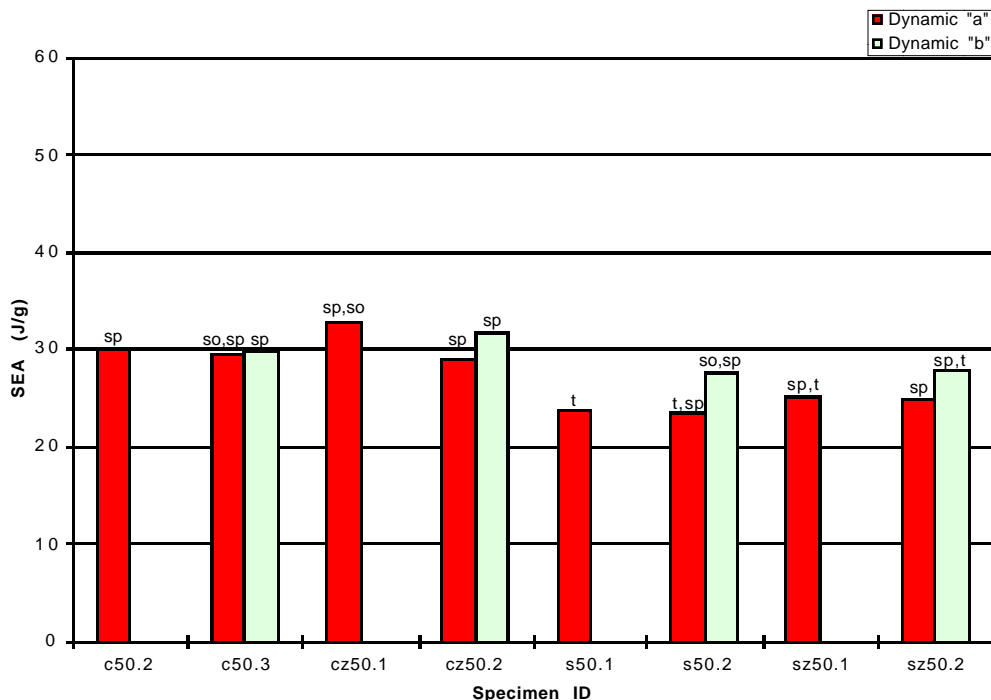


Figure 6-10: Specific energy absorption (SEA) and crush modes of the 50k dynamic specimens

The crush modes for each specimen are also given in Figure 6-10. As in Figure 6-5, the crush mode is shown above the bar representing each specimen. The circular 50k dynamic specimens failed primarily by splaying. Specimen c50.3a and cz50.1 also showed the socking mode. Specimen c50.3b had a portion of the tube wall pushed almost entirely inside. The square 50k specimens without 0° tows failed by all three modes. Specimen s50.1 failed by tearing, with most of one flat crushed almost entirely inside. The fronds in s50.1 were short because they broke off during crushing. Specimen s50.2a failed by tearing and splaying, and s50.2b failed by socking with some splaying. The square 50k specimens with 0° tows all failed primarily by splaying. Specimens sz50.1 and sz50.2b also failed by tearing into fronds. The fronds on sz50.1 were short because the tows broke off during crush. Specimen sz50.2b also showed some evidence of the tearing mode, and some sheet-like sections the 0° tows were still intact.

As was seen in Figure 6-7 and Figure 6-8, the initial peaks for most of the 50k specimens were

quite large when compared to the average crush loads. This is seen in Figure 6-11, which shows the load ratios for the 50k dynamic specimens. Because the initial peak was not very high for the circular 50k dynamic specimens without 0° tows, the load ratios for these tubes are significantly lower than for any of the other 50k dynamic specimens. Of the other specimens, all have load ratios greater than 2, and specimens cz50.1, cz50.2, sz50.1, and sz50.2 have load ratios equal to or greater than 2.5. In all the 50k dynamic cases, the middle specimens had load ratios about the same as the load ratios of the corresponding end specimens.

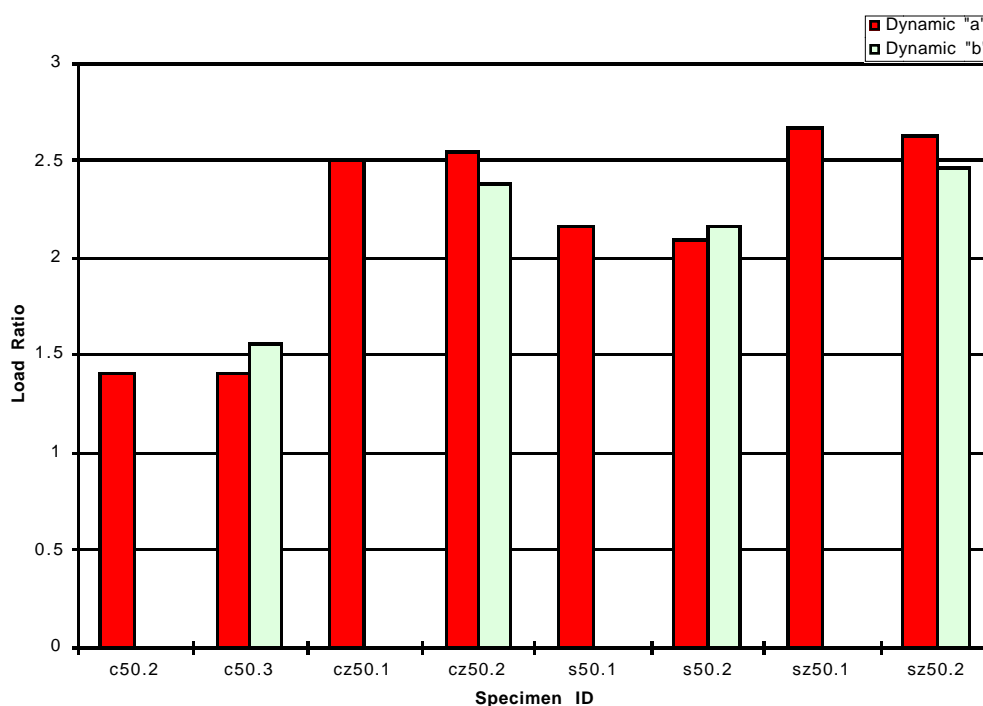


Figure 6-11: Load ratios for the 50k dynamic specimens

The tow overlap positions are given in Table 6-2. It appears that one measurement is missing for s50.2b because the square 50k tubes have the overlaps about 110 mm apart and the first overlap position that is shown in Table 6-2 is at 152 mm; there should also have been an overlap at about 40 mm for specimen s50.2b. Using Figure 6-7, Figure 6-8, and Table 6-2, it can be concluded that there is little or no effect of the tow overlap positions on the crush load for either the circular or square 50k dynamic specimens. Specimens cz50.1 and s50.2a are the only specimens that show

peaks, albeit small peaks, near the overlap position that are distinct from the other valley-to-peak variations seen in the steady crush regions.

Table 6-2: Position, from beveled end, of tow overlaps for the 50k dynamic specimens

Specimen	Position (mm)			
c50.2	48	129	206	284
c50.3a	66	139	216	287
c50.3b	40	114	190	267
cz50.1	60	141	217	297
cz50.2a	77	153	228	296
cz50.2b	53	127	203	281
s50.1	19	133	244	
s50.2a	90	203		
s50.2b		152	264	
sz50.1	98	208		
sz50.2a	27	140	247	
sz50.2b	90	202		

6.3 Comparison of 12k and 50k specimens

The shape of the crush load vs. crush displacement traces depended on the specimen types. Most of the circular 12k tubes all had large valley-to-peak variations in the stable crush region, while all of the square dynamic specimens, both 12k and 50k, had large initial peaks. The circular 50k specimens with 0° tows also had large initial peaks, while the circular 50k specimens without 0° tows did not. In general, the 12k specimens had larger valley-to-peak variations than did the 50k specimens, but the 50k specimens had higher initial peaks.

The average crush loads for the 12k specimens were generally higher than for the 50k specimens. All of the circular 12k specimens had average loads higher than did all of the circular 50k speci-

mens (cz50.1 was almost the same as cz12.2). Regarding the square specimens, the 12k middle specimens had higher average load levels than did the 50k middle specimens, but, the 12k end specimens had average loads similar to the 50k end specimens, with two of the 50k end specimens having higher average loads than any of the 12k end specimens.

As with the average crush load, the SEAs of all the circular 12k specimens were higher than all of the SEAs of the circular 50k specimens. In contrast to the average crush load, the SEAs of all the square 12k specimens were also higher than the SEAs of all the square 50k specimens. With both the 12k and 50k specimens, the circular specimens generally had higher SEAs than the square specimens. All but one of the square 12k specimens (sz12.1) had lower SEAs than the circular 12k specimens, and all of the square 50k specimens had lower SEAs than the circular 50k specimens.

If, as mentioned in [5], a load ratio of less than 1.25 is desirable, then none of these specimens would be acceptable. The 12k specimens without 0° tows had about the same load ratios as the 50k specimens without 0° tows, but the 12k specimens with 0° tows had lower load ratios than all of the 50k specimens with 0° tows.

The 12k specimens showed slight evidence of having the tow overlaps increase the crush load in the vicinity around the overlap. However, the 50k specimens showed no such evidence.

In the dynamic tests the 12k specimens showed significant advantage over the 50k dynamic specimens. The greatest advantage in SEA due to fiber type was seen between the circular 12k and 50k specimens.

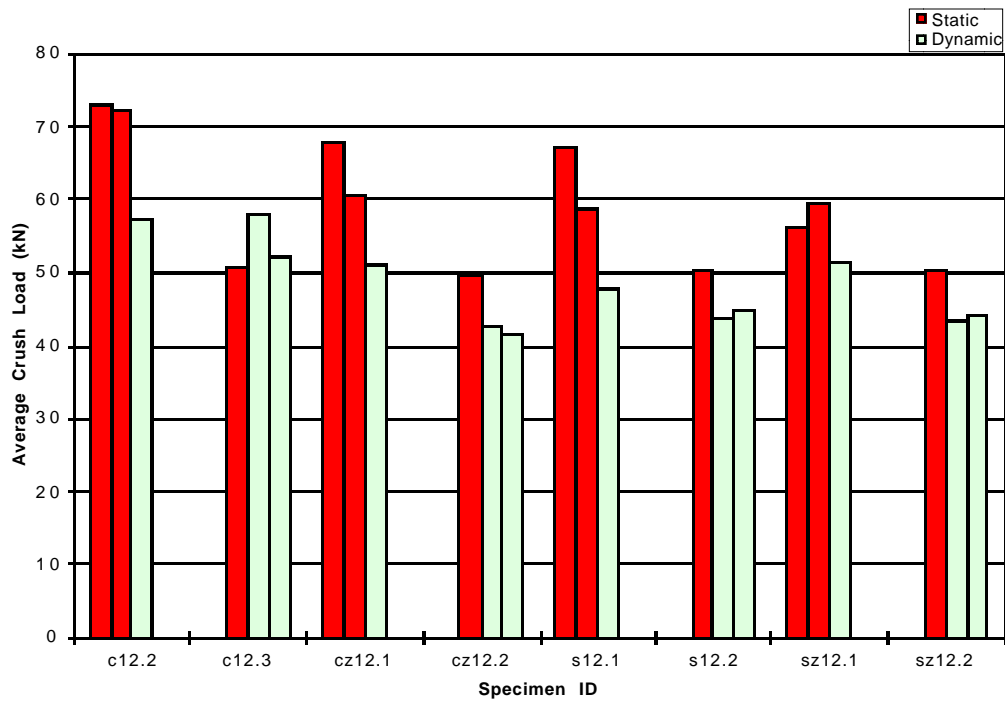
Chapter 7 Comparison of static and dynamic energy absorption characteristics

Although the static and dynamic batteries of specimens have been discussed independently in Chapters 5 and 6, it is important to study the similarities and differences in crushing that are seen when the crush rate is changed. These issues are discussed in this chapter.

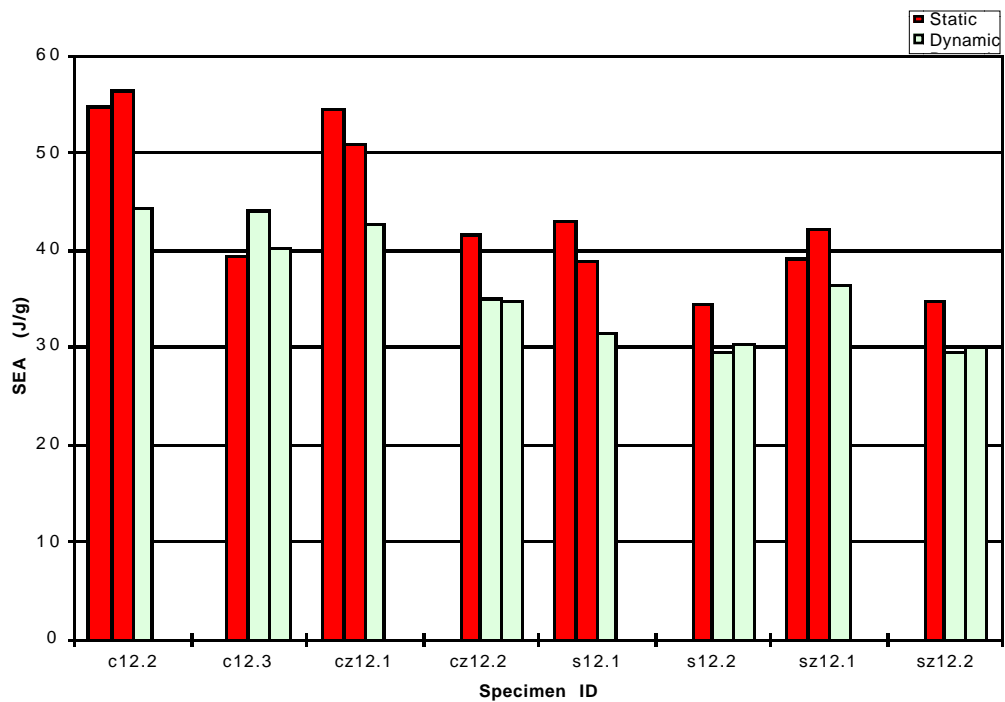
7.1 12k specimens

For both the static and dynamic tests, the main difference seen in the shapes of the crush load vs. crush displacement traces is that the square tubes generally had higher initial peaks than the circular tubes. Both the static and dynamic square 12k specimens had initial crush peaks that were higher than the initial peaks of the circular 12k specimens. Of the 12k specimens, the dynamic square specimens had the most distinct initial peaks.

Figure 7-1 shows the average crush loads and SEAs for all of the 12k specimens. The three specimens cut from each uncut tube are represented by the three columns above the tube name in Figure 7-1. The static specimens are represented by the dark columns, while the light columns represent the dynamic specimens. For each triplet of columns for a given tube, the two columns with the same shading represent the two end specimens cut from a tube; the “a” specimen is shown on the left and the “b” specimen on the right. The column with the other shading represents the single specimen cut from the middle of that tube. The other column charts in this chapter have also been formatted in this manner, which is somewhat different than the previous chapters.



(a)



(b)

Figure 7-1: (a) Average crush load and (b) specific energy absorption for the 12k specimens

It is seen in Figure 7-1 that, for a given tube, the static tests usually had higher average crush loads and SEAs than the dynamic tests. The only exception to this is tube c12.3 for which both of the dynamic specimens had higher average crush loads and SEAs than the static specimen. The 12k specimens from the second set of replicate tubes (c12.3, cz12.2, s12.2, sz12.2) had lower average crush loads and SEAs than the specimens from the first set of tubes (c12.2, cz12.1, s12.1, sz12.1), except for the dynamic specimen c12.3a which had a higher average crush load and SEA than the dynamic specimen c12.2, and static specimen s12.2 which had a higher average crush load and SEA than dynamic specimen s12.1. The circular 12k specimens also tended to have higher SEAs than the square 12k tubes.

The crush modes were more difficult to classify in the dynamic tests than in the static tests. All of the circular specimens showed the socking crush mode (except c12.3 which has already been discussed) and most showed splaying. Also, all of the circular specimens without the 0° tows showed the tearing mode. All of the square specimens showed the tearing crush mode, while all of the square specimens with and one without the 0° tows showed socking. Socking and tearing were the most common crush mode seen for the 12k specimens.

As discussed above, the square specimens showed higher initial peaks than the circular specimens. This is reflected in the load ratios of these specimens seen in Figure 7-2. It is seen, also, that all of the dynamic specimens had higher load ratios than the static specimens from the same tube. The tube that had the closest load ratios between static and dynamic specimens was c12.3, where the dynamic specimens had load ratios only 14% higher than the static specimen. The load ratios of the dynamic specimens were 56% higher than the static specimens for tubes s12.1, and sz12.1 and 57% higher for tube sz12.2. These percentages were calculated using: $[(Load\ Ratio_{dynamic} - Load\ Ratio_{static}) / Load\ Ratio_{static}] \times 100\%$, where the values of load ratio are averages for the two static or two dynamic specimens, depending on how the original tube was cut.

The effect of the tow overlap positions on the crush load was much more pronounced with the 12k static specimens than with the dynamic ones. The presence of the 0° tows seems to accentuate the

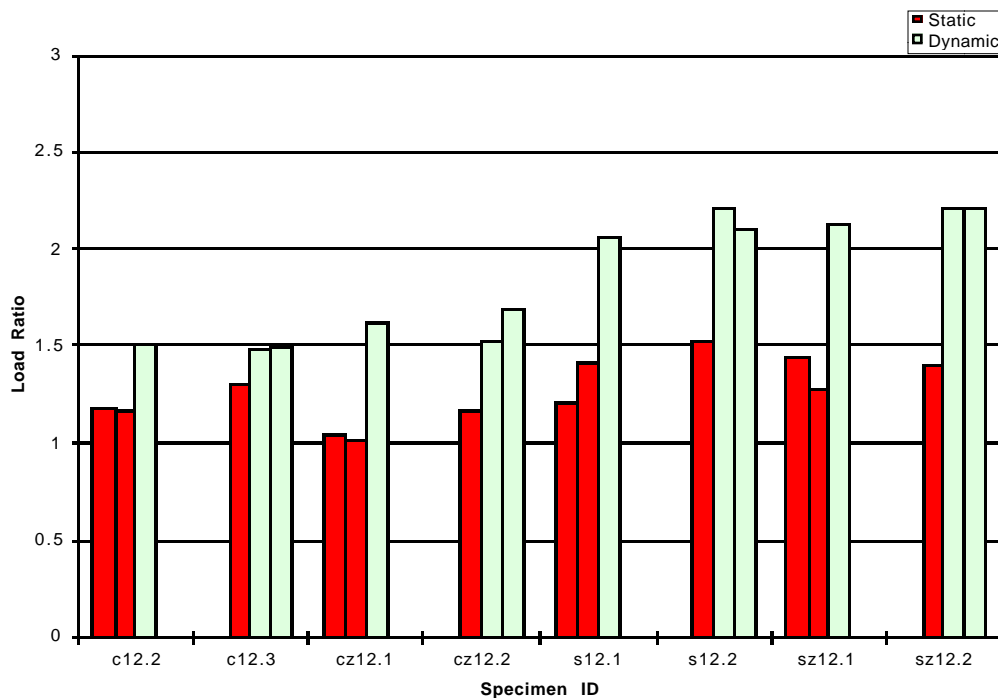


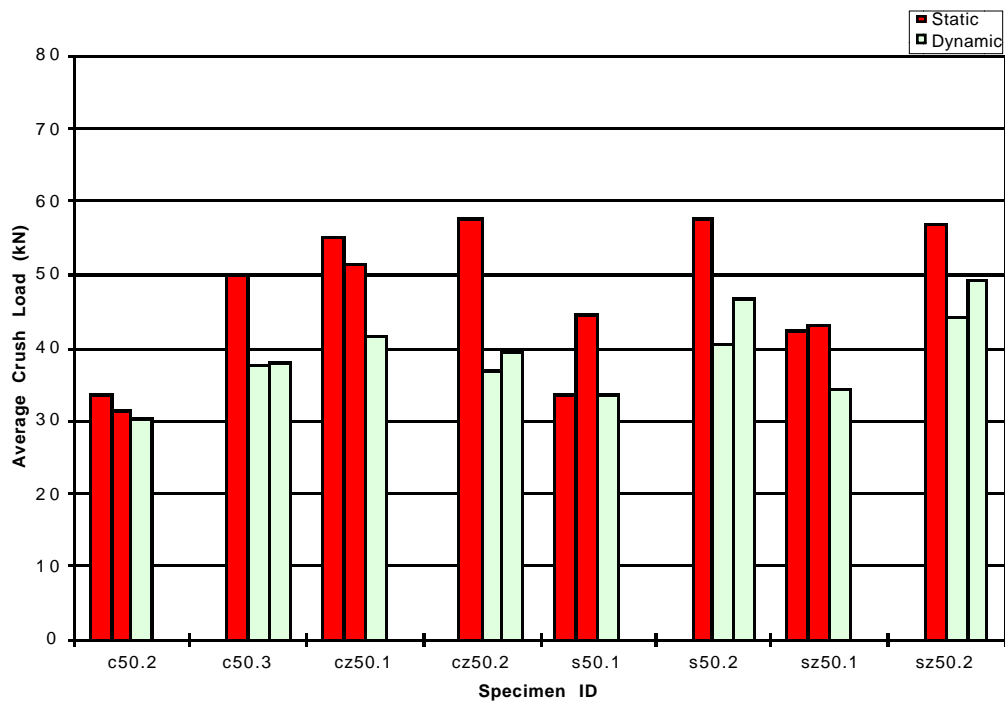
Figure 7-2: Load ratios of the 12k specimens

effect of the tow overlap positions in the static specimens, but not in the dynamic specimens.

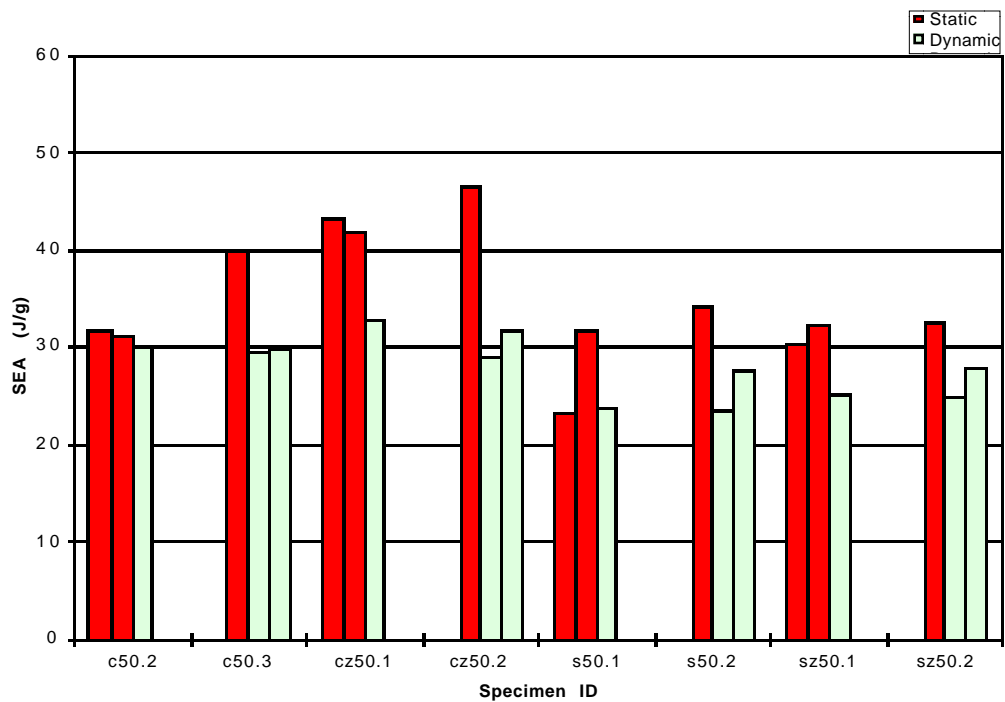
7.2 50k specimens

The main difference seen in the shapes of the crush load vs. crush distance traces of the 50k specimens is the high initial peaks for nine of the twelve dynamic tests. For both the static and the dynamic tests, the square specimens had higher initial peaks than the circular tubes. Also, for the static square and the dynamic circular and square specimens, the presence of the 0° tows made the initial peak more prominent.

The average crush loads and SEAs for the 50k specimens are shown in Figure 7-3. Except for tube s50.1, all of the dynamic 50k specimens cut from a tube had lower average crush loads and SEAs than the static specimens cut from that tube. For both the static and dynamic tests, the square specimens tended to have higher average loads, but lower SEAs, than the circular specimens.



(a)



(b)

Figure 7-3: (a) Average crush loads and (b) specific energy absorption of the 50k specimens

The splaying crushing mode was the most common crush mode seen in the circular 50k specimens. Socking was seen in three of the circular 50k static specimens but only in one of the circular 50k dynamic specimens. The tearing crushing mode was seen in all of the 50k static specimens, but was not as prevalent in the 50k dynamic specimens. Tearing was seen in only four of the six dynamic square 50k specimens.

Due to the high initial peaks seen in most of the dynamic 50k specimens, the load ratios were quite high for most of the 50k dynamic specimens. The load ratios for the 50k specimens are shown in Figure 7-4. The dynamic specimens from a tube all had higher load ratios than the static specimen, or specimens, from that tube. Except for the circular 50k tubes without 0° tows, the dynamic specimens had significantly higher load ratios than the static specimens. The presence of 0° tows led to higher load ratios for the dynamic specimens.

There was not much evidence of the tow overlap positions having an effect on the crush load for either the 50k static or dynamic specimens.

7.3 Comparison of 12k and 50k specimens

As is seen in Figure 7-1a and Figure 7-3a, for the 12k specimens, the square specimens seemed to have average crush loads about the same or lower than the circular specimens, but the square 50k specimens had about the same or higher average crush loads than the 50 circular specimens. For both the static and dynamic specimens the dynamic tests generally had lower average crush loads than the static specimens cut from the same tube. As also seen by comparing these two figures, the average crush loads for the 50k specimens were, overall, lower than the average crush loads for the 12k specimens

It is seen in Figure 7-1b and Figure 7-3b that the SEAs of the circular specimens, both 12k and 50k, and static and dynamic were generally higher than the SEAs of the square specimens. As with the average crush load, the SEAs of the static specimens were generally higher than the

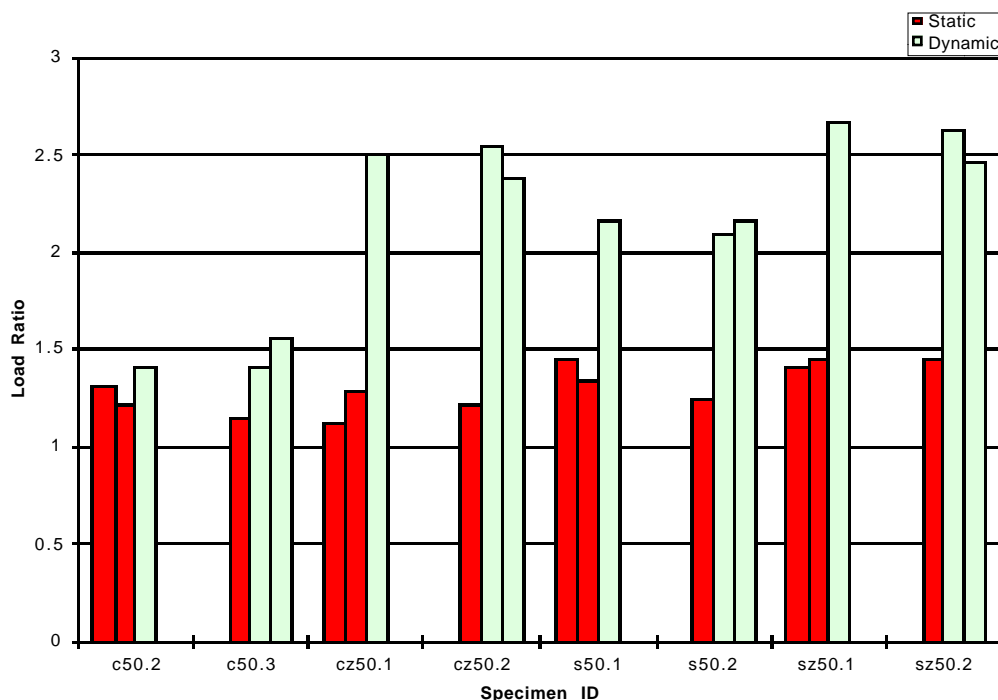


Figure 7-4: Load ratios of the 50k specimens

SEAs of the dynamic specimens cut from the same tube. Overall, the 0° tows did not seem to have a large effect on the SEA. With the 12k specimens, it was originally believed that the middle specimens might be somehow inferior. However, when the SEAs of all of the static 12k specimens are examined together, it is seen that it is the tubes themselves, not the position within the tube that may be inferior. This is evidenced by the fact that the specimens from the first set of 12k tubes (c12.2, cz12.1, s12.1, sz12.1) had higher SEAs than specimens from the second set of 12k tubes. This is a puzzling result because both sets of 12k tubes were fabricated in the same manner. The circular 50k static and dynamic specimens showed an opposite trend. The static specimens from the second set of circular 50k tubes, tubes with the tighter tow spacing, had higher SEAs than specimens from the first set of tubes. In contrast, the circular dynamic specimens from the tubes with the tighter tow spacing actually had lower SEAs than those from the first set of tubes. Both the static and dynamic specimens from the square tubes with the tighter tow spacing had slightly higher SEAs than the specimens from the square tubes with the wider tow spacing. The net effect is that no general statement can be made. By comparing Figure 7-1b and Figure 7-3b, it is seen, however, that overall, the SEA of the 12k material is higher than the SEA of the 50k material.

The crush modes in the 50k specimens were more difficult to classify than for the 12k specimens. The socking crushing mode was much more common in the 12k specimens than in the 50k specimens. In the square 12k specimens, the presence of the 0° fibers made the socking crushing mode more pronounced, but this was not the case for the square 50k specimens. The square 12k specimens all showed the tearing crushing mode. Tearing was also seen in all of the static square 50k specimens but only in two of the dynamic square 50k specimens.

All of the dynamic specimens had higher load ratios than the static specimens from the same tube. Also, the square specimens tended to have higher load ratios than the circular specimens. There was not much difference in load ratio between corresponding 12k and 50k static specimens. However, the dynamic 50k specimens with 0° tows had considerably higher SEAs than the corresponding dynamic 12k specimens, but the dynamic 50k specimens without 0° tows had SEAs similar to the corresponding 12k specimens.

Chapter 8 Conclusions and recommendations

8.1 Conclusions

Outlined in Chapter 1 were four specific objectives for this research effort. The experimental procedure was designed in such a manner provide answers to these objectives. These objectives were to compare how the energy absorption characteristics were changed by varying several parameters:

- *two types of graphite fiber: lower cost Fortafil 50k fiber and aerospace-grade T300 12k fiber*

The specimens with the 12k tows had higher specific energy absorption than the specimens with the 50k tows. The SEAs were fairly close for the static specimens with 12k and 50k tows but in the dynamic tests those specimens with the 12k tows clearly had higher SEAs. However, perhaps this loss of energy absorption capability would be acceptable considering the substantial cost savings of the 50k material.

- *two different stacking sequences: with $\pm 45^\circ$ tows and with $\pm 45^\circ$ and 0° tows*

The stacking sequences did not seem to have a large effect on the SEA but did contribute in other ways. The stacking sequence played a part in determining the crush mode and the shape of the crush load vs. crush displacement traces.

- *two different specimens geometries: circular and square cross-section tubes*

The specimen geometry played a major role in determining the energy absorption characteristics. The circular specimens tended to have higher SEAs than the square specimens. The circular and square specimens also showed different crush modes and the square specimens generally had higher load ratios.

- *different crush rates: static crushing and dynamic impact crushing*

The rate of crush was also significant. The specimens tested statically tended to absorb more energy than those tested dynamically. Also, the dynamic specimens generally had higher load ratios and the crush modes were slightly different.

8.2 Recommendations

The high tow count material has proven that it can be effective in energy absorption, so further study is warranted. There are many interesting avenues to explore as a continuation of this work. Several of these are:

- *Try to improve the energy absorption characteristics of the 50k towpreg.*

Further work and experimentation with the 50k towpreg might yield higher quality tubes.

If the winding tension were increased, then the consolidation might be better, producing higher energy absorption.

- *Change the crush initiator.*

Because the load ratios were quite high for most of the specimens, different crush initiators could be used in order to try to lower the initial peak.

- *Because the automotive industry is such a high volume business, part processing times must be shortened.*

Filament winding time are unacceptable, and for this reason a similar research effort could be pursued, but with specimens made with a faster manufacturing process. Perhaps, one of the resin injection techniques could be used.

- *If filament winding were not used, the fiber architecture would have to be different.*

The use of a braided preform could be used in conjunction with resin injection or RTM. Also, Atkins and Pearce now braids tubes with the Thiokol towpreg used in this study. If the braided towpreg were used, the filament wound and braided architecture could be compared directly.

- *A resin system that the automotive industry is more interested in could be selected.*

Perhaps, a vinyl ester resin could be used, as was contemplated at one time for this effort.

References

1. McConnell, V. P. ed. *Automotive Composites: A Design and Manufacturing Guide*, Ray Publishing, Wheat Ridge, CO, Vol. 1, 1997, pp. 6-7.
2. Piellisch, Richard. "Beyond Gasoline: Autos Remain Elusive for Carbon Composite Structures, but Alternative Cars Still Hold a Great Market Potential," *SAMPE Journal*, Vol. 32, No. 5, 1996, pp. 14-17.
3. Ashley, Steven. "Composite Car Structures Pass The Crash Test," *Mechanical Engineering*, Vol. 118, No. 12, December 1996, pp. 59-63.
4. Wallentowitz, H. and Adam, H. "The Use of Energy Absorbing Reinforcements in Automotive Applications," *SAMPE Journal*, Vol. 31, No. 5, September/October 1995, pp. 23-28.
5. Karbhari, Vistasp M., Falzon, Paul J., and Herzberg, Israel "Energy Absorption Characteristics of Hybrid Braided Composite Tubes," *Journal of Composite Materials*, Vol. 31, No. 12, 1997, pp. 1165-1186.
6. Thornton, P. H. "Energy Absorption in Composite Structures," *Journal of Composite Materials*, Vol. 13, July 1979, pp. 247-263.
7. Thornton, P. H. "The Crush of Fiber-Reinforced Plastics," in *Handbook of Ceramics and Composites Volume 1: Synthesis and Properties*, Cheremisinoff, N. P. ed., Marcel Dekker Inc., New York, 1990, pp. 307-337.
8. Hull, D. "Energy Absorption of Composite Materials under Crash Conditions," *Proceedings of the Fourth International Conference on Composite Materials (ICCM IV)*, Vol. 1, Oct. 25-28 1982, pp. 861-870.
9. Johnson, W. and Reid, S. R. "Metallic Energy Dissipating Systems," *Applied Mechanics Reviews*, Vol. 31, No. 3, March 1978, pp. 277-287.
10. Farley, Gary L and Jones, Robert M. "Crushing Characteristics of Continuous Fiber-Reinforced Composite Tubes," *Journal of Composite Materials*, Vol. 26, No. 1, 1992, pp. 37-50.
11. Hull, D. "A Unified Approach to Progressive Crushing of Fibre-Reinforced Composite Tubes," *Composite Science and Technology*, Vol. 40, 1991, pp. 377-421.
12. Farley, Gary L. "Energy Absorption of Composite Materials," *Journal of Composite Materials*, Vol. 17, May 1983, pp. 267-279.
13. Schmueser, D. W. and Wickliffe, L. E. "Impact Energy Absorption of the Continuous Fiber Composite Tubes," *Journal of Engineering Materials and Technology*, Vol. 109, January 1987, pp. 72-77.

References

14. Karbhari, Vistasp M. "Progressive Crush of Resin Transfer Molded Square Tube Stiffened Beam Elements," *Journal of Composite Materials*, Vol. 31, No. 10. 1997, pp. 981-1001.
15. Hamada, H., Coppala, J. C., Hull, D., Maekawa, Z., and Sato, H. "Comparison of Energy Absorption of Carbon/Epoxy and Carbon/PEEK Composite Tubes," *Composites*, Vol. 23. Number 4. July 1992, pp. 245-252.
16. Farley, Gary L. "Effect of Fiber and Matrix Maximum Strain on the Energy Absorption of Composite Materials," *Journal of Composite Materials*, Vol. 20, July 1986, pp. 322-334.
17. Farley, Gary L., Bird, Richard K., and Modlin, John T. "The Role of Fiber and Matrix in Crash Energy Absorption of Composite Materials," *Journal of the American Helicopter Society*, April 1989, pp. 52-58.
18. Hamada, H., Nakai, A., Kameo, K., and Takeda, N. "Crushing Performance of Braided Composites," *Proceedings of the Eighth Japan-U. S. Conference on Composite Materials*, September 24-25, 1998, pp. 467-475.
19. Lavoie, J. André and Morton, John. "Design and Application of a Quasistatic Crush Test Fixture for Investigating Scale Effects in Energy Absorbing Composite Plates," *NASA Contractor Report 4526*, July 1993.
20. Thornton, P. H. and Edwards, P. J. "Energy Absorption in Composite Tubes," *Journal of Composite Materials*, Vol. 16, November 1982, pp. 521-544.
21. Thornton, P. H. "The Crush Behavior of Pultruded Tubes at High Strain Rates," *Journal of Composite Materials*, Vol. 24, June 1990, pp. 594-615.
22. Fairful, A.H. and Hull, D. "Effects of Specimen Dimensions On the Specific Energy Absorption of Fibre Composite Tubes." *Proceedings of Sixth International Conference On Composite Materials (ICCM VI) and Second European Conference On Composite Materials (ECCM II)*, Vol. 3, July 20-24 1987, pp. 3.36-3.45.
23. Farley, Gary L. "Effect of Specimen Geometry on the Energy Absorption Capability of Composite Materials," *Journal of Composite Materials*, Vol. 20, July 1986, pp. 390-400.
24. Farley, Gary L. "Technical Note: Energy-Absorption Capability and Scalability of Square Cross Section Composite Tube Specimens," *Journal of the American Helicopter Society*, April 1989, pp. 59-62.
25. Farley, Gary L., Jones, Robert M. "Crushing Characteristics of Composite Tubes with 'Near-Elliptical' Cross Section," *Journal of Composite Materials*, Vol. 26, No. 12, 1992, pp. 1741-1751.
26. Thusis, H. G. S. J., Metz, V. H. "The Influence of Trigger Configurations and Laminate Lay-Up on The Failure Mode of Composite Crush Cylinders," *Composite Structures*, Vol. 25, pp. 37-43.
27. Sigalas, I., Kumosa, M., and Hull, D. "Trigger Mechanisms in Energy-Absorbing Glass Cloth/Epoxy Tubes," *Composite Science and Technology*, Vol. 40, 1991, pp. 265-287.
28. Farley, Gary L. "The Effect of Crushing Speed on the Energy-Absorption Capability of Composite Tubes," *Journal of Composite Materials*, Vol. 25, October 1991, pp. 1314-1329.
29. Farley, Gary L., Wolterman, Richard L., and Kennedy, John M. "The Effects of Crushing Surface Roughness on the Crushing Characteristics of Composite Tubes," *Journal of the American Helicopter Society*, July 1992, pp. 53-60.

References

30. Farley, Gary L. and Jones, Robert M. "Analogy for the Effect of Material and Geometrical Variables on Energy-Absorption Capability of Composite Tubes," *Journal of Composite Materials*, Vol. 26, No. 1, 1992, pp. 78-89.
31. Farley, Gary L. and Jones, Robert M. "Prediction of the Energy-Absorption Capability of Composite Tubes," *Journal of Composite Materials*, Vol. 26, no. 3, 1992, pp. 388-404.
32. Faruque, M. Omar and Wang, Han C. "Crash Analysis of Structures Made of Laminated Fibre Reinforced Composites," *AMD-Vol. 210/BED-Vol. 30, Crashworthiness and Occupant Protection in Transportation Systems*, ASME 1995, pp. 191-201.
33. Thiokol, TCR™ Composites Division, P.O. Box 707, M/S 230, Brigham City, UT 84302-0707, (800) TC-RESIN.
34. Atkins and Pearce Technology, Inc., 1 Braidway, Covington, KY 41017-9702, (800) 837-7477.
35. The Dow Chemical Company, 2301 North Brazosport Blvd., B-1603, Freeport, TX 77541-3257, (800) 441-4369.
36. Composite Machines Company, 3211 South 300 West, Salt Lake City, UT 84115, (801) 466-2686.
37. Flexicon Pacific, Inc., 1219 West Trenton Ave., Orange, CA 92667, (714) 633 9820.
38. Dunstone Company, Inc., 2104 Crown View Dr., Charlotte, NC 28227, (704) 841-1383.

Appendix Data traces from dynamic tests

The load on the impact plate and acceleration of the drop head were recorded during the dynamic tests. On recommendation from General Motors, the load, not the acceleration, was used to obtain the crush distance, and then the load was plotted vs. the crush distance. The acceleration was integrated as a check.

Shown here are six traces for each dynamic test. The top left trace is the load on the impact plate plotted vs. time. Below are plots of the speed and crush distance, obtained through division by mass and integration, vs. time. These integrations were discussed in Chapter 2. The top right trace shows the acceleration of the drop head plotted vs. time and below that, the first integral of the acceleration, the speed, plotted vs. time. The trace on the bottom right shows the load plotted vs. the crush length obtained from the load, and is the same as is seen in the crush load vs. crush length trace shown in Chapter 6 for each specimen. The important point to note is that the velocity obtained by integrating acceleration data (middle right) is always noisier than the velocity obtained by integrating the force divided by the mass (middle left). Furthermore, integrating the acceleration often leads to significant negative velocities. Significant negative velocities indicate a large rebound of the dropped specimens, an event that was never observed.

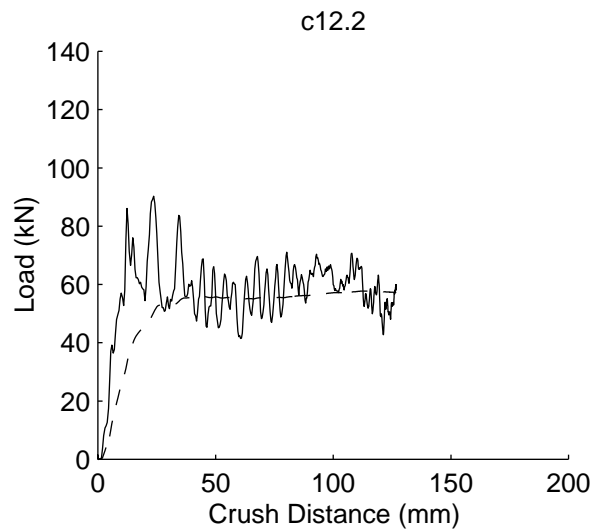
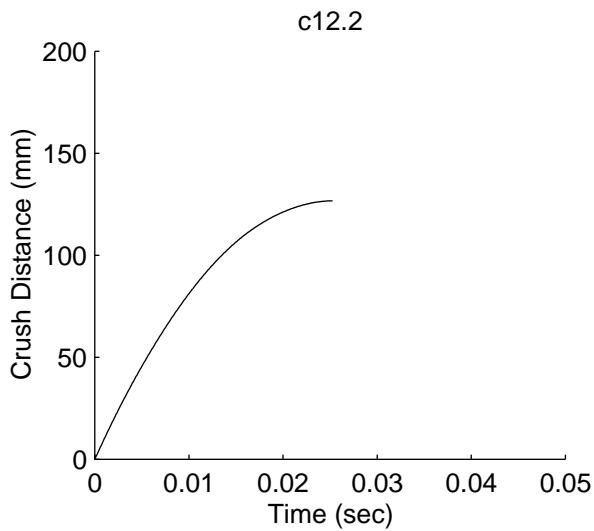
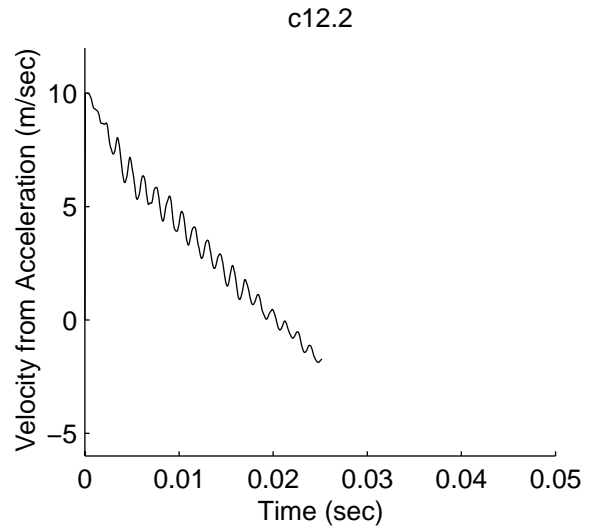
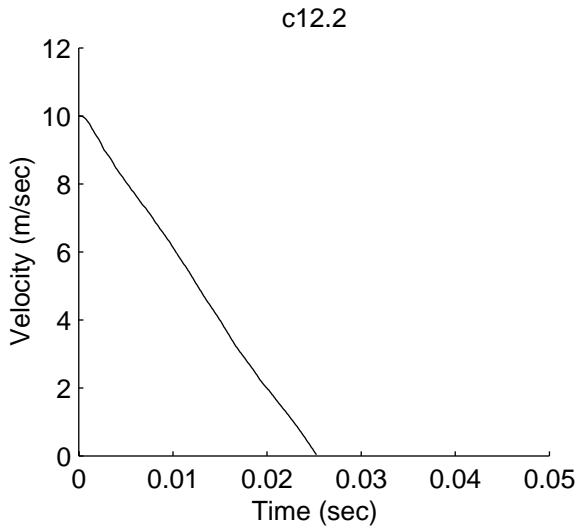
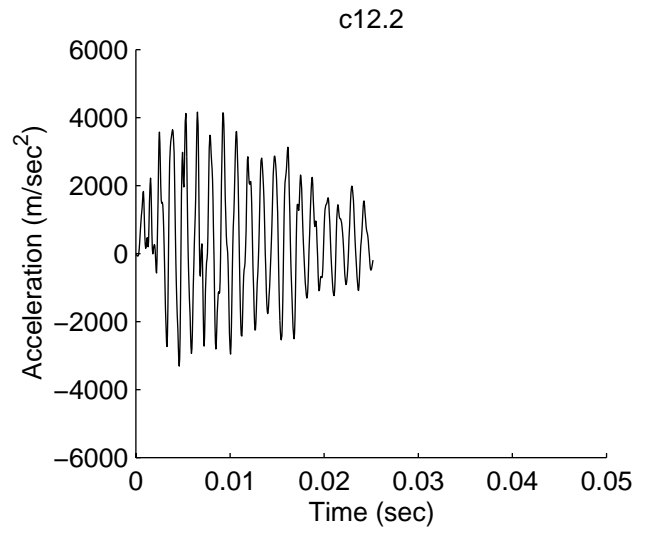
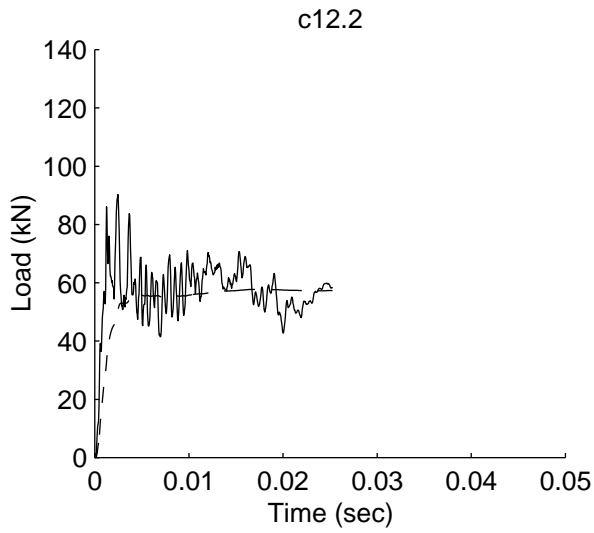


Figure A-1: Dynamic data traces for c12.2

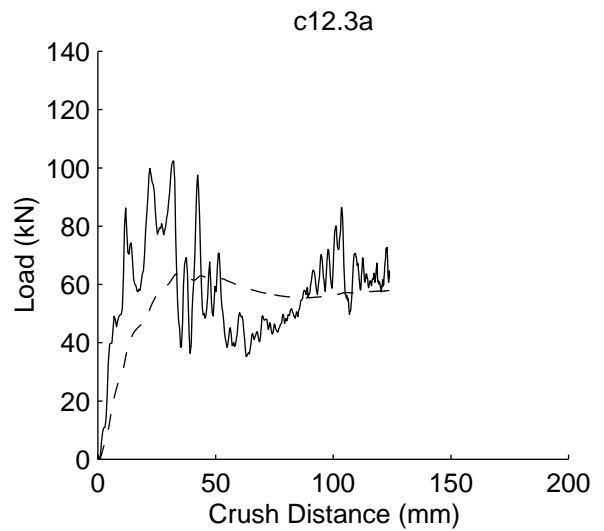
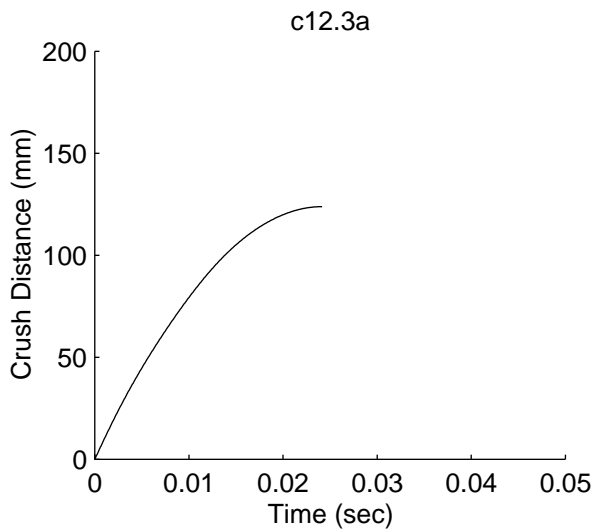
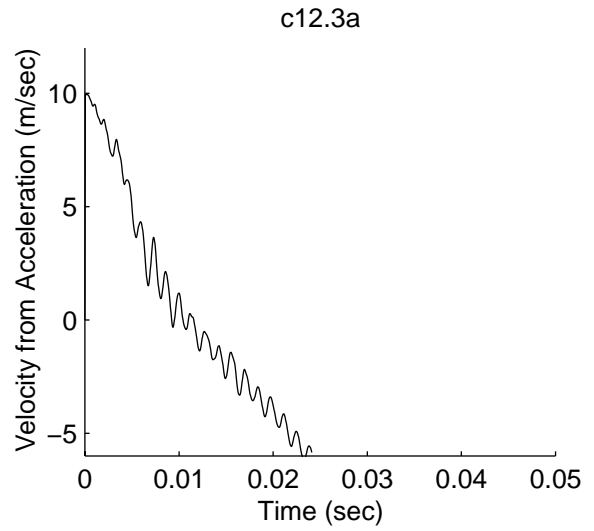
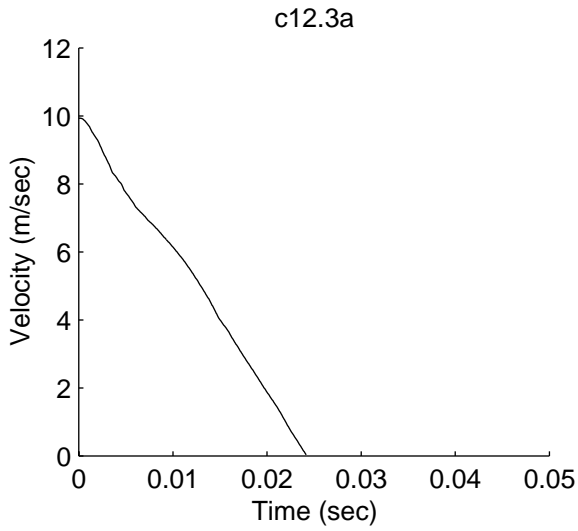
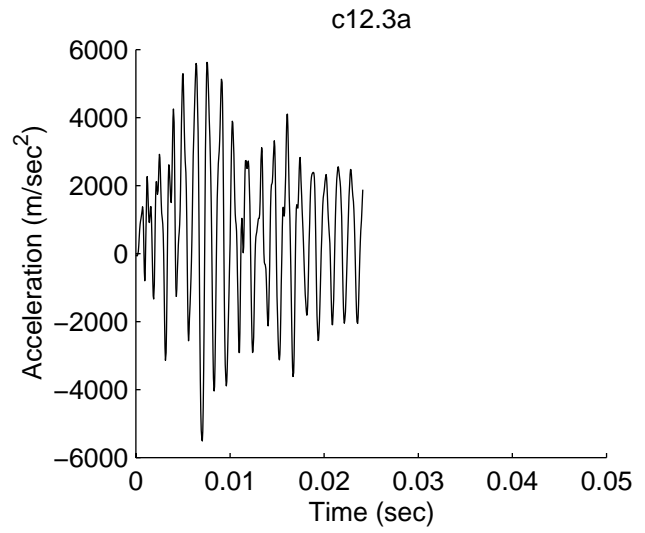
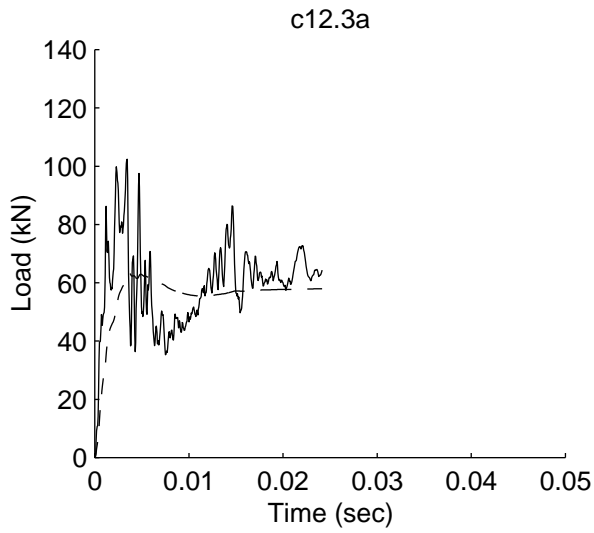


Figure A-2: Dynamic data traces for c12.3a

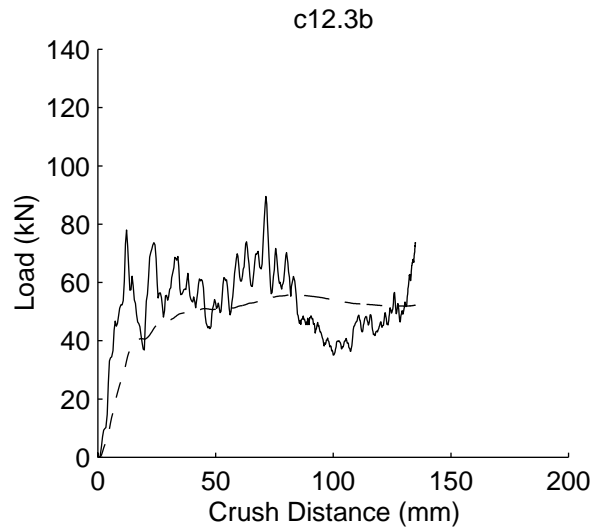
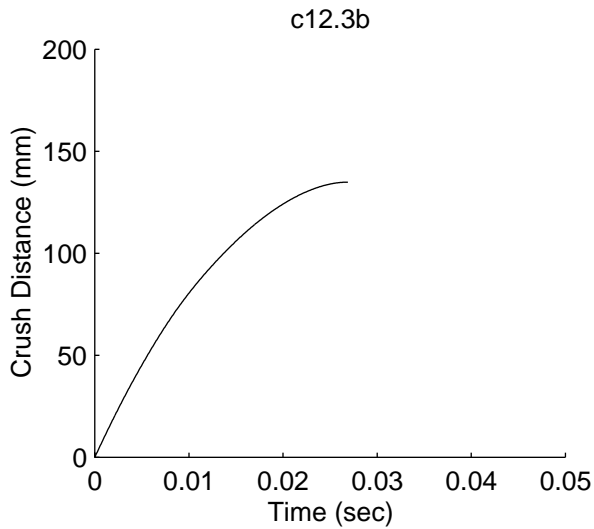
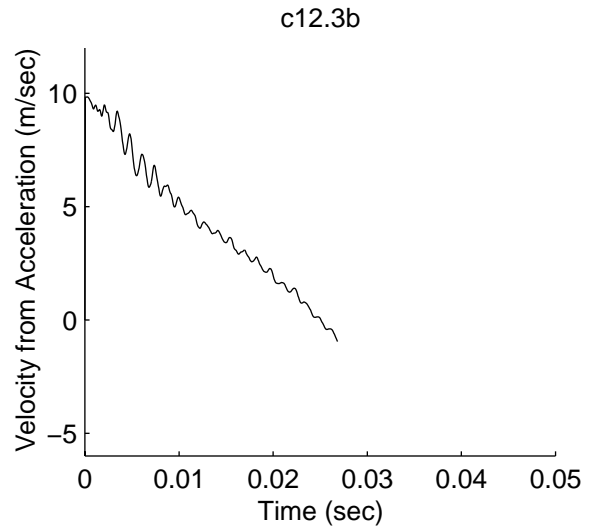
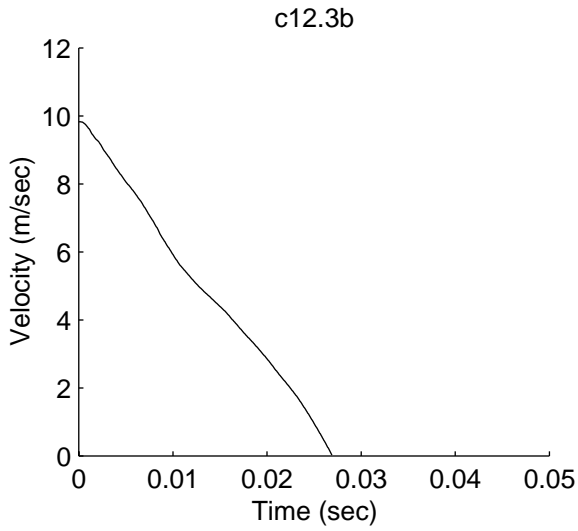
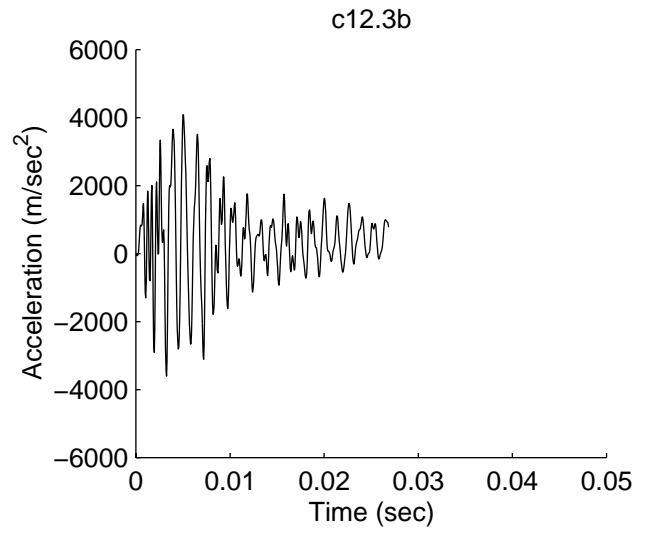
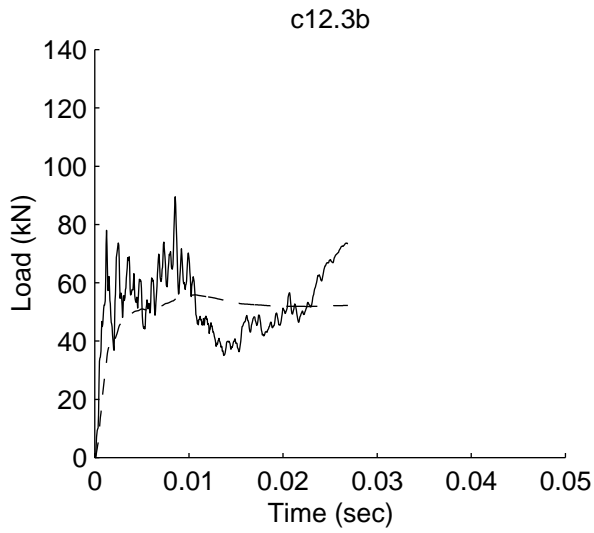


Figure A-3: Dynamic data traces for c12.3b

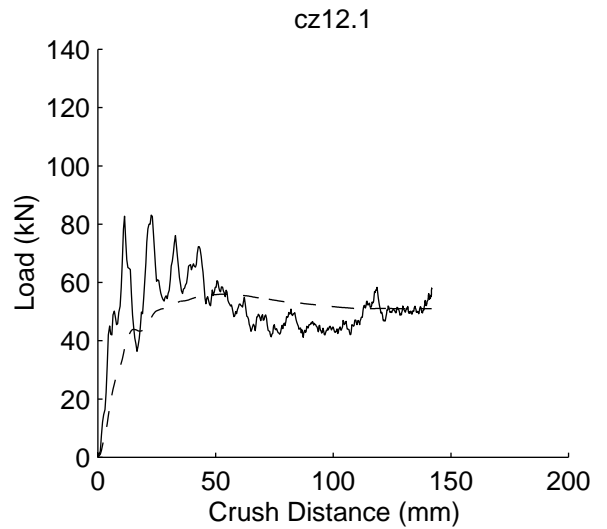
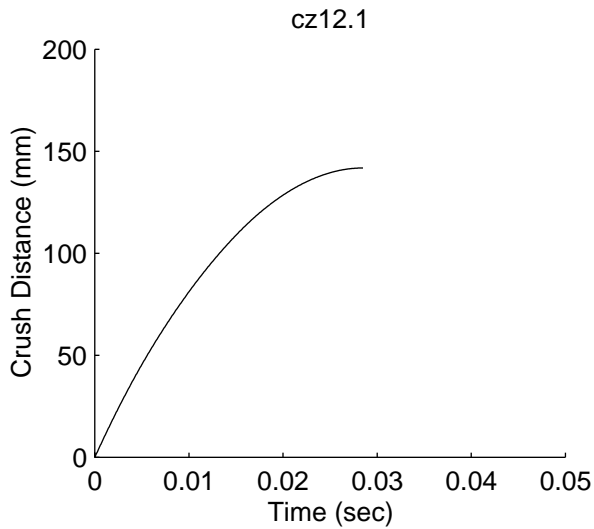
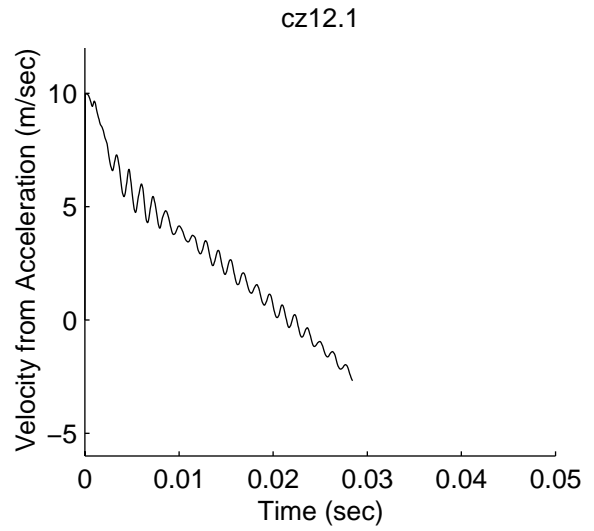
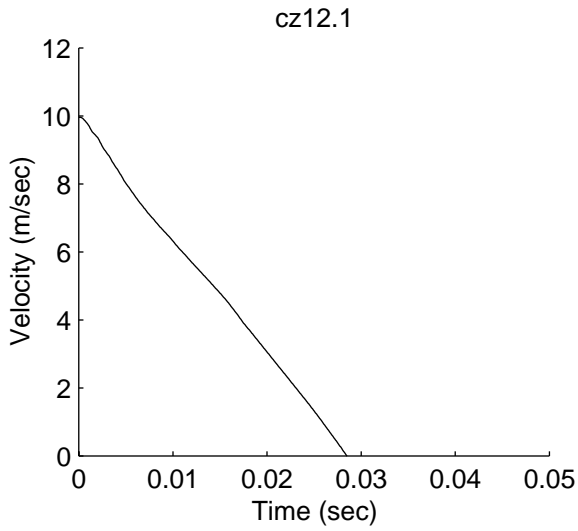
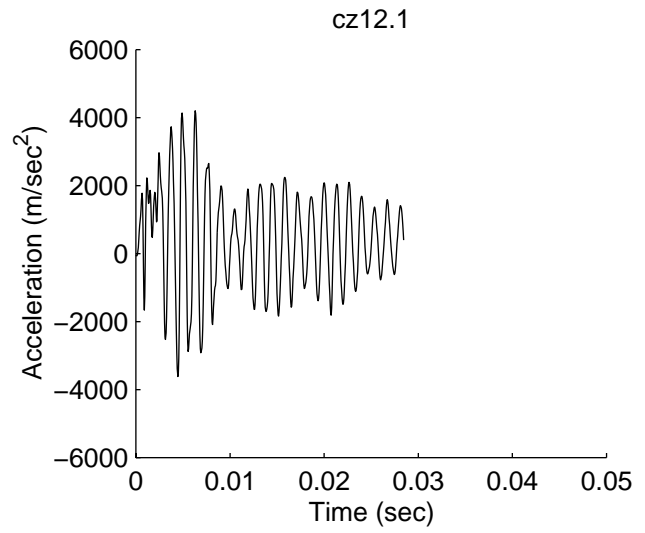
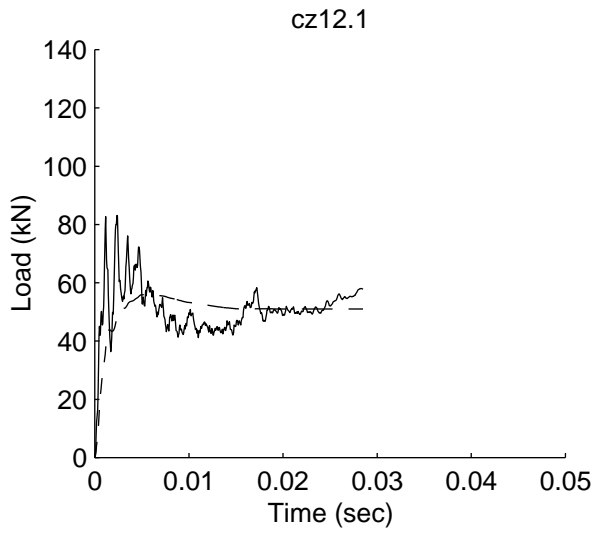


Figure A-4: Dynamic data traces for cz12.1

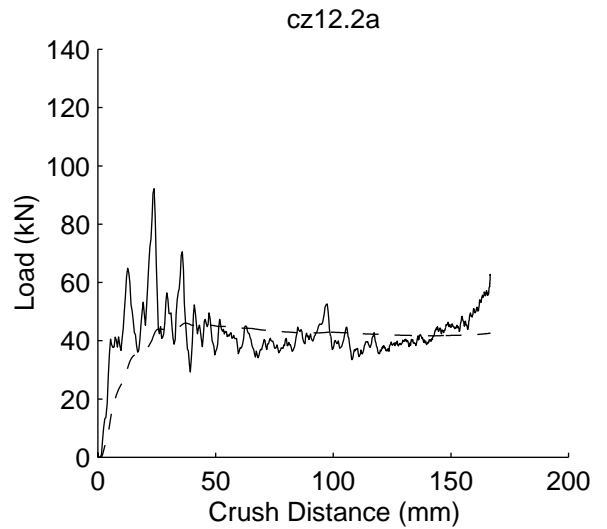
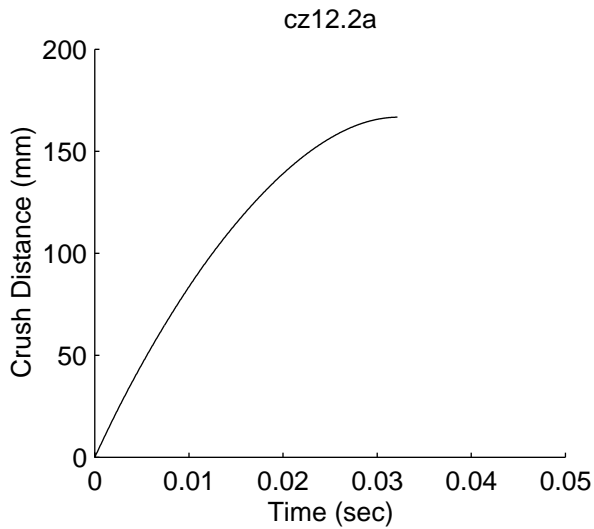
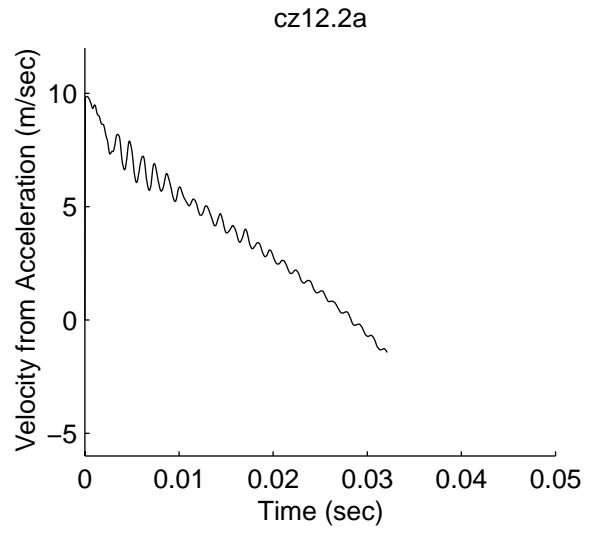
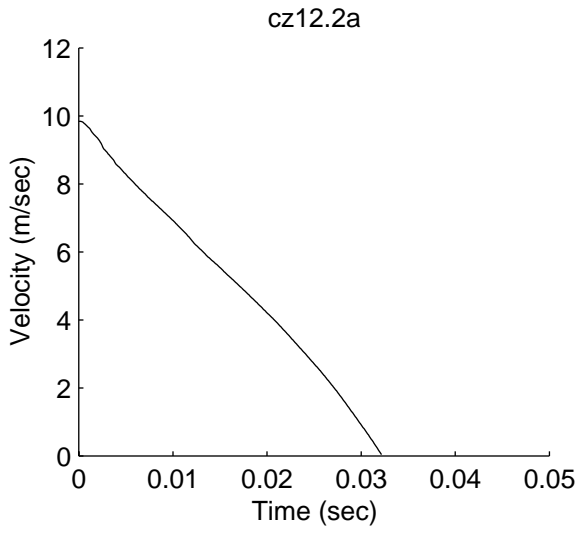
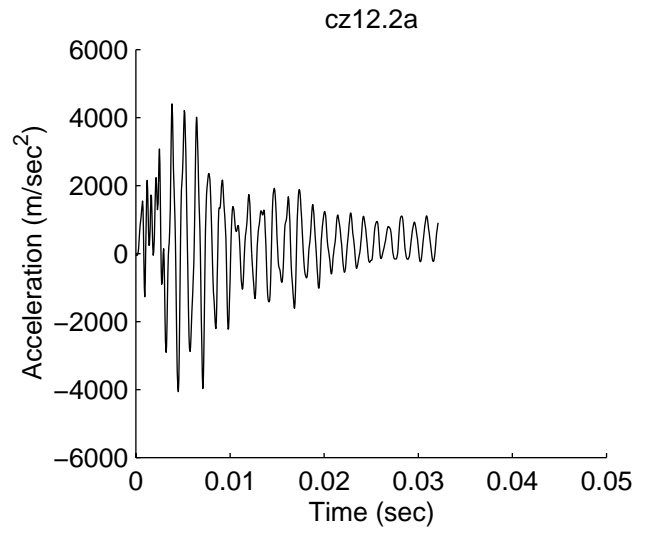
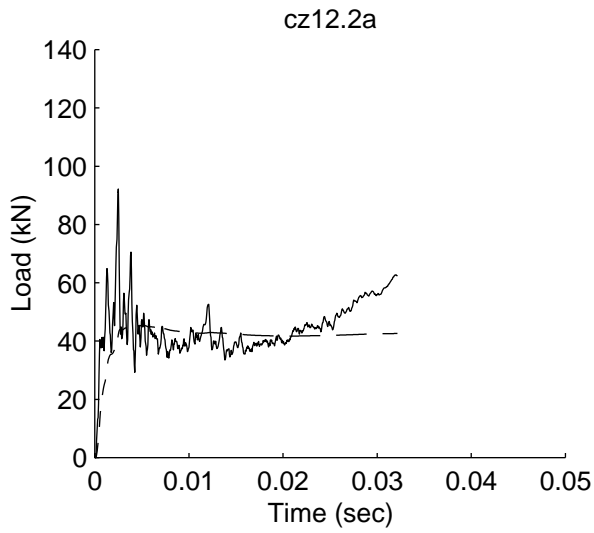


Figure A-5: Dynamic data traces for cz12.2a

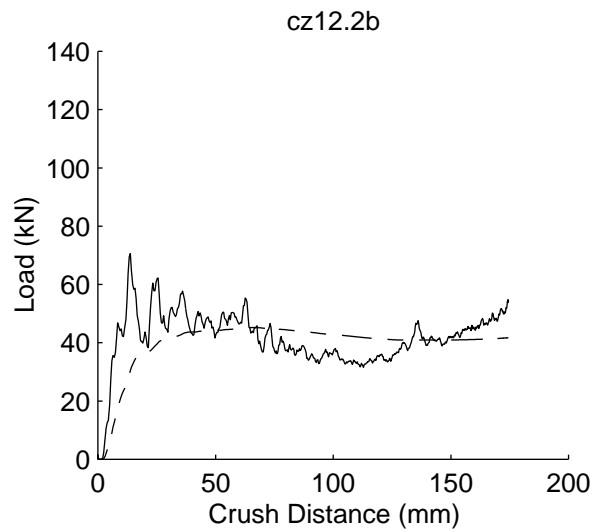
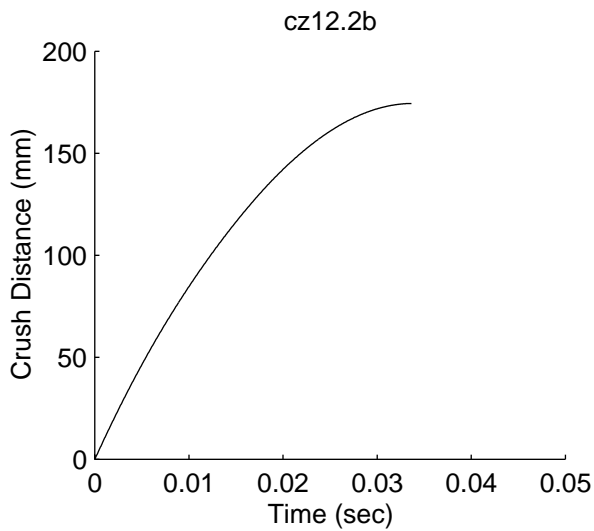
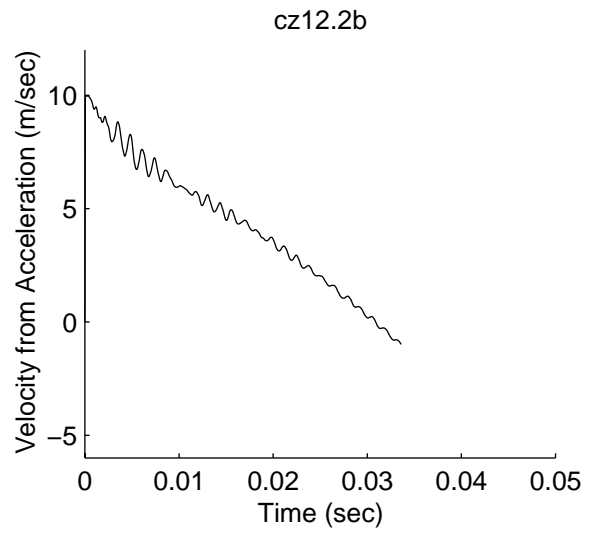
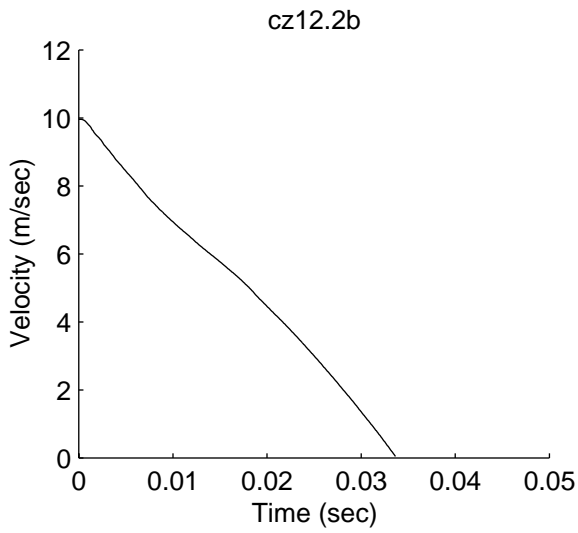
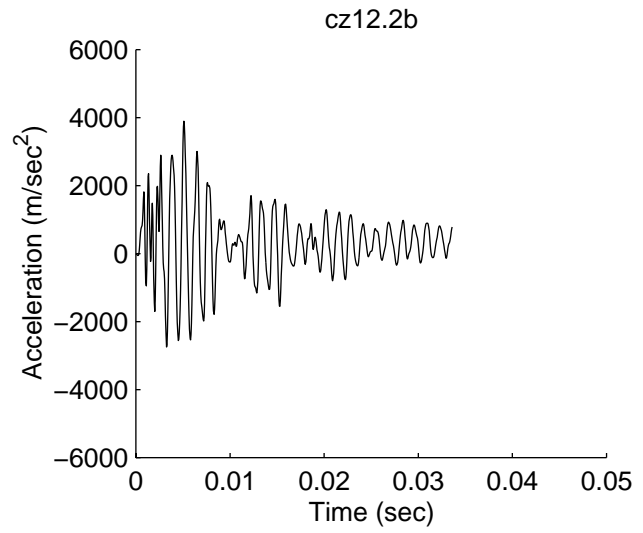
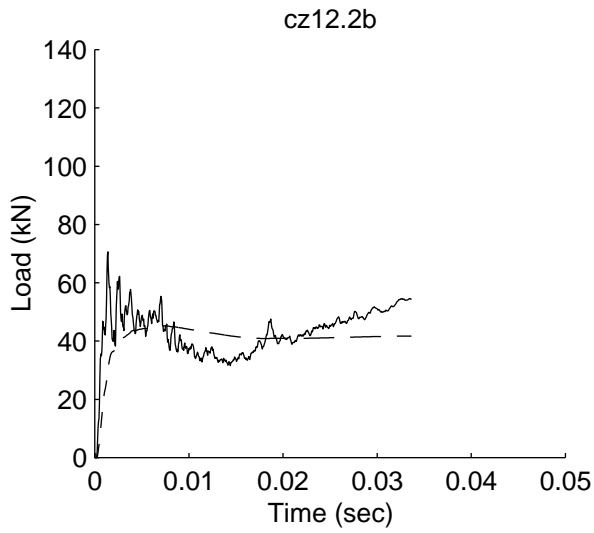


Figure A-6: Dynamic data traces for cz12.2b

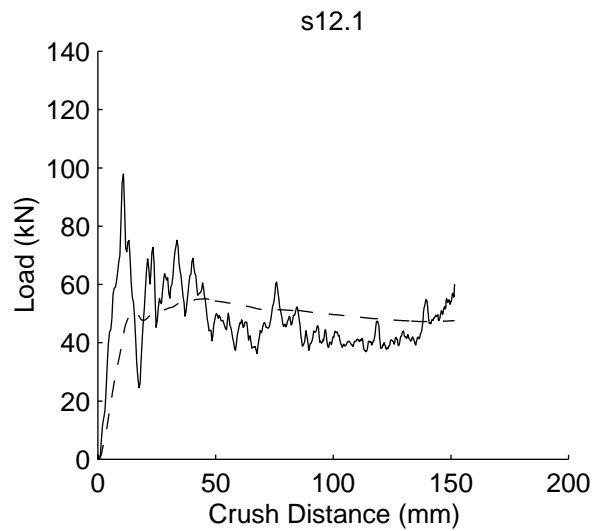
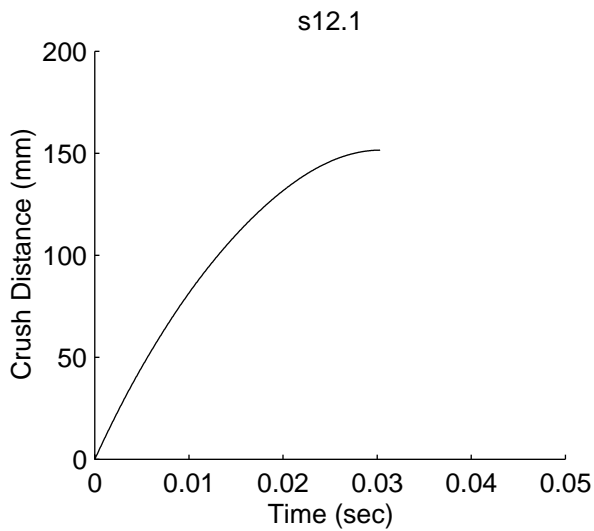
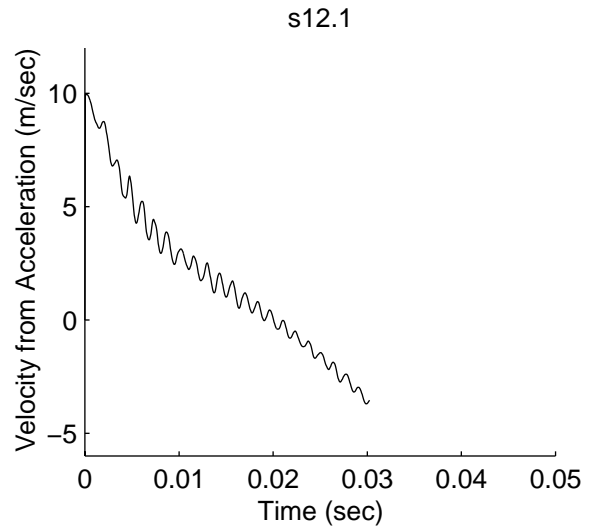
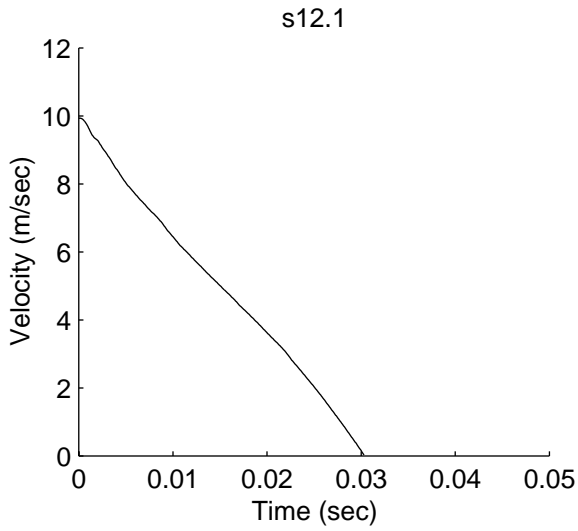
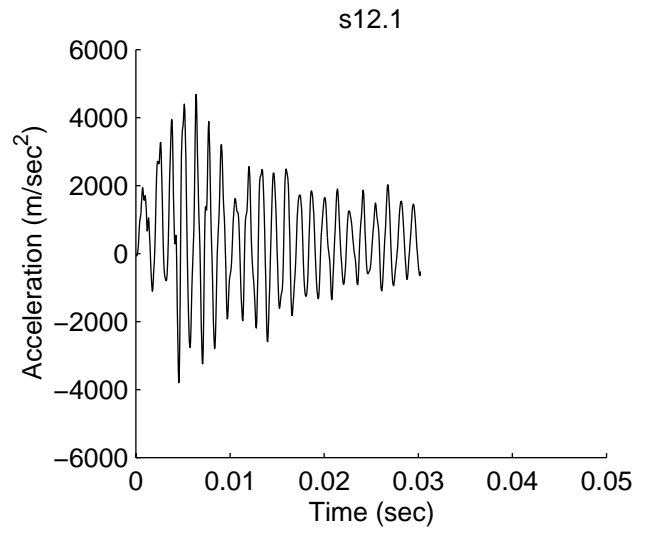
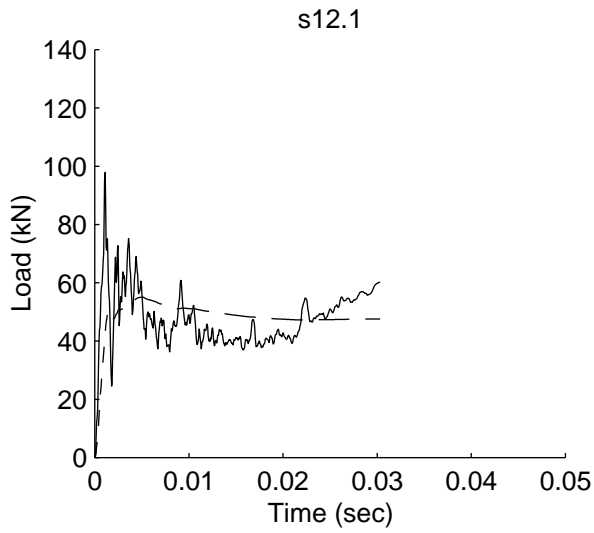


Figure A-7: Dynamic data traces for s12.1

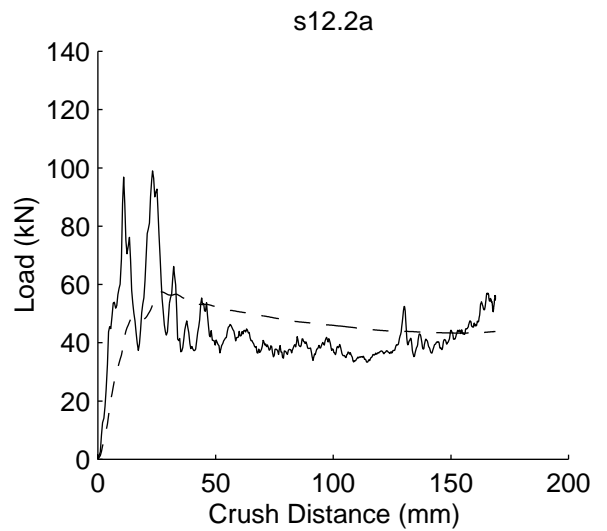
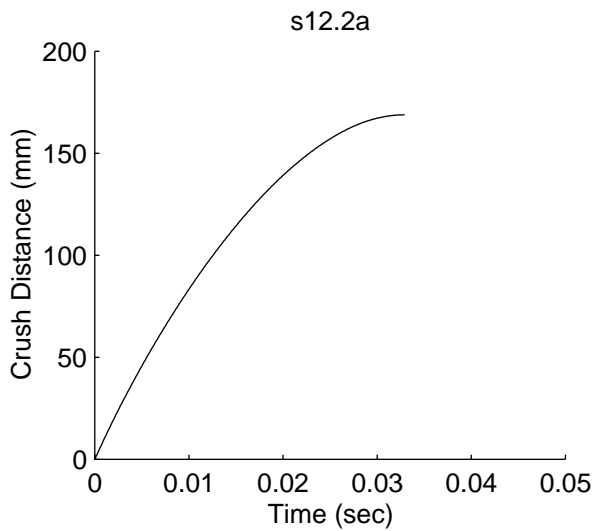
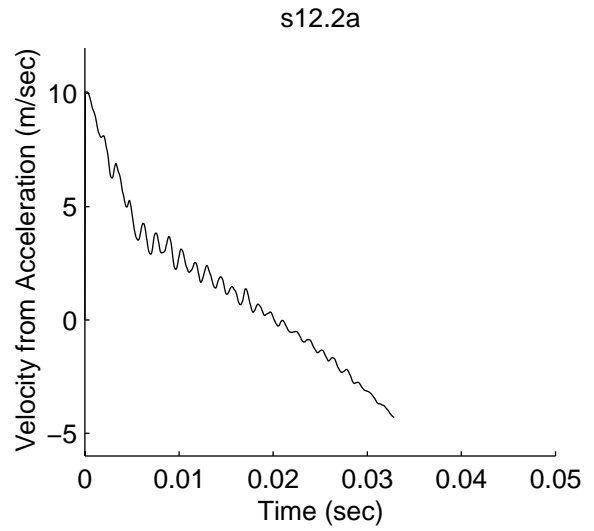
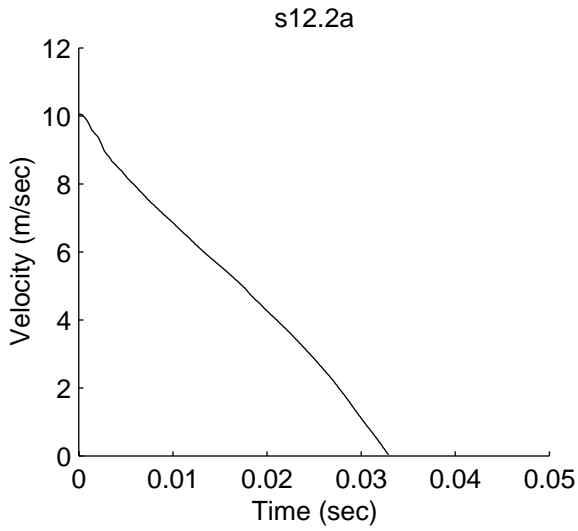
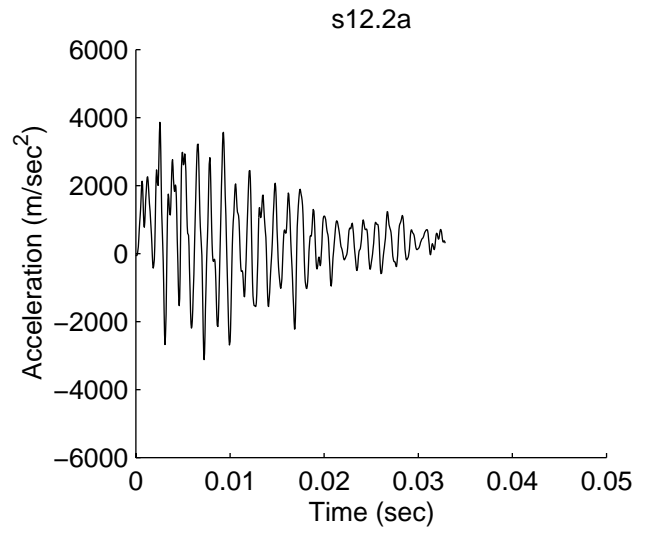
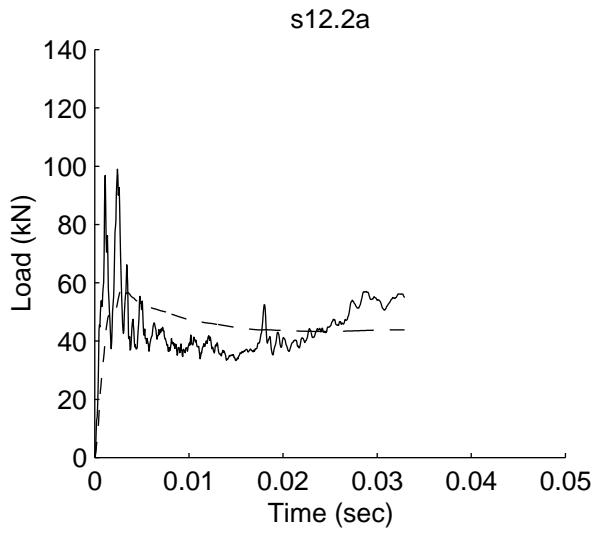


Figure A-8: Dynamic data traces for s12.2a

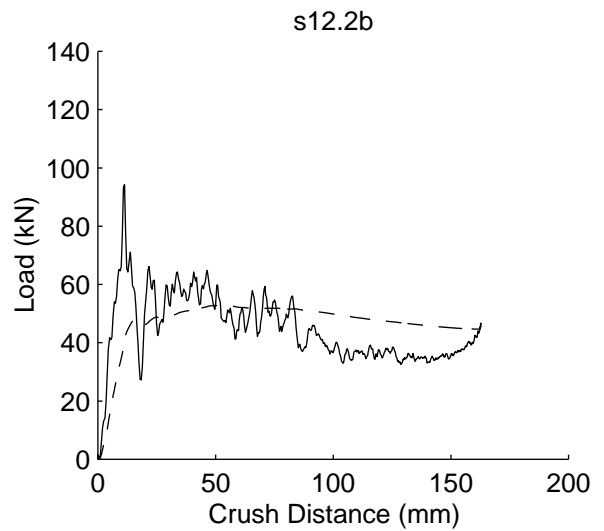
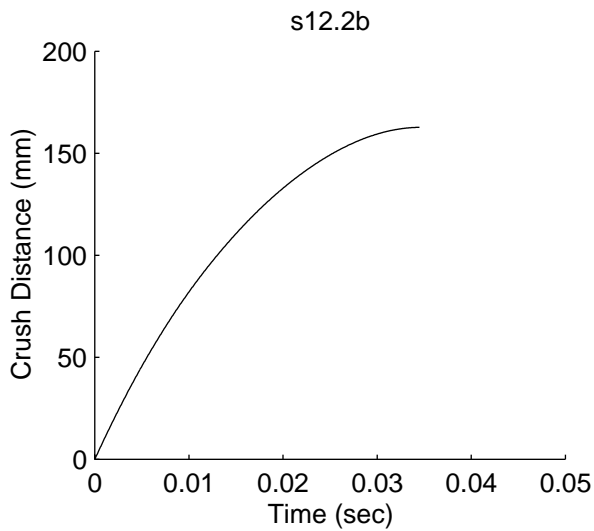
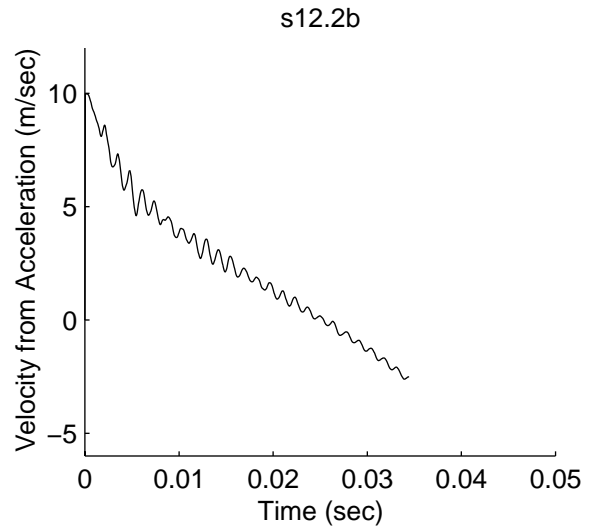
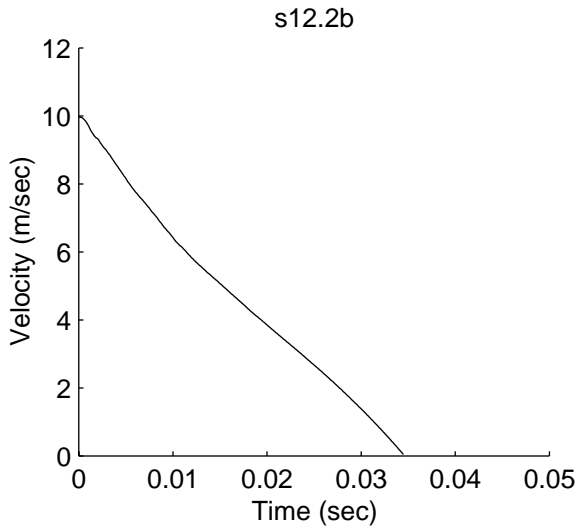
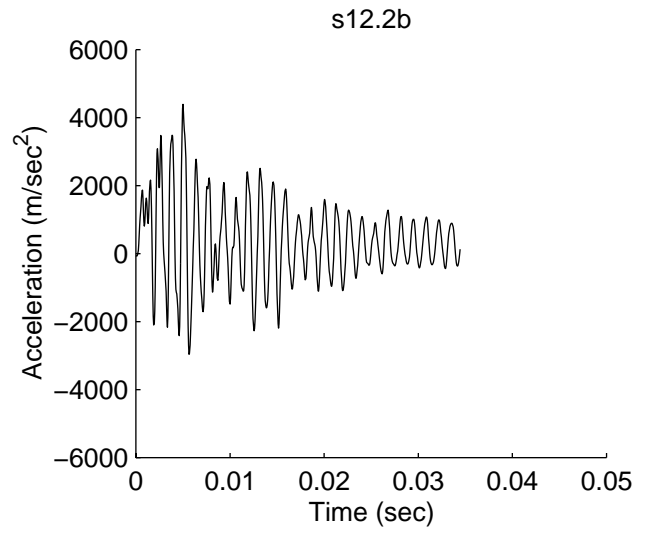
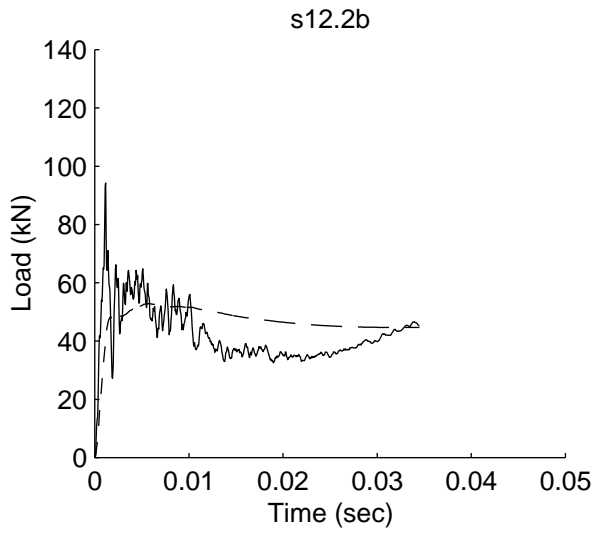


Figure A-9: Dynamic data traces for s12.2b

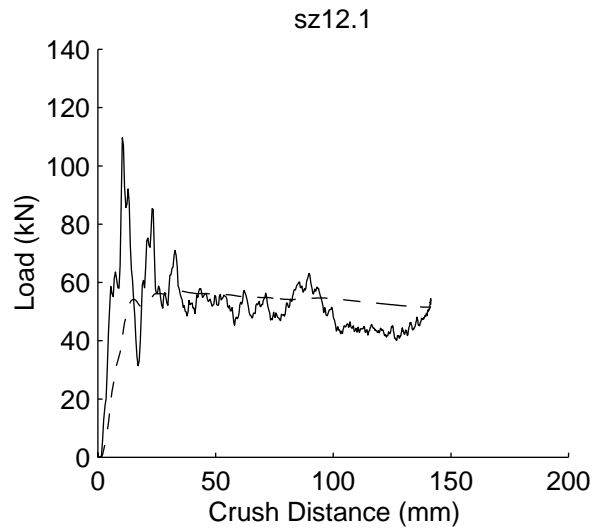
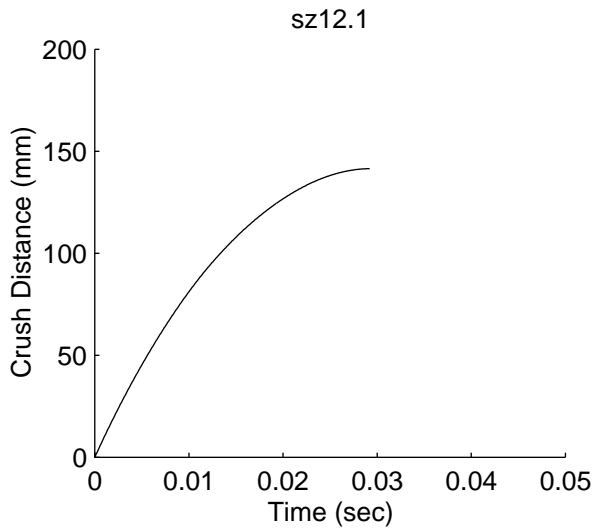
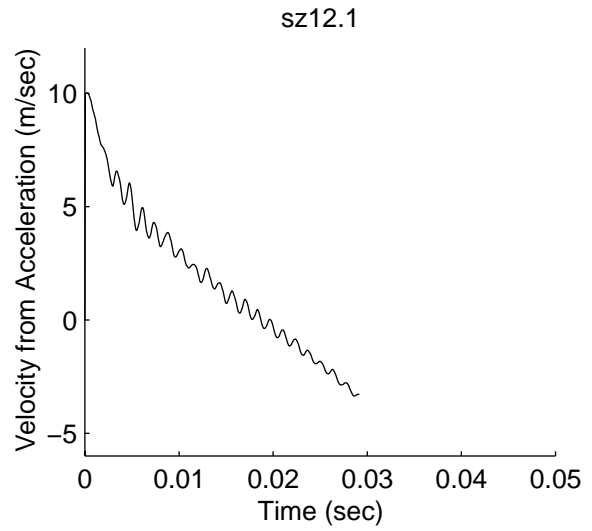
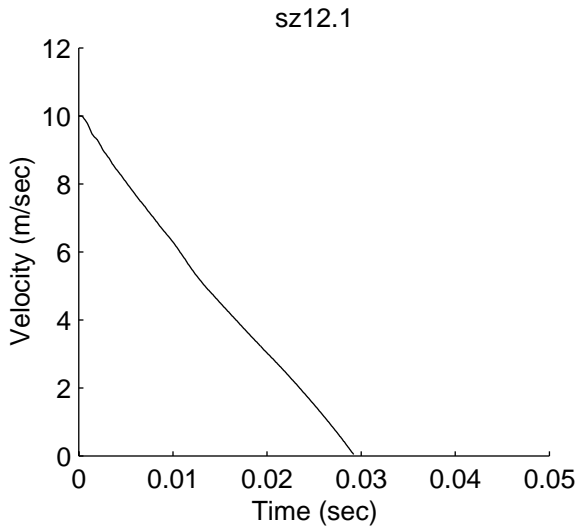
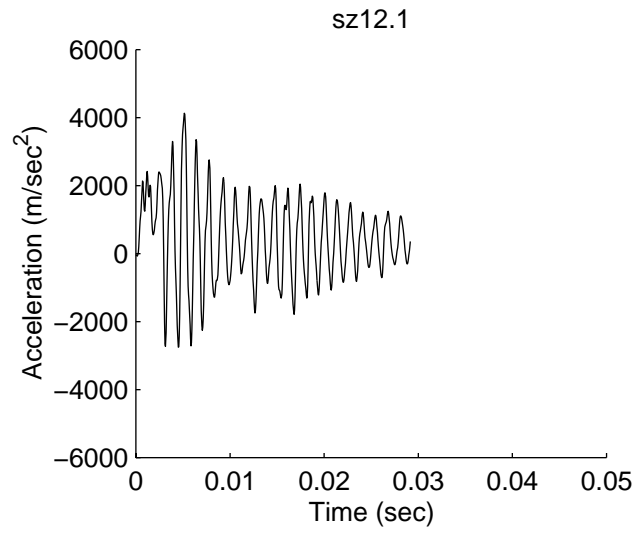
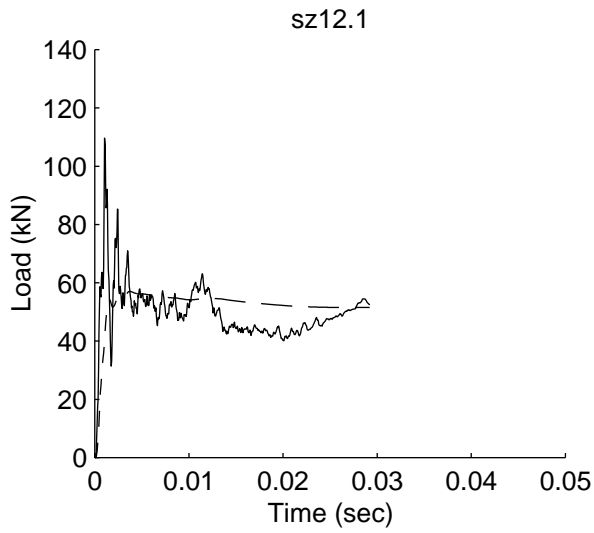


Figure A-10: Dynamic data traces for sz12.1

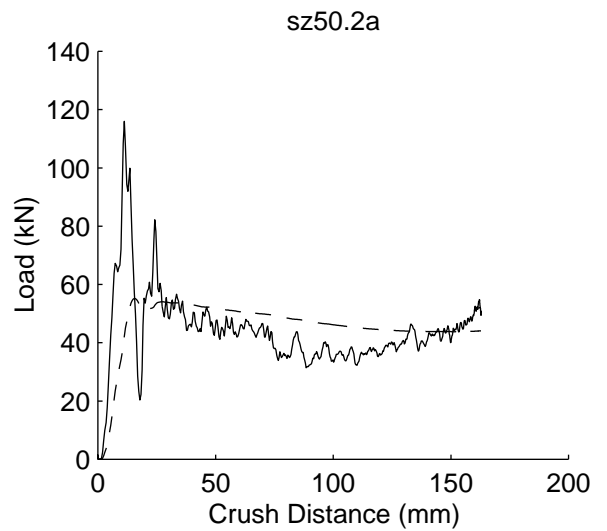
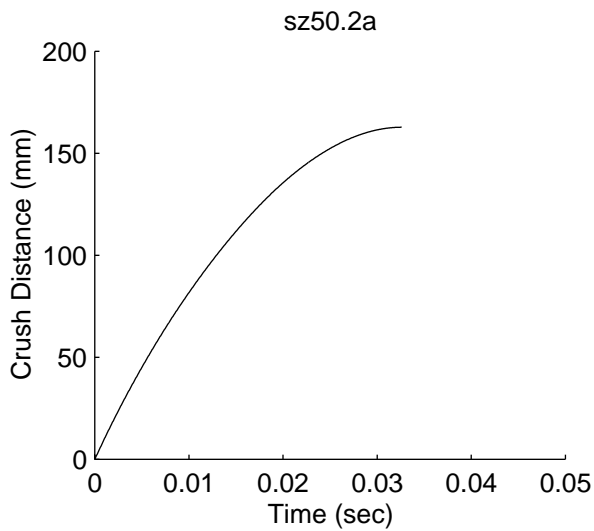
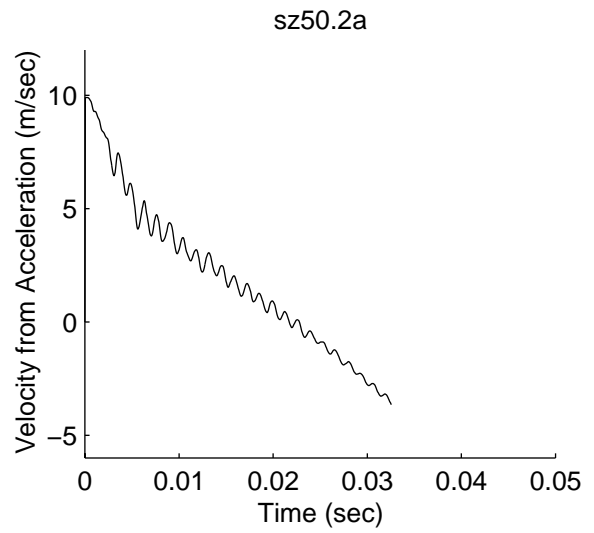
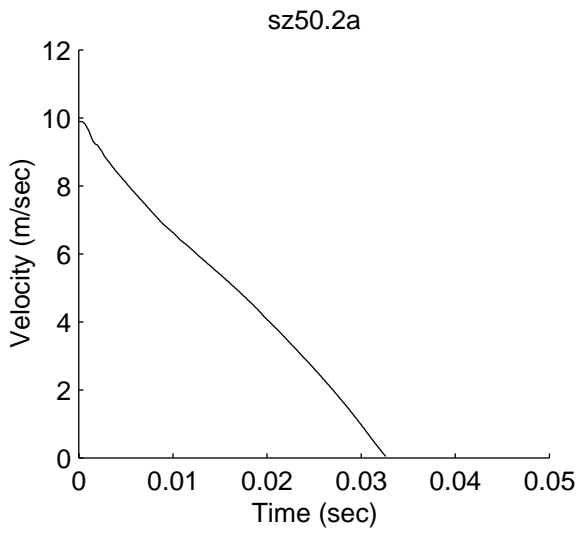
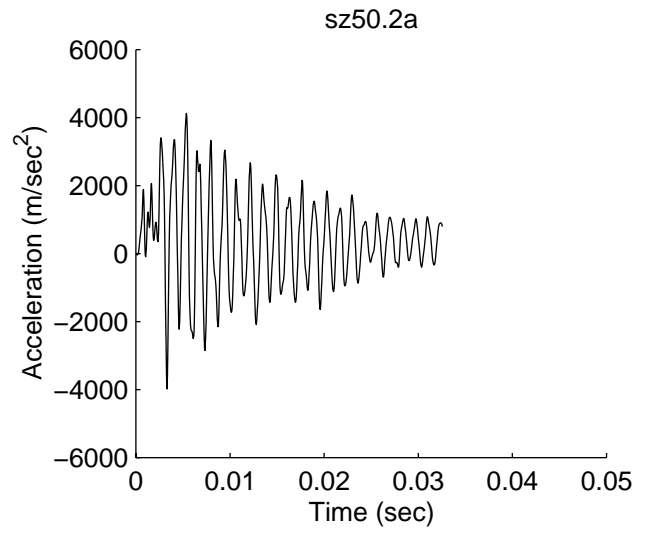
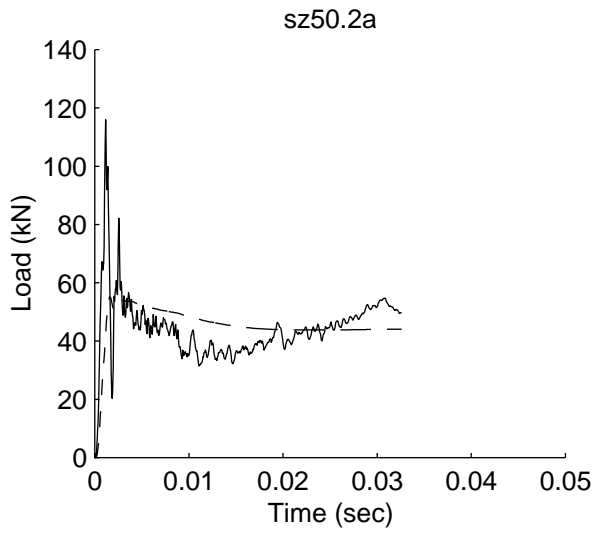


Figure A-11: Dynamic data traces for sz12.2a

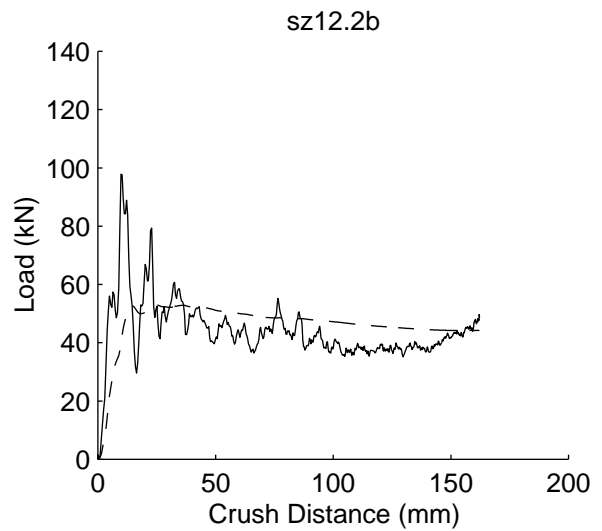
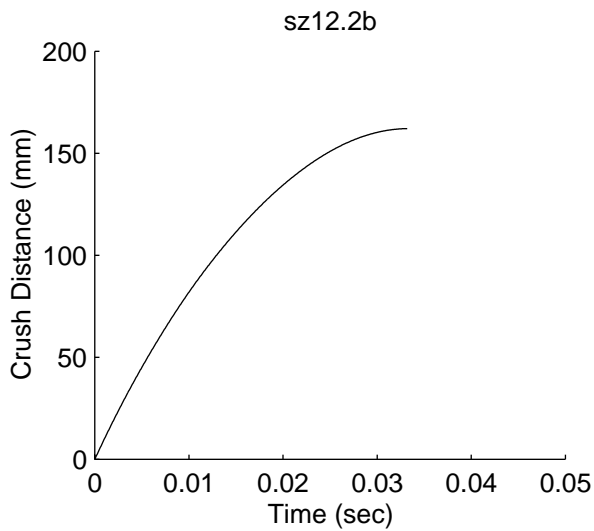
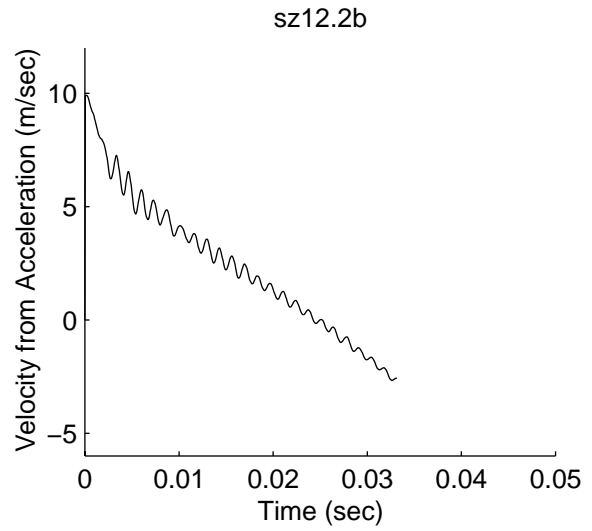
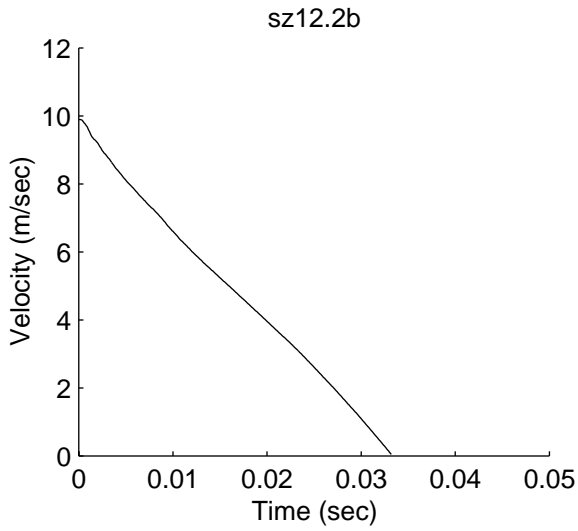
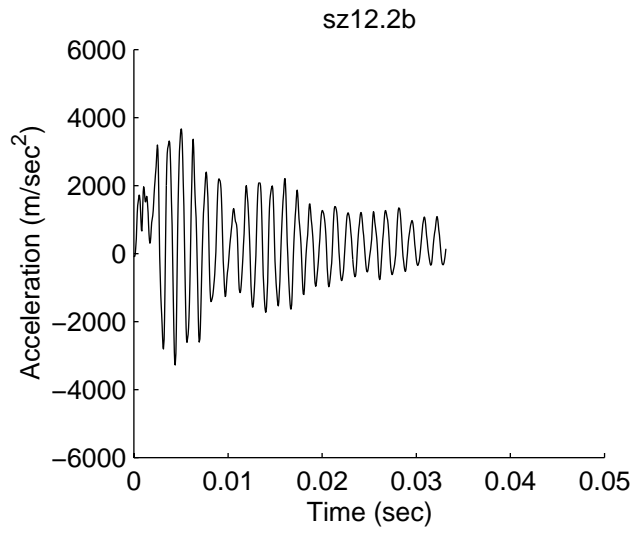
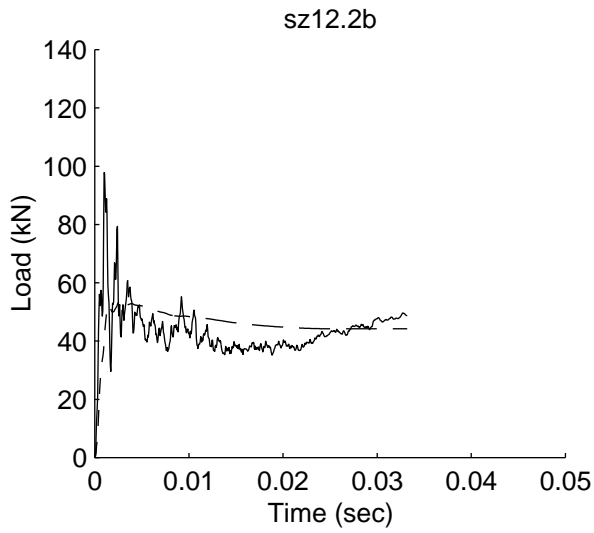


Figure A-12: Dynamic data traces for sz12.2b

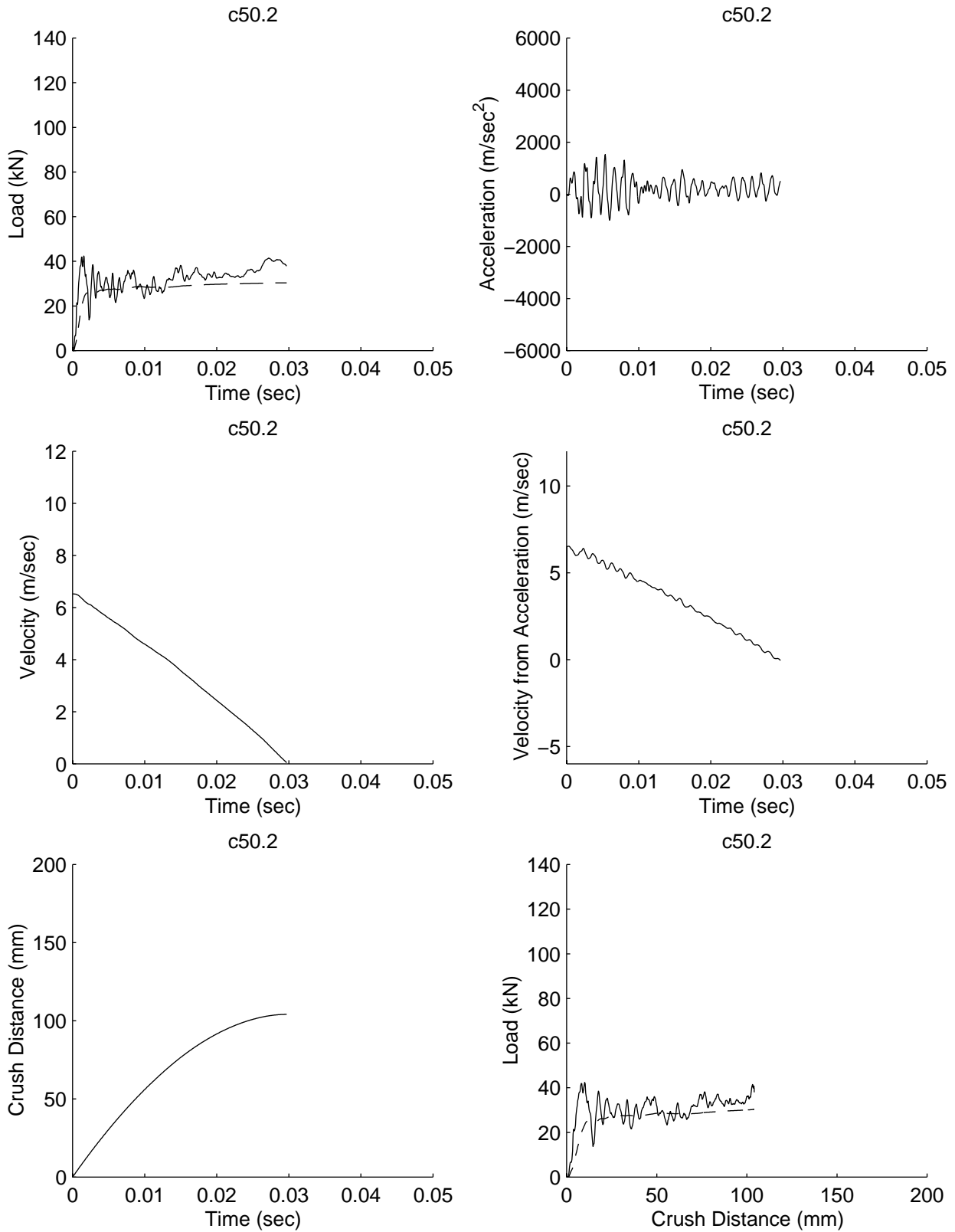


Figure A-13: Dynamic data traces for c50.2

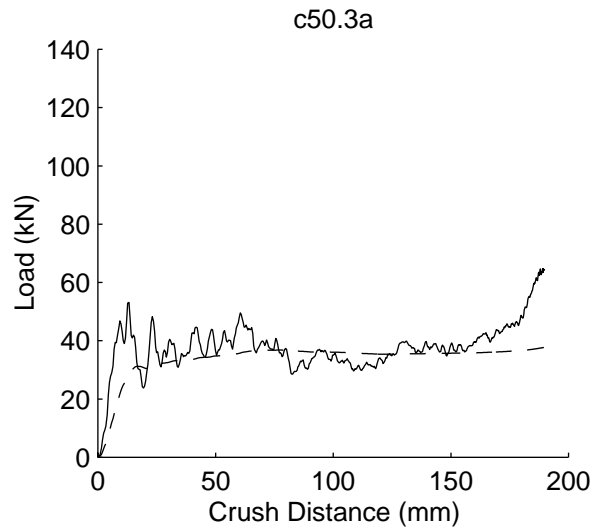
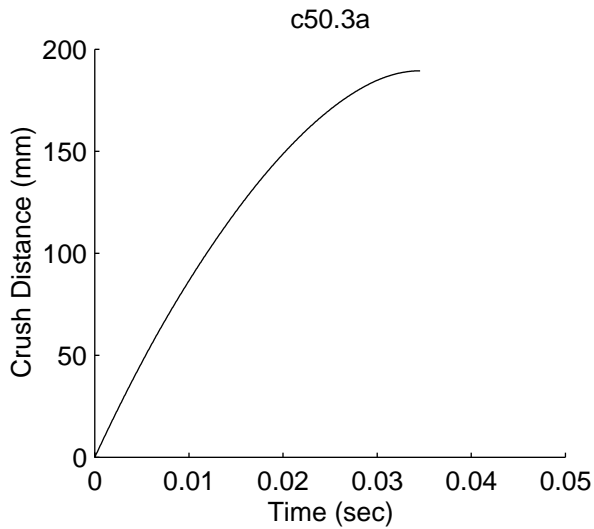
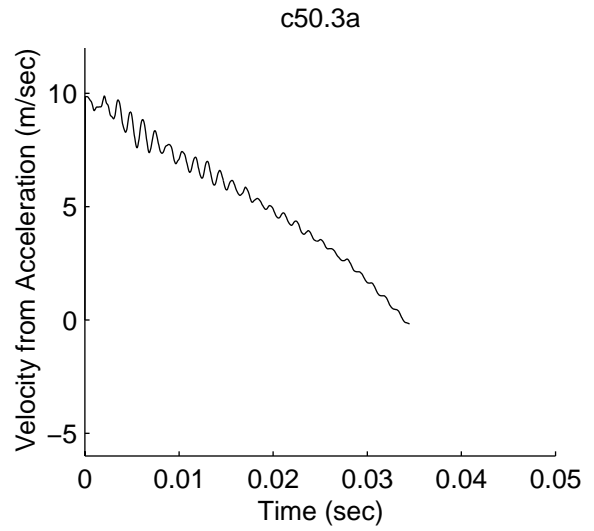
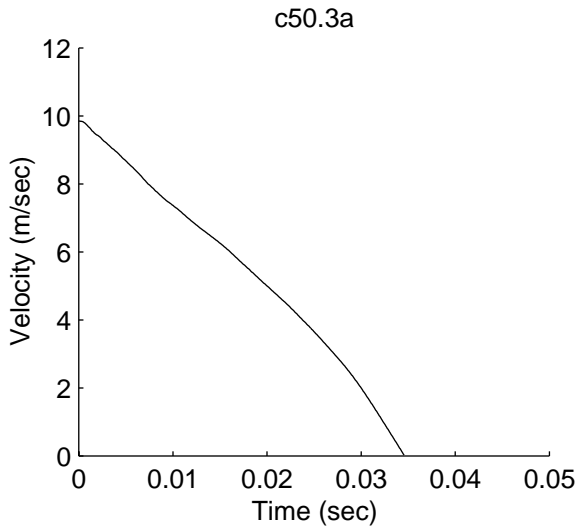
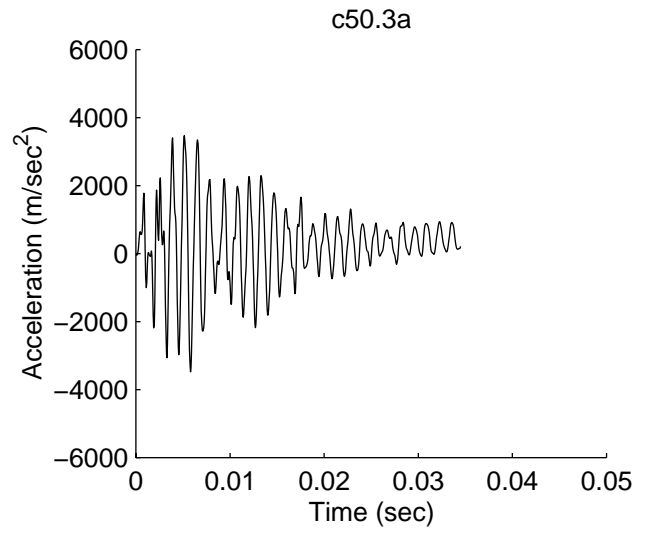
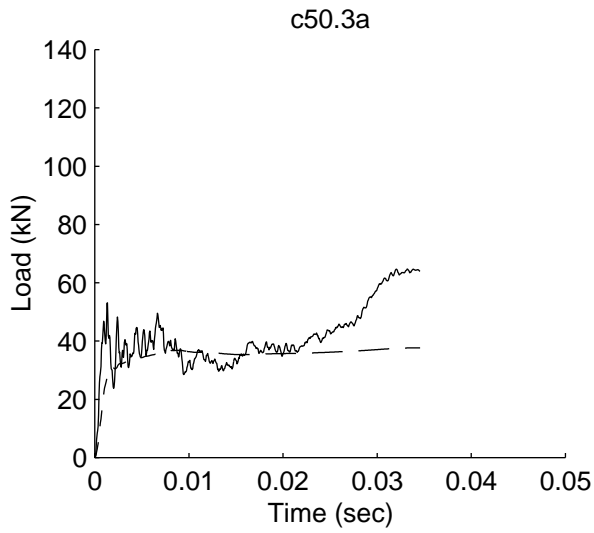


Figure A-14: Dynamic data traces for c50.3a

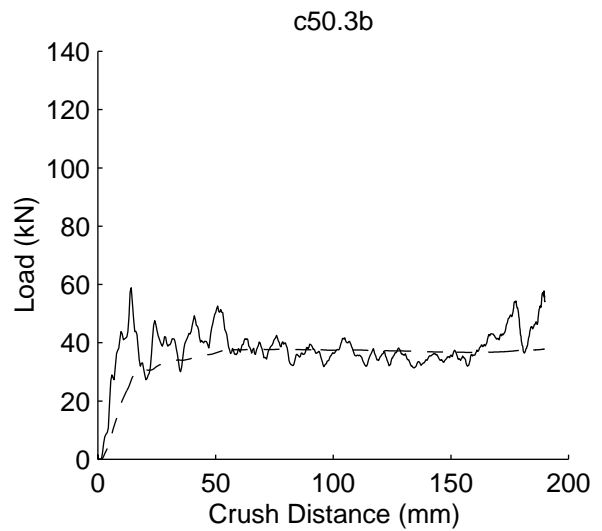
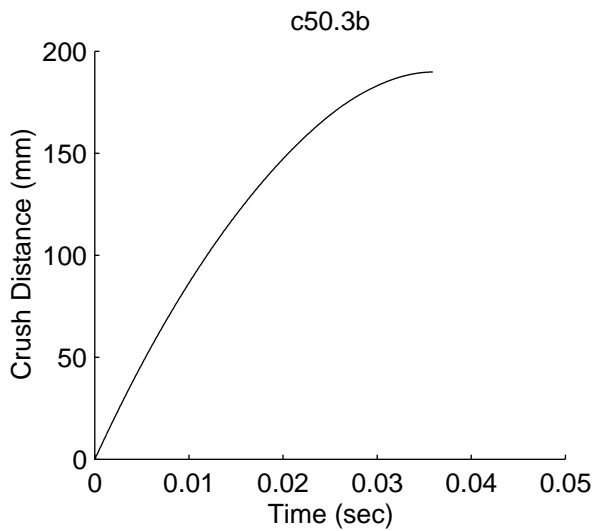
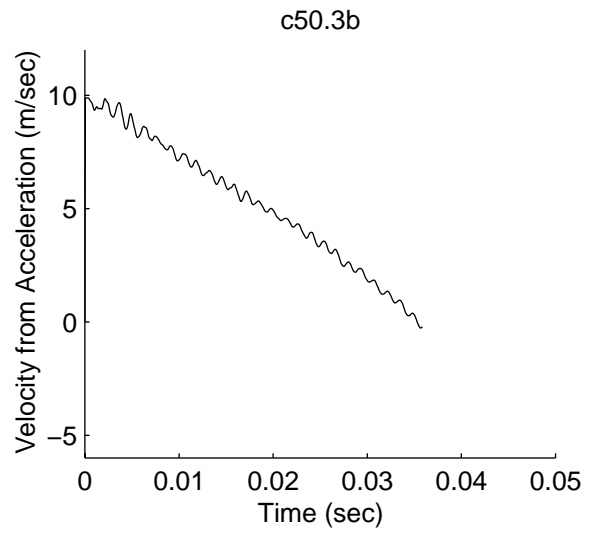
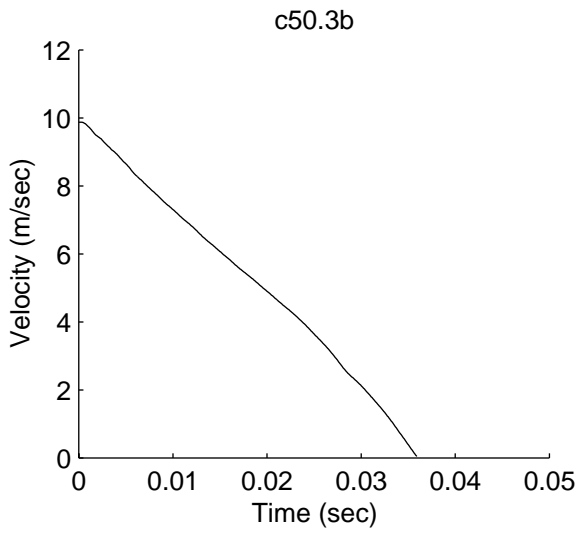
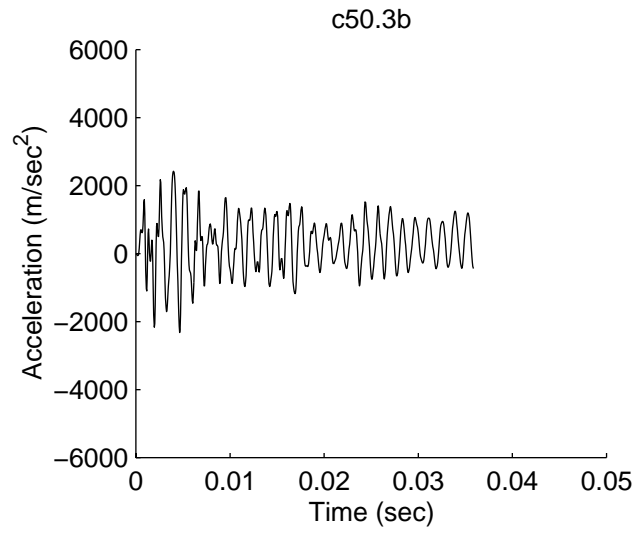
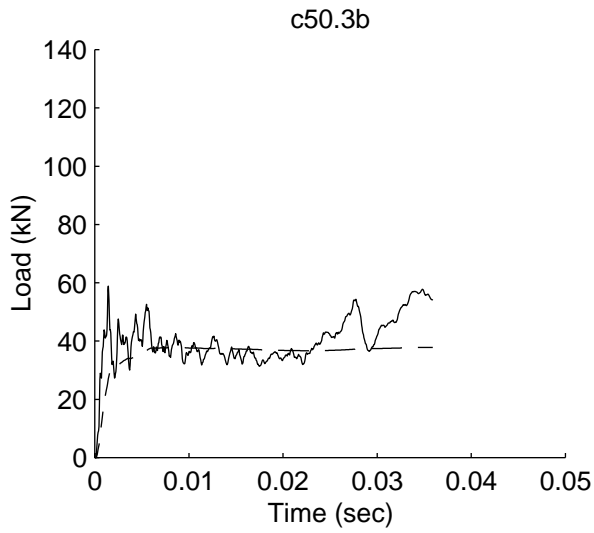


Figure A-15: Dynamic data traces for c50.3b

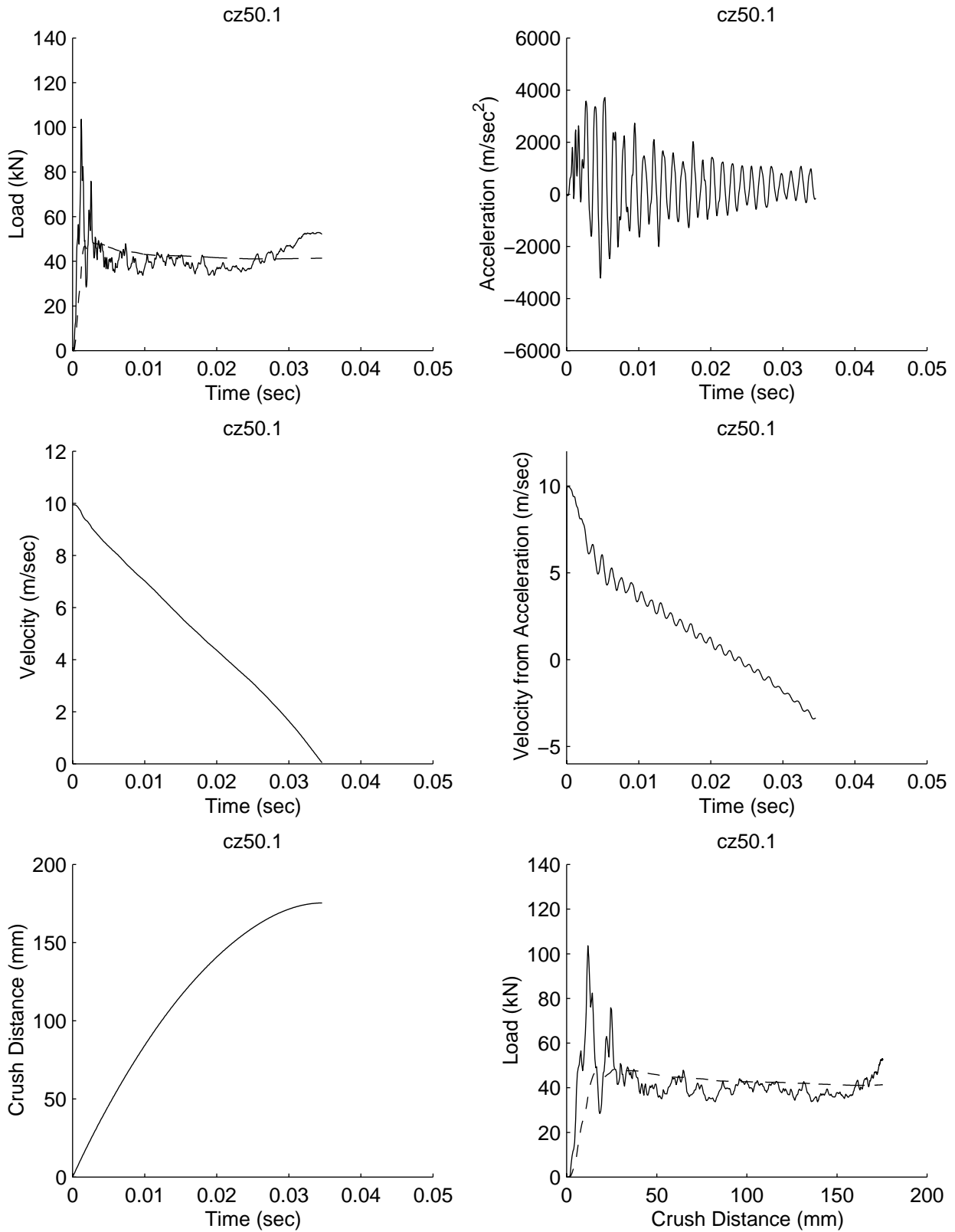


Figure A-16: Dynamic data traces for cz50.1

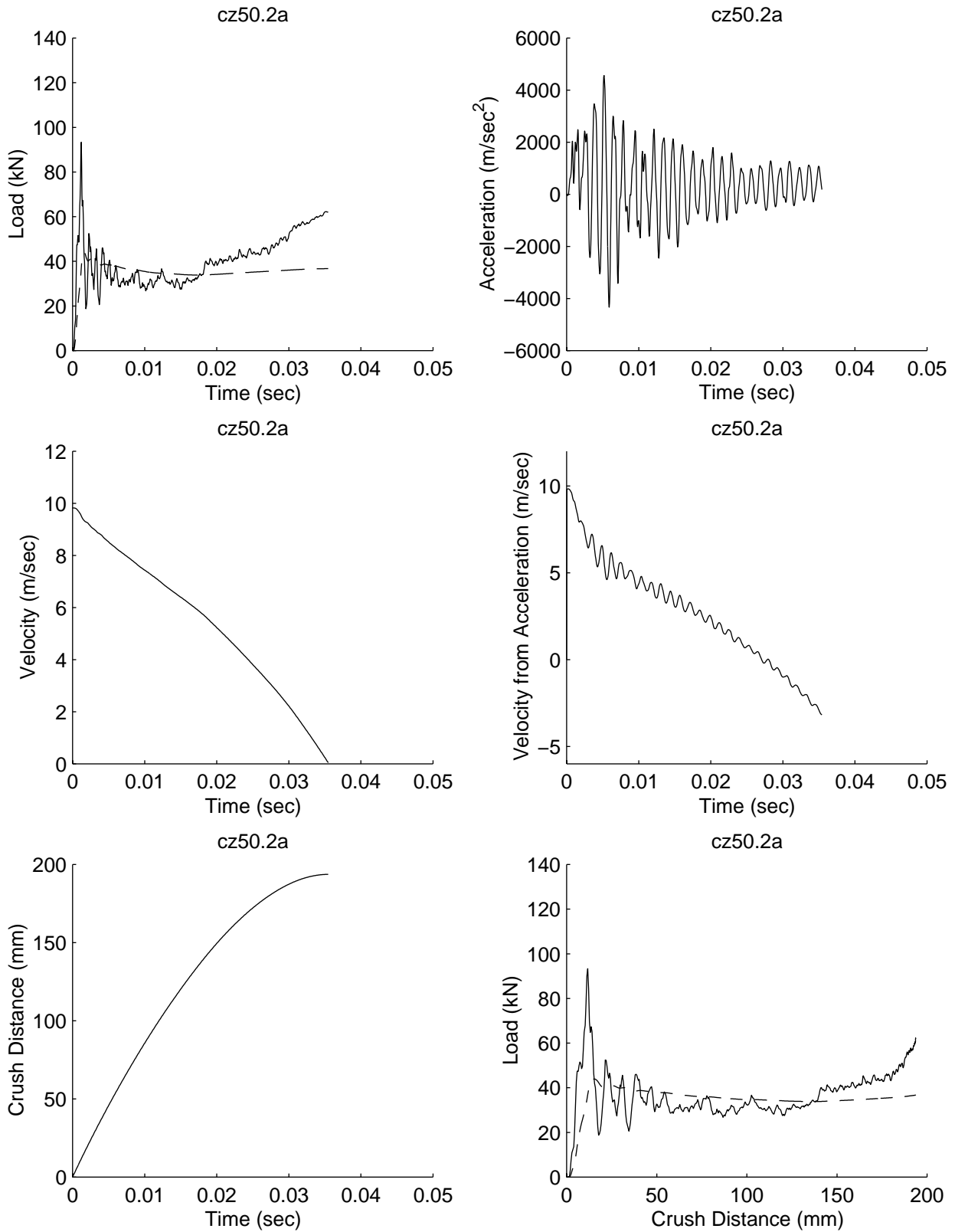


Figure A-17: Dynamic data traces for cz50.2a

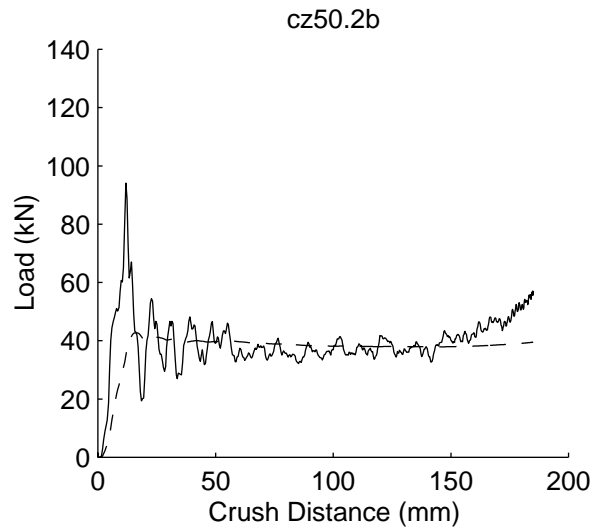
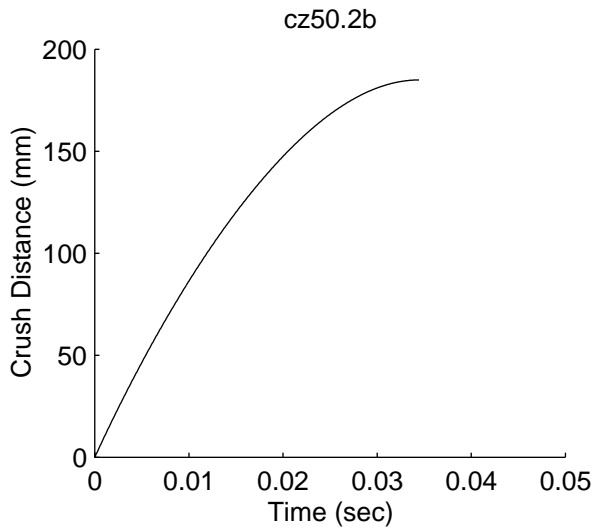
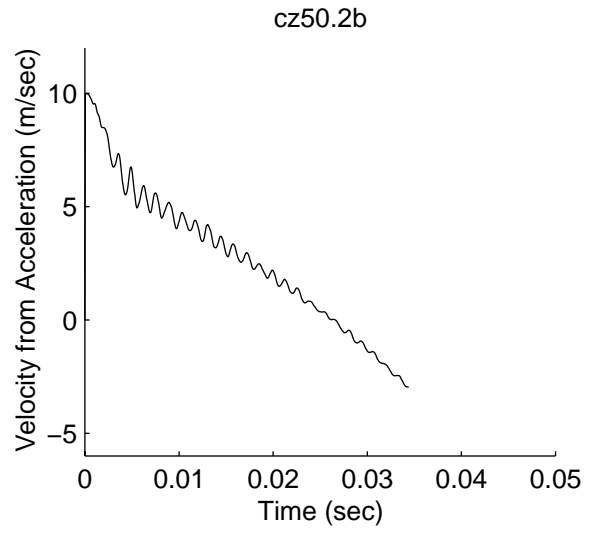
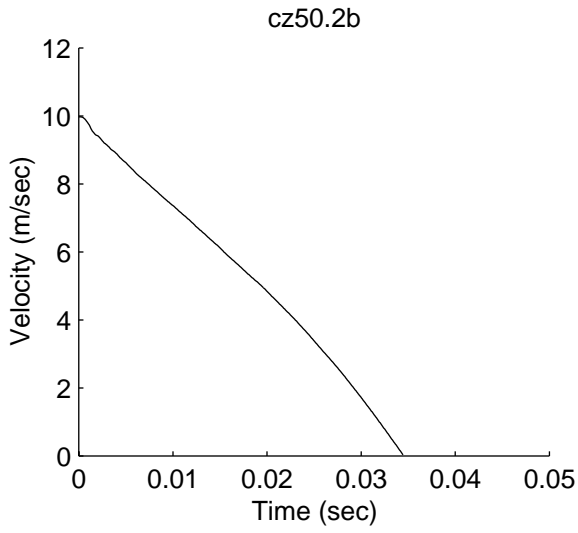
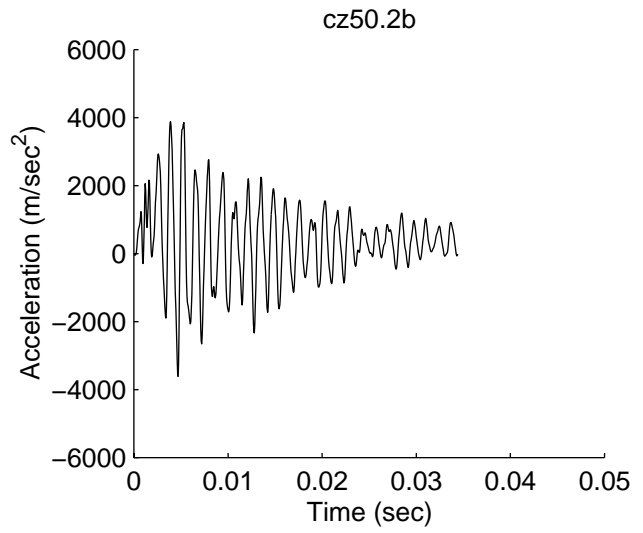
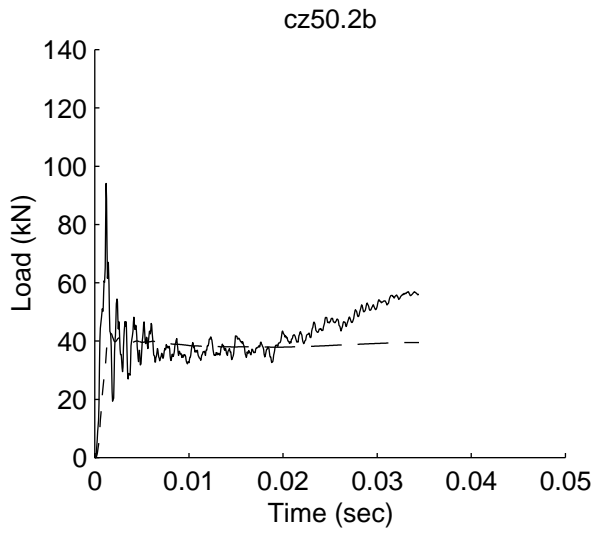


Figure A-18: Dynamic data traces for cz50.2b

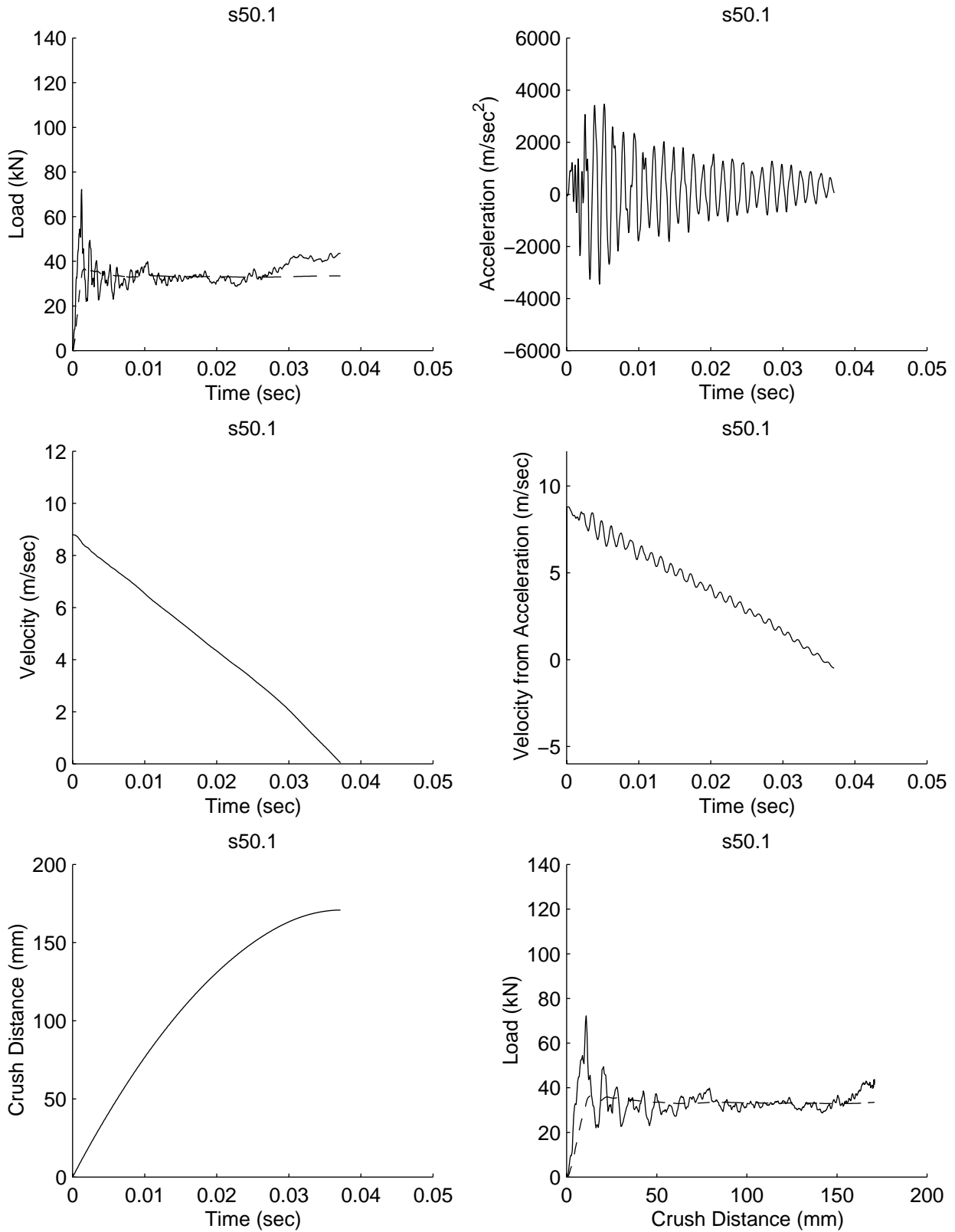


Figure A-19: Dynamic data traces for s50.1

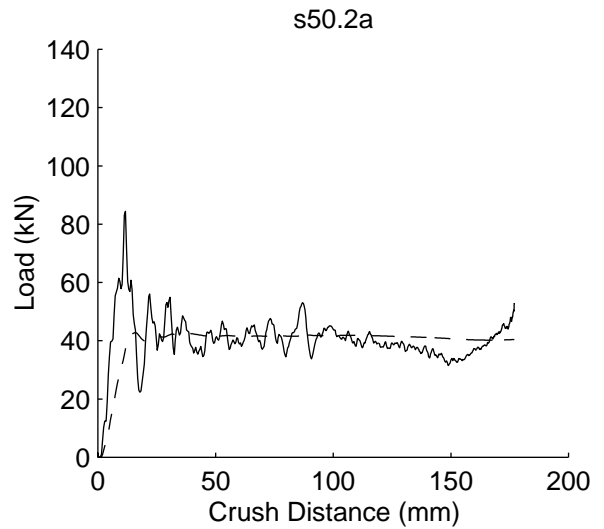
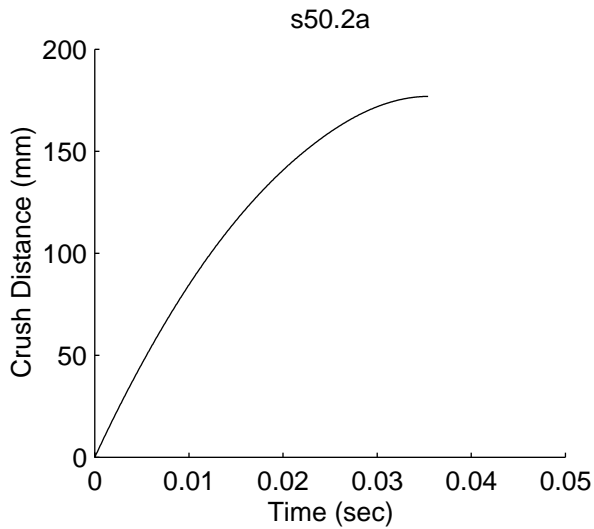
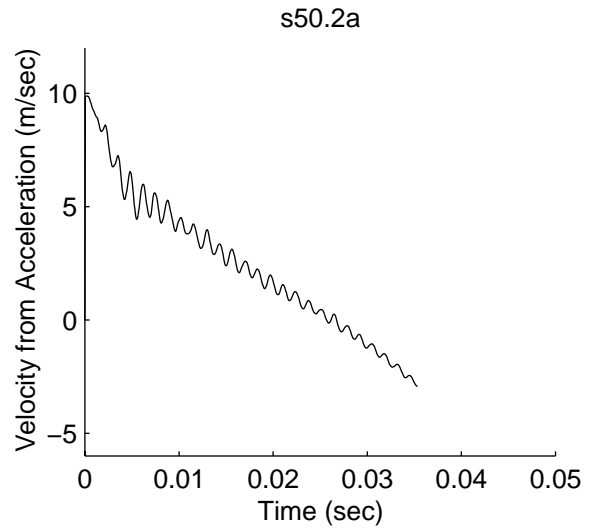
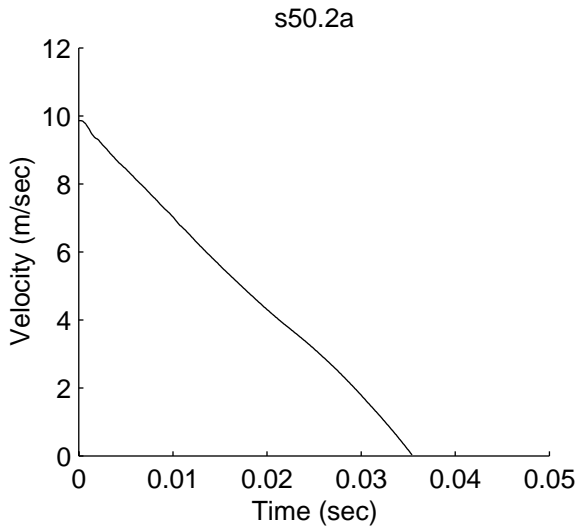
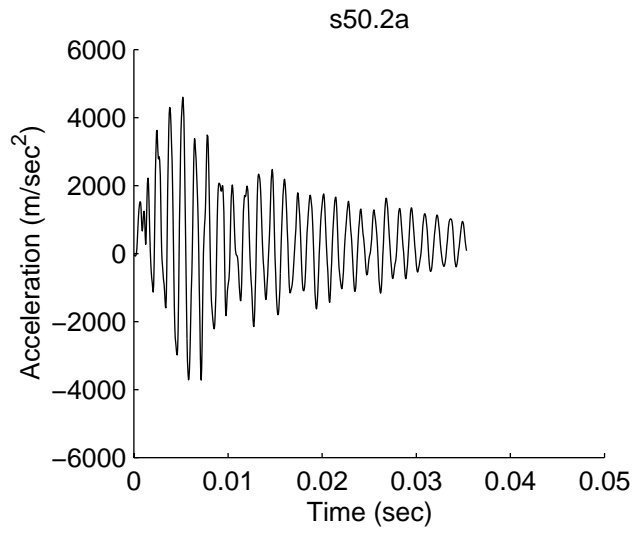
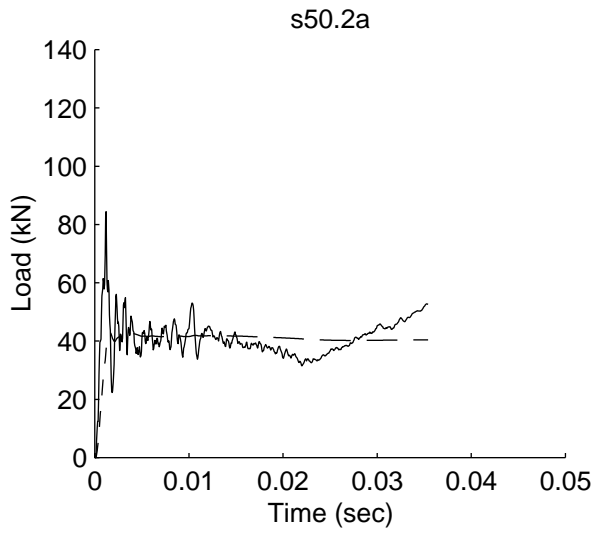


Figure A-20: Dynamic data traces for s50.2a

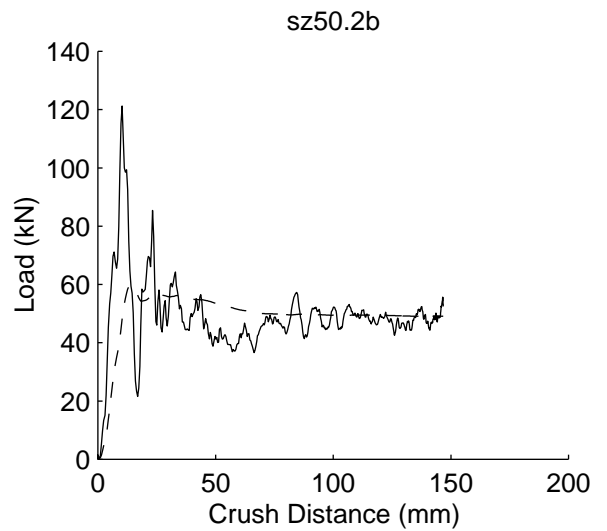
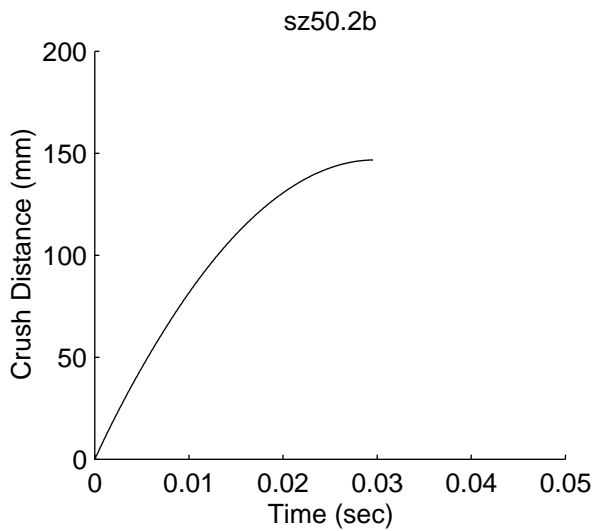
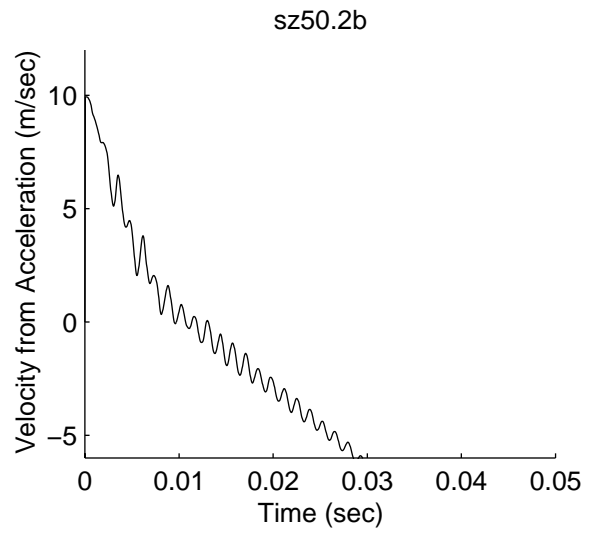
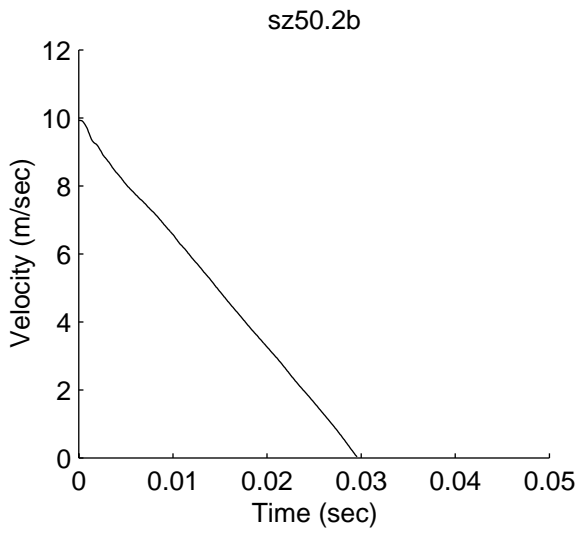
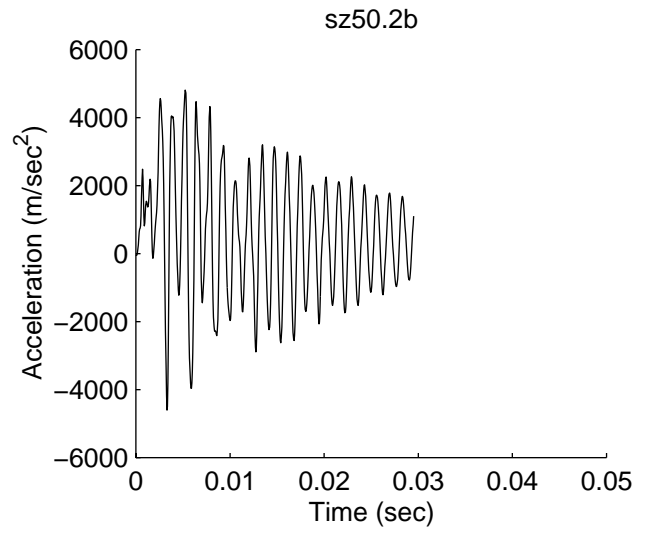
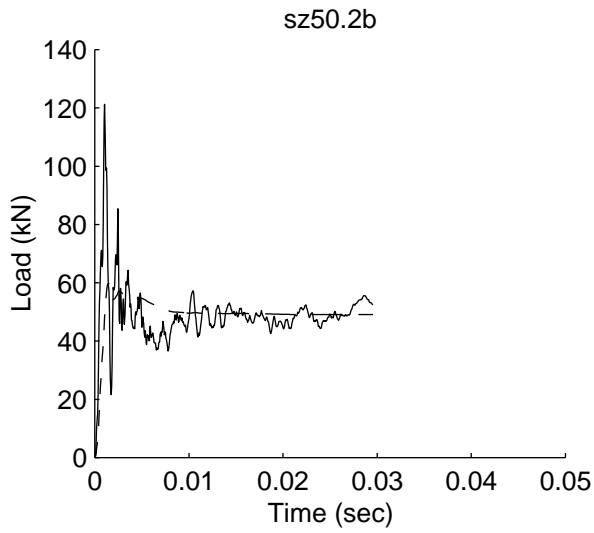


Figure A-21: Dynamic data traces for s50.2b

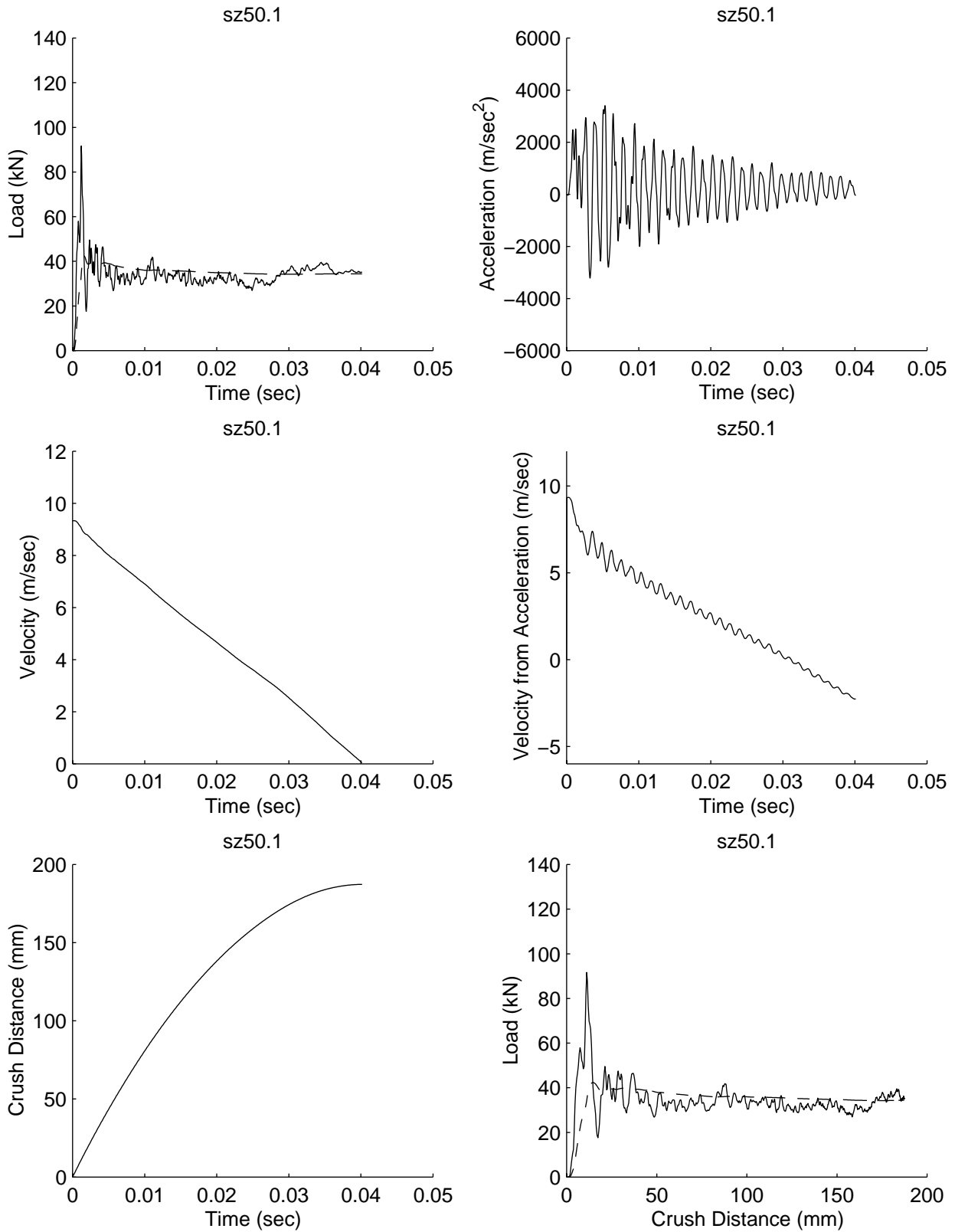


Figure A-22: Dynamic data traces for sz50.1

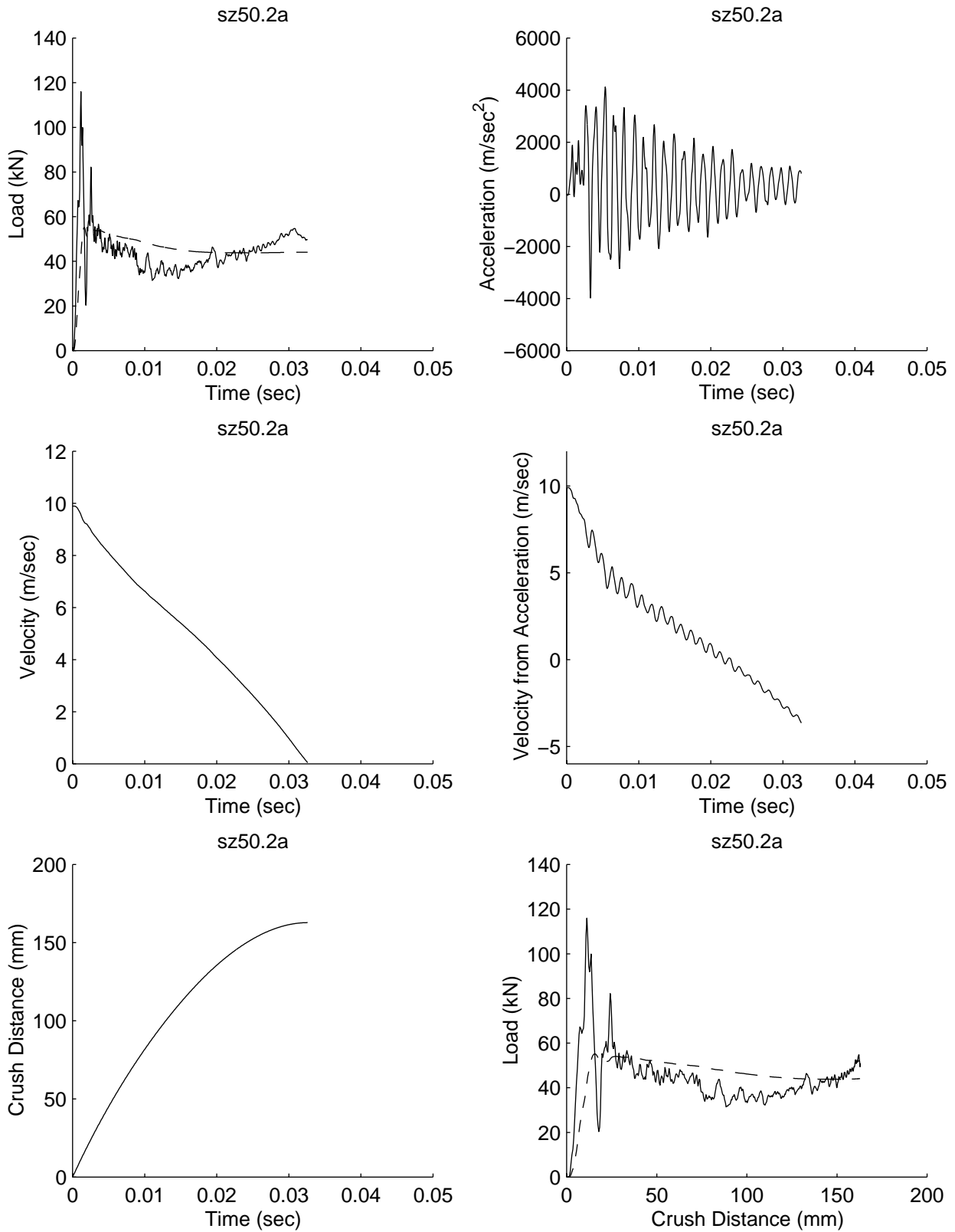


Figure A-23: Dynamic data traces for sz50.2a

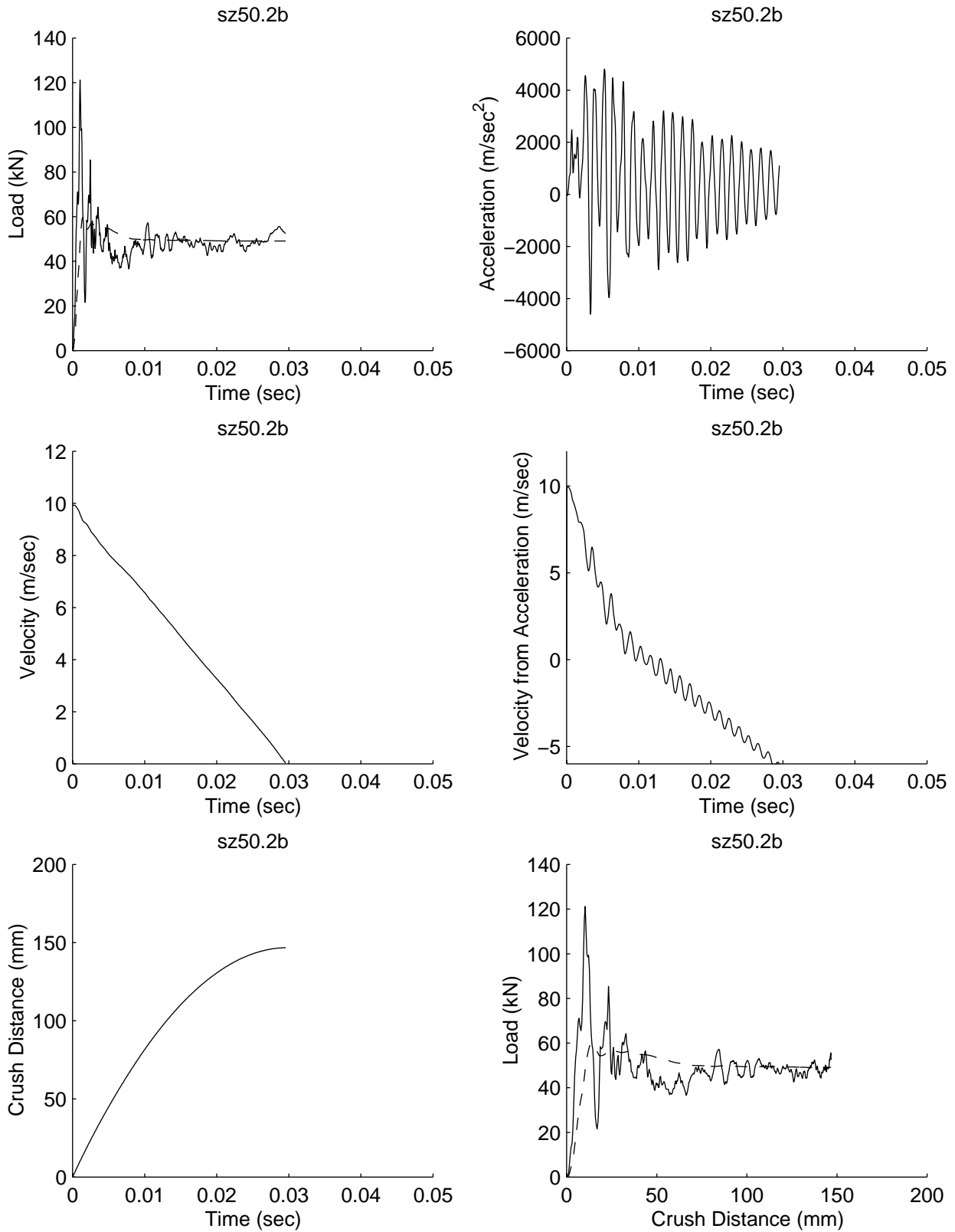


Figure A-24: Dynamic data traces for sz50.2b

Vita

Marc Robert Schultz

Marc Robert Schultz was born on December 17, 1972 and spent his early years in Rockland County, New York. After graduating from Clarkstown Senior High School South in 1991, he attended the State University of New York, University at Buffalo. While an undergraduate, he spent one summer participating in the Summer Undergraduate Research Program sponsored by the National Science Foundation (NSF) Science and Technology Center for High Performance Polymeric Adhesives and Composites at Virginia Polytechnic Institute and State University (Virginia Tech). In 1995, he graduated summa cum laude from the University at Buffalo with a Bachelor of Science degree in Mechanical Engineering. Upon graduation, he enrolled at Virginia Tech to pursue graduate studies in Engineering Mechanics. The research effort pursued as part of the Master of Science degree was sponsored by the NSF Science and Technology Center at Virginia Tech.